eXPRESS Polymer Letters Vol.9, No.7 (2015) 582
Available online at www.expresspolymlett.com
DOI: 10.3144/expresspolymlett.2015.54

Editorial corner – a personal view
Proper molecular level tool to explore the structure-property relationships in elastomer nanocomposites

L. Q. Zhang[1,2,3,4*], *J. Liu*[1,2,4]

[1]Key Laboratory of Beijing City on Preparation and Processing of Novel Polymer Materials, People's Republic of China
[2]Beijing Engineering Research Center of Advanced Elastomers, People's Republic of China
[3]Engineering Research Center of Elastomer Materials on Energy Conservation and Resources, Ministry of Education, PRC
[4]State Key Laboratory of Organic-Inorganic Composites, Beijing University of Chemical Technology, 100029 Beijing, People's Republic of China

Establishing a quantitative relation between the structure and properties of elastomer nanocomposites (ENCs) is still challenging and requires the multi-scale approach. To clearly and comprehensively characterize the multi-scale structure of ENCs, molecular dynamics simulation proved to be a powerful tool. We have studied the dispersion of nanoparticles (NPs) with different shapes in the elastomer matrix (DOI: 10.1021/la201073m, DOI: 10.1016/j.polymer.2014.01.042), and the interfacial chain mobility nearby the NPs (DOI: 10.1039/c0cp02952a). One important finding is that polymer depletion induces direct aggregation of NPs at low rubber-NPs interaction and at high interfacial interaction NPs are bridged via polymer chains, between which NPs exhibit a homogeneous dispersion by adsorbing a layer of polymer chains. This simulation result is consistent with the theoretical prediction (DOI: 10.1021/ma060577m).

Besides the molecular level characterization, the static and dynamic mechanical properties are also investigated. We have examined the reinforcement mechanism due to spherical and rod-like NPs (DOI: 10.1039/c4cp01555j, DOI: 10.1039/c0cp00297f). It was found the destruction of the network formed by aggregation between NPs directly or NPs via bridged polymer chains leads to the occurrence of the Payne effect under external tensile or shear loading (DOI: 10.1039/c4sm00233d). Since ENCs always exhibit strong viscous loss attributed to the large internal friction between various structural units, we design a compounding system by mixing elastomer with carbon nanosprings, which are a kind of helical carbon nanotubes and possess reversible mechanical deformation, and we find the hysteresis loss during the tension-recovery process can be dramatically reduced by enhancing the interfacial interaction between elastomer and carbon nanosprings and the spring constant of carbon nanosprings. This may open a new avenue for the fabrication of automobile tires made of ENCs with low fuel consumption (DOI: 10.1002/adfm.201201438).Based on these research works, it is believed that molecular dynamics simulation will play an important role in the study of ENCs. However, future progress should be focused on improving the simulated realness to come close to the experimental systems as much as possible, and increasing the calculation speed to cover multi-scale and length, which need and deserve more scientists to devote their efforts.

Prof. Dr. Li Qun Zhang
Member of International Advisory Board

*Corresponding author, e-mail: zhanglq@mail.buct.edu.cn

eXPRESS Polymer Letters Vol.9, No.7 (2015) 583–596
Available online at www.expresspolymlett.com
DOI: 10.3144/expresspolymlett.2015.55

Processing and characterization of plasticized PLA/PHB blends for biodegradable multiphase systems

I. Armentano[1], E. Fortunati[1], N. Burgos[2], F. Dominici[1], F. Luzi[1], S. Fiori[3], A. Jiménez[2], K. Yoon[4], J. Ahn[4], S. Kang[4], J. M. Kenny[1,5]*

[1]Materials Engineering Center, UdR INSTM, University of Perugia, Strada Pentima Bassa 4, 05100 Terni, Italy
[2]University of Alicante, Dpt. Analytical Chemistry, Nutrition & Food Sciences, 03690 San Vicente del Raspeig, Spain
[3]Condensia Química S.A. C/ Junqueras 16-11A, 08003 Barcelona, Spain
[4]Bio-materials R&D team, Samsung Fine Chemicals 130, Samsung-ro, Yeongtong-gu, Suwon-si, Gyeonggi-do 443-803, Korea
[5]Institute of Polymer Science and Technology, CSIC, Madrid, Spain

Received 29 October 2014; accepted in revised form 14 January 2015

Abstract. Blends of poly(lactic acid) (PLA) and poly(3-hydroxybutyrate) (PHB) plasticized with a lactic acid oligomer (OLA) added at three different concentrations (15, 20 and 30 wt% by weight), were prepared by an optimized extrusion process to improve the processability and mechanical properties of these biopolymers for flexible film manufacturing. Morphological, chemical, thermal, mechanical, barrier and migration properties were investigated and formulations with desired performance in eco-friendly films were selected. The efficiency of OLA as plasticizer for PLA_PHB blends was demonstrated by the significant decrease of their glass transition temperatures and a considerable improvement of their ductile properties. The measured improvements in the barrier properties are related to the higher crystallinity of the plasticized PLA_PHB blends, while the overall migration test underlined that all the proposed formulations maintained migration levels below admitted levels. The PLA_PHB blend with 30 wt% OLA was selected as the optimum formulation for food packaging, since it offered the best compromise between ductility and oxygen and water vapor barrier properties with practically no migration.

Keywords: *polymer blends and alloys, poly(lactic acid), poly(hydroxybutyrate), biodegradable, lactic acid oligomers*

1. Introduction

Reduction of packaging wastes has been a strong motivation for replacing the most common plastics by bio-based and/or biodegradable materials. Simultaneously, the food packaging industry requires the development of simple formulations produced by easy, readily available and cost effective processing technologies such as melt blending approaches [1]. At the same time, consumers demand high quality food with long shelf-life and also they desire see through the packaging to perceive the foodstuff aspect. Thus, food packagings are required to contain food products and protect them from the surroundings avoiding contamination, humidity and oxidations process as well as being transparent enough to allow seeing the food through the packaging. In this context, the efficiency in the use of polymer films in food packaging has however been limited by their poor mechanical properties and by their moisture sensitivity. Improving their processability and tensile properties is an important challenge to be afforded before sending these formulations to the market. Consequently, the modification of these materials is in the focus of scientific research.

*Corresponding author, e-mail: ilaria.armentano@unipg.it

In contrast to the development of novel polymeric materials and new polymerization routes, blending is a relatively cheap and fast method to tailor the plastics properties. As a result, this approach may play a crucial role in increasing the competitiveness of biopolymers [2–5]. Poly(lactic acid) (PLA) thereby represents the most investigated aliphatic polyester for a wide range of applications, due to its biodegradability, renewability and excellent mechanical properties, good processability and low cost [6, 7]. It is now produced on a large scale and used for various applications in different domains: packaging, medicine, agriculture and textiles. However, high brittleness, slow crystallization rate and low barrier properties of PLA compared to those of synthetic polymers strongly limit its applications in, for instance, food packaging [6]. Several strategies have been attempted for PLA to enhance its crystallization rate as well as to improve its barrier properties. Blending of PLA with other biopolymers or conventional synthetic polymers is one of the most effective methods to obtain new properties required for specific end-use applications [8, 9]. For example, blending PLA with poly(hydroxybutyrate) (PHB), a highly crystalline biopolymer with high melting point and among the most studied polyhydroxyalkanoates (PHAs), leads to materials with interesting physical, thermal, and mechanical properties compared to neat PLA [10–12].

PLA and PHB are biodegradable polyesters and they are used in consumer products by several industrial sectors due to their biocompatibility, biodegradability and sustainability [6, 12, 13]. They have comparable thermal and mechanical properties to those of some conventional/non-degradable polymers and this has generated much interest in exploring their physical and processing properties for sustainable packaging applications.

Zhang *et al.* [11] and Zhang and Thomas [12] reported that PLA melt blended with 25 wt% of PHB showed optimal miscibility between both polymers and improvement in tensile properties compared to pure PLA, due to the reinforcement effect of the small, finely dispersed and highly crystalline PHB particles with the result of enhancing the PLA crystallinity by the nucleating agent of PHB in PLA matrices. Other authors also found that the addition of PHB significantly improved the crystallinity and crystallization rate of PLA [14]. Furthermore PLA_PHB (75:25) blends showed improved oxygen barrier and surface wettability properties, whereas their disintegrability under composting conditions suggested a valuable end-life option for PLA_PHB packaging materials [1].

Similarly, Noda *et al*. [10] found an improvement in toughness of PLA_PHAs blends, as long as the content of PHAs is not high (below 20 wt%). This singular behavior was explained by the unusually slow crystallization kinetics of PHAs, when PHA particles are dispersed in small domains (around 1 μm), leading to rubbery amorphous PHA particles dispersed in the hard and brittle PLA matrix.

On the other hand, with regard to the field of application, plasticizers are frequently incorporated into PLA-based materials, to improve their processability and/or other properties required by a specific application [14]. The addition of plasticizers to PLA allows the production of flexible films by improving its inherent brittle nature. Plasticizers exchange the intermolecular bonds among polymer chains to bonds between the macromolecules and the small molecular weight compound, thus promoting conformational changes resulting in increased deformability. Both, the glass transition and the processing temperatures of the material decrease, thus enabling the melt processing of heat-sensitive polymers at lower temperatures [4, 5, 11, 12, 15, 16]. Concerning food contact materials, plasticizers should meet several requirements, in particular being non-toxic, showing good compatibility with the polymer and providing suitable thermal, mechanical and barrier properties. Besides transparency, their low volatility and low migration to foodstuff are also relevant parameters to ensure the permanence of the plasticizer in the polymer matrix, and consequently the stability of films during their shelf life. Several compounds have been studied as potential PLA plasticizers, such as triacetine, citrate esters [17], glycerol [18], malonate oligomers, adipates and polyadipates, poly(ethylene glycol) (PEG) [19], poly(propylene glycol) (PPG) or their copolymers. However, their incorporation into PLA without showing phase separation over time was restricted to concentrations lower than 20 wt% in all cases [20]. In general, it has been accepted that amounts from 10 to 20 wt% of plasticizers are required to provide a substantial reduction in the PLA glass transition temperature (T_g) as well as to obtain adequate mechanical properties for films manufacturing. The ideal approach to increase miscibility between PLA and potential

plasticizers would be to add a compound with similar chemical structure and a relatively high molar mass to reduce migration rate and detrimental changes in the material properties over time [21]. Martin and Averous reported the addition of glycerol and oligomeric lactic acid (OLA) to PLA and compared both with other plasticizers, such as citrate ester and polyethylene glycol (PEG) with different average molecular weight. Conclusions were drawn that glycerol was the least efficient plasticizer, and OLA and the lower molecular weight PEG gave the best performance to increase ductile properties in PLA [19, 22].

The aim of this paper is to study the effects of OLA on PLA_PHB blends to improve the polymer and blend processability for films manufacturing with selection of adequate OLA contents to get the desired performance and to create a new type of eco-friendly blends suitable for single-use applications, such as fast-food packaging.

2. Experimental part

2.1. Materials

Commercial poly(lactic acid) PLA 3051D, was purchased from NatureWorks® Co. LLC, USA. This PLA grade shows specific gravity 1.25 g·cm^{-3}, molecular weight (M_n) 1.42·10^4 g·mol^{-1}, and a melt flow index (MFI) of 7.75 g/10 min tested at 210°C and 2.16 kg loading.

Poly(3-hydroxybutyrate) (PHB), was supplied by NaturePlast (France). This PHB grade has a density of 1.25 g·cm^{-3}, MFI 15–30 g/10 min tested at 190°C and 2.16 kg loading.

The plasticizer selected for this study is based on oligomeric lactic acid (OLA), developed and provided by Condensia Quimica S.A (Barcelona, Spain) [23]. OLA was synthesized as described elsewhere [21] and it was produced as a slightly colored liquid with molar mass (M_n) of 957 g·mol^{-1} (determined by size exclusion chromatography) and glass transition temperature around –37°C (determined by differential scanning calorimetry, DSC).

2.2. Processing of binary and ternary blends

PLA and PHB were pre-dried to get rid of any moisture trace in the polymer structure and to avoid any undesirable hydrolysis reaction during processing. PLA was put into an oven at 98°C for 3 h, while PHB was dried at 70°C for 4 h. PLA and PLA/PHB based formulations were processed and mixed by using a twin-screw microextruder (Dsm Explore 5&15 CC Micro Compounder). Processing parameters (screw speed, mixing time and temperature profile) were modulated to optimize the extrusion procedure. The selected ratio content of PHB was 15 wt% in the PLA/PHB blends.

OLA was pre-heated at 100°C for 5 min, to ensure the liquid condition during the extrusion process.

Three different OLA concentrations were selected based on the results obtained in a previous report [20]: 15, 20 and 30 wt%, as shown in Table 1.

PLA and PLA_PHB blend films with thicknesses between 20 and 60 μm were obtained by extrusion with the adequate filmature tip. Screw speed at 100 rpm was used to optimize the material final properties, while the temperature profile was set up at 180–190–200°C in the three different extrusion areas. The total processing time was established at 6 minutes. PLA alone was mixed for 6 min; in the case of PLA_15PHB blend, i.e. PLA was processed for the first 3 min and PLA_PHB for the remaining 3 min, while in the PLA_PHB_OLA systems, PLA_PHB was previously mixed for 3 min and OLA was added to the polymeric blend for the last 3 min (Table 1).

2.3. Characterization techniques

2.3.1. Morphology

The transparency of the films was evaluated by visual observation, while the morphology and micro-

Table 1. Material formulations and process parameters

Formulations	Component contents			Mixing parameters		
	PLA [wt%]	PHB [wt%]	OLA [wt%]	Speed [rpm]	Mixing time [min]	Temperature profile [°C]
PLA	100	0	0	100	6	180–190–200
PLA_15PHB	85	15	0	100	3+3*	180–190–200
PLA_15PHB_15OLA	70	15	15	100	3+3**	180–190–200
PLA_15PHB_20OLA	65	15	20	100	3+3**	180–190–200
PLA_15PHB_30OLA	55	15	30	100	3+3**	180–190–200

*3 min mixing PLA and 3 min mixing PLA_PHB

** 3 min mixing PLA_PHB and 3 min mixing PLA_PHB_OLA

structure of the fracture surfaces of PLA, PLA_PHB and PLA_PHB_OLA films were investigated by field emission scanning electron microscope (FESEM Supra 25, Zeiss, Germany). Films were previously freeze-cut in liquid nitrogen, gold coated with an Agar automatic sputter coated and then analysed.

2.3.2. X-ray diffraction (XRD)

Crystalline/amorphous character of all blends was evaluated by Wide angle X-ray scattering (WAXS) by using a Bruker D8-Advance (Madison, WI, USA) diffractometer, equipped with a Cu Kα radiation source (λ = 1.546 Å), operating at 40 kV and 40 mA as the applied voltage and current, respectively. The incidence angle (2θ) was varied between 2 and 90° at a scanning rate of 2°·min^{-1}.

2.3.3. Thermal analysis

Differential scanning calorimetry (DSC) tests were carried out with a TA Instruments Mod. Q200 calorimeter to determine the effect of the OLA content on the glass transition temperature (T_g) of PLA and PLA_PHB blends. Tests were performed in three cycles (two heating and one cooling scans) from –25 to 200°C, at 10°C·min^{-1}. Glass transition, crystallization and melting phenomena in PLA, PLA_PHB and PLA_PHB_OLA blends were determined.

Degree of crystallinity X_c was calculated by using Equation (1):

$$X_c = \frac{\Delta H_m - \Delta H_{cc}}{w \cdot \Delta H_m^0} \quad (1)$$

where ΔH_m and ΔH_{cc} are the enthalpy of melting and cold crystallization peaks, respectively; w is the weight fraction of PLA polymer in the sample and ΔH_m^0 is the heat of melting of purely crystalline PLA, considering these values as 93 J·g^{-1} [4, 5].

Thermal degradation behavior of PLA-based formulations was evaluated by thermogravimetric analysis (TGA, Seiko Exstar 6300, Tokyo, Japan); 5 mg samples were used and dynamic tests were performed in nitrogen atmosphere (250 mL·min^{-1}) from 30 to 600°C at 10°C·min^{-1}. Thermal degradation temperatures (T_{max}) for each tested material were evaluated.

2.3.4. Infrared spectroscopy (FT-IR)

FT-IR spectra were obtained at room temperature in reflection mode by attenuated total reflectance (ATR) with a FT-IR spectrometer (Jasco FT-IR 615, Japan). The scanned wave number range was 4000–600 cm^{-1}, at 4 cm^{-1} of spectral resolution.

2.3.5. Tensile tests

The tensile properties of neat PLA, PLA_PHB, and PLA_PHB_OLA blends were evaluated. Tests were performed on 50×10 mm^2 rectangular probes as indicated in the UNI EN ISO 527-5 standard, with a crosshead speed 1 mm·min^{-1} and a load cell 50 N. These tests were carried out in a digital Lloyd testing machine (Lloyd Instrument LR 30K Segensworth West, Foreham, UK) and the initial grip separation was 25 mm. Tensile strength (σ_b), failure strain (ε_b), yield strength (σ_y), yield strain (ε_y) and elastic modulus (E) were calculated from the resulting stress-strain curves. These measurements were performed at room temperature and at least six samples were tested for each specimen.

2.3.6. Barrier properties

Films of PLA and PLA_PHB blends for barrier properties testing were obtained by compression moulding. Blends were melted at 170°C in a Carver Inc. Hot Press (Wabash, Indiana, USA) by keeping them between the press plates for 4 minutes at atmospheric pressure. Then, pressure was gradually increased during 2 minutes up to 5 MPa and maintained for 5 minutes. Circular films with homogeneous thickness (235±15) μm and 14 cm diameter were obtained. The Oxygen Transmission Rate (OTR) tests were conducted with an Oxygen Permeation Analyser 8500 from Systech Instruments (Metrotec S.A, Spain) at 23°C.

Pure oxygen (99.9%) was introduced into the upper half of the chamber while nitrogen was injected into the lower half, where an oxygen sensor was placed. The oxygen volumetric flow rate per unit area of the membrane (*OTR*, cm^3 m^{-2} day^{-1}) was continuously monitored until a steady state was reached. The permeability coefficient is dependent on the film thickness and proportional to *OTR*·*e* (*e* = thickness, mm). Therefore, the *OTR*·*e* values were used to compare the oxygen barrier properties of the films. All samples were analyzed in triplicate.

Water Vapor Permeability coefficient (*WVP*) was determined gravimetrically using the ASTM E96/E96 M-05 [24] standard and it was calculated in kg·m·Pa^{-1}·s^{-1}·m^{-2} by using Equation (2):

$$WVP = \frac{WVT \cdot e}{\Delta P} \quad (2)$$

where WVT (kg·s^{-1}·m^{-2}) is the water vapor transmission rate through an average film thickness e (m) and ΔP is the vapor pressure difference between the two sides of the specimens (Pa), calculated by using Equation (3):

$$\Delta P = S\,(R_1 - R_2) \quad (3)$$

where S is the saturation vapor pressure at the testing temperature (Pa) and R_1, R_2 are the relative humidity of the climate chamber and inside the dish, respectively. WVP tests were performed using the desiccant method, where samples (90 mm diameter circles) were sealed with paraffin to the test stainless steel dishes containing anhydrous calcium chloride (pre-dried at 200°C for 2 h) as desiccant agent. These dishes were placed in a climate chamber at 23±1°C and RH 50±2%, and were weighed periodically until the steady state was reached. The weight change in the dishes compared with the initial mass G, (±0.001 g), was plotted versus time at 24 h intervals, t (h). Linear regression was used to calculate the slope of a fitted straight line (G/t) allowing the WVT calculation by using Equation (4):

$$WVT = \frac{G/t}{A} \quad (4)$$

Where A is the effective area of the test film (0.01 m^2). All values reported in this study are the average of three replicate samples (n = 3) ± standard deviation (SD).

2.3.7. Migration tests

Overall migration tests for all materials were performed in two liquid food simulants: ethanol 10% (v/v) (simulant A) in agreement with the Commission Regulation EU N° 10/2011 [25] and isooctane (alternative simulant to D2) according to the Commission Directive 2002/72/EC [26]. Rectangular sheets of 2.5×10 cm^2 were totally immersed in 25 mL of food simulant in both cases in triplicate. Whereas the most common use of a material for contact with food is at room temperature for more than one day, the test conditions selected were more restrictive, as indicated in the current legislation. Samples in ethanol 10% (v/v) were kept in an oven at 40°C for 10 days, while samples in isooctane were kept in a climate chamber at 20°C for 2 days. After the contact time, films were removed and the simulants were totally evaporated and dried in an oven at 105°C for 30 minutes. Mass of the non-volatile residue was determined with an analytical balance (±0.1 mg accuracy) until constant weight (±0.5 mg) to determine the overall migration value in mg·kg^{-1} of simulant. All overall migration values of samples are the average of three determinations (n = 3) ± standard deviation (SD).

2.3.8. Statistical analysis

Analysis of variance (ANOVA) for barrier properties and migration tests and significance in the data differences were carried out by using SPSS statistics 22.0 software. Tukey's multiple sample comparison method with a 95% confidence level ($p < 0.05$) was used to identify which data groups were significantly different from others.

3. Results and discussion

In order to analyze the stability of the OLA during the processing conditions, a thermogravimetric test in isothermal conditions (air atmosphere at 200°C, for 30 min) was performed to simulate the processing thermal profile (Figure 1). Some weight losses for pure OLA were observed at 200°C, but they were moderate in comparison with other plasticizers for PLA used in previous works in the research group [27, 28]. No significant phase separation should be expected at the selected concentrations, giving evidence of the thermal resistance of this plasticizer under the processing conditions selected for these blends.

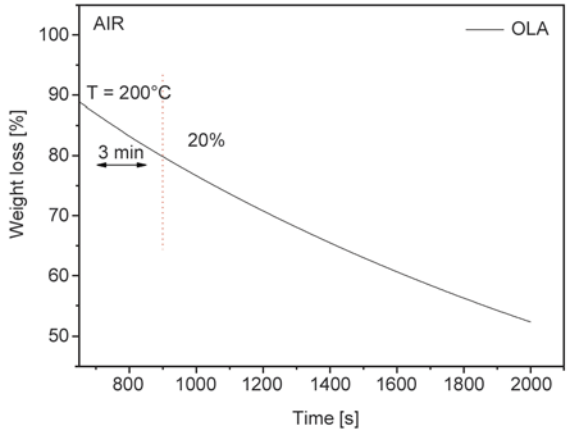

Figure 1. OLA isothermal test in air at 200°C, for 30 min

Hence PLA, PLA_PHB and PLA_PHB_OLA films were successfully developed by extrusion process, with the selected process parameters.

3.1. Transparency and microstructure

The visual appearance and transparency of PLA and PLA_PHB based blends after the optimized extrusion process were investigated and summarized in Figure 2. Images underline that all the produced samples appeared colourless and maintained the good and typical transparency of the PLA matrix, also in the case of the higher content of OLA.

Figure 3 gives the FESEM images of the fracture surface of the films, for the neat PLA, PLA_PHB blend and the plasticized (PLA_PHB_OLA) samples with various OLA concentrations, at different resolutions. Neat PLA showed a smooth and uniform surface typical of a semicrystalline polymer. FESEM images of PLA_PHB films underlined that the dispersed PHB phase had relatively small average diameter and, with a typical sea-island morphology, where the discrete PHB spherical domains are dispersed in the PLA polymer matrix. With the addition of OLA, the size of the PHB domains reduced remarkably.

Moreover, the blend system showed better interfacial adhesion between both phases in the presence of the plasticizer. This indicates that the addition of OLA improved the interfacial properties of the immiscible PLA_PHB blend, with similar results to those obtained by adding a compatibilizer.

On the other hand, the surface of the specimens with OLA showed a different aspect. Shear-yield and plastic deformation formed on the fracture surfaces of OLA based blends were observed, especially for the system with the highest plasticizer content (Figure 3). Plastic deformation and the different fracture directions required more energy and thus the materials with OLA should have higher toughness.

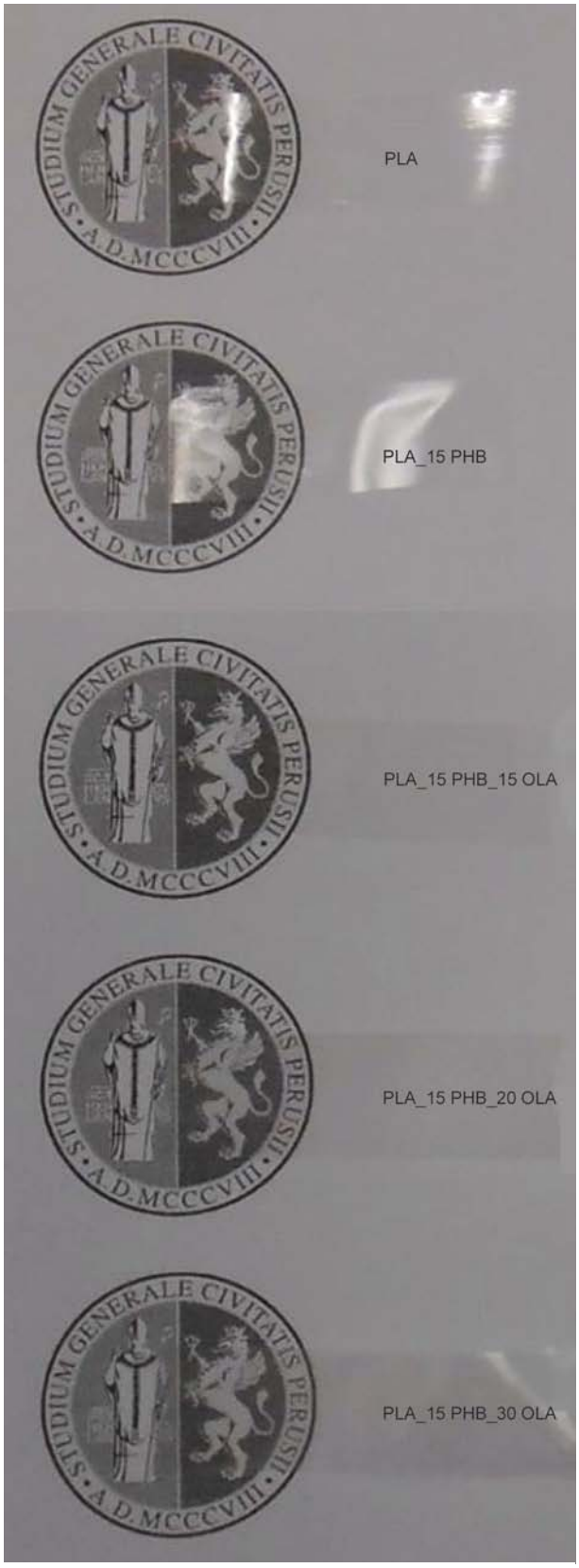

Figure 2. Images of neat PLA, PLA_PHB, and PLA_PHB_OLA films

3.2. X-ray diffraction (XRD)

Figure 4 shows the diffraction patterns of neat PLA, and ternary PLA_PHB_OLA films. In the case of the neat PLA film, a diffraction peak at $2\theta = 16.5°$ was observed, which corresponds to the characteristic peak of PLA [12, 20] and indicates the development of a certain crystallinity degree after processing. The diffraction patterns of PLA_PHB, showed amorphous structure at room temperature with no diffraction peaks other than the amorphous halo. This result could be explained by the low PHB content in the PLA matrix and the interaction between both biopolymers, reducing their crystal-

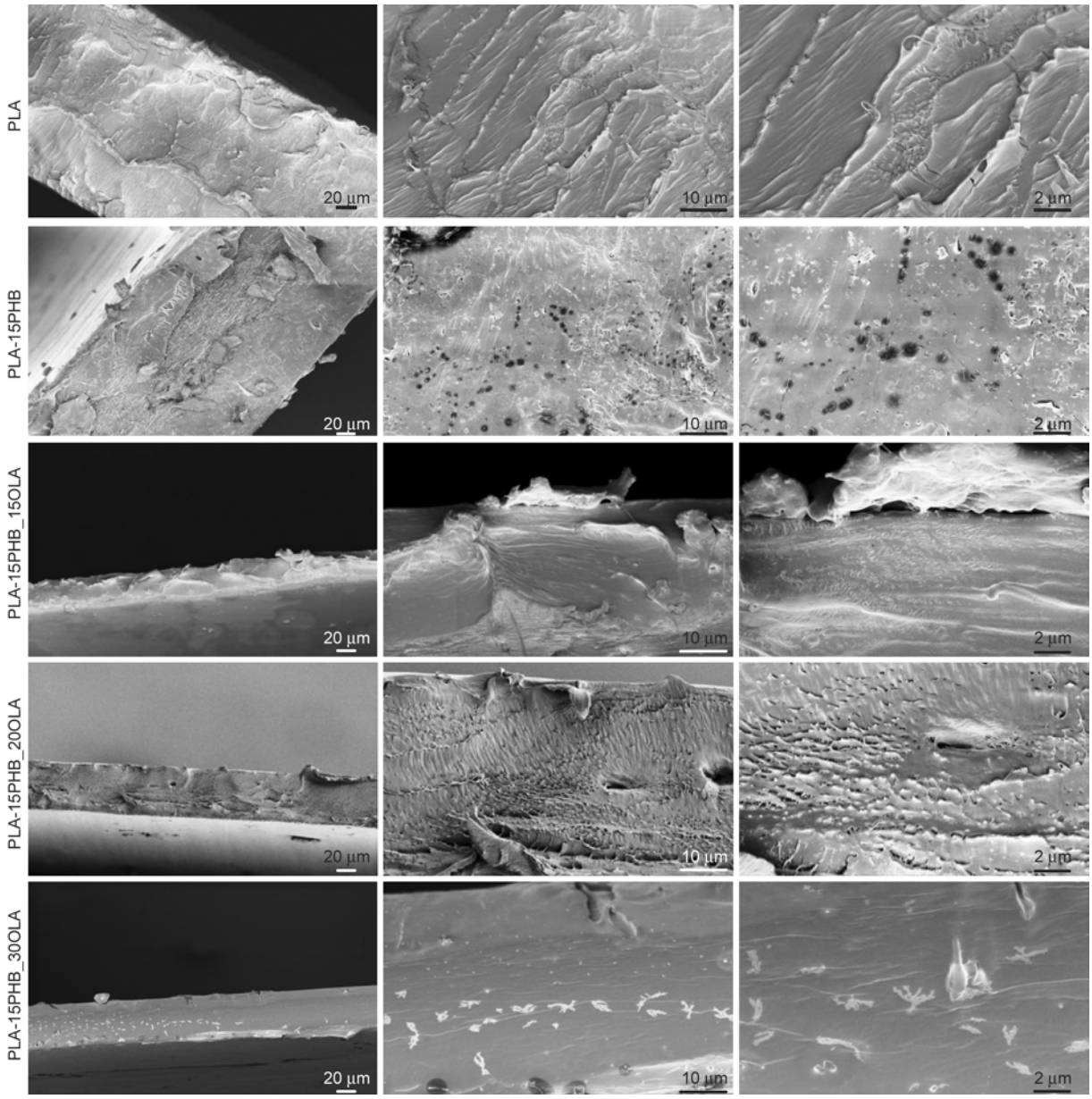

Figure 3. FESEM images of PLA, PLA_PHB and PLA_PHB_OLA films at different resolution and OLA concentration

lization rate, as other authors observed for this blends [12]. However, the addition of OLA induced the development of crystallinity, which was higher with the plasticizer content (Figure 4). In the PLA_15PHB_15OLA film two diffraction peaks at 2θ = 13.5 and 27.2° (with lower definition) were observed. The first one corresponds to the characteristic peak of PHB crystallinity, while the other characteristic peak of this polymer (2θ = 17°) was overlapped by the peak at 2θ = 16.5° attributed to PLA [4, 16]. The intensity of these peaks increased for 20 and 30 wt% OLA content and the band at 30.1° became more defined. Furthermore, one additional peak at 19.8° was observed for higher OLA concentrations. These results imply that the presence of OLA improved the interaction between PLA and PHB and consequently the development of crystallinity in the blends structure, with a clear

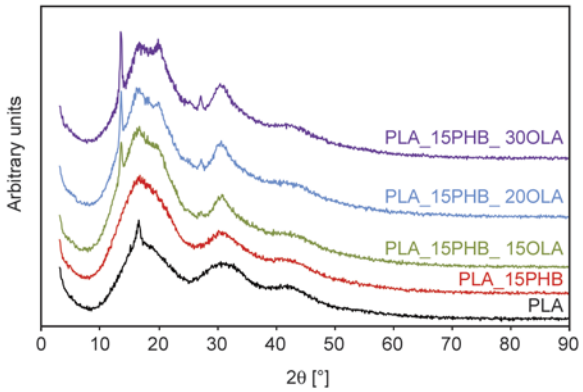

Figure 4. X-Ray diffraction patterns of PLA, PLA_PHB and PLA_PHB_OLA films

incidence on the mechanical properties of these blends.

3.3. Thermal analysis

Differential scanning calorimetry (DSC) analysis of different formulations was conducted in order to determine the effect of the OLA introduction and content on the glass transition temperature (T_g), and on crystallization and melting phenomena of PLA_PHB based systems. DSC thermograms at the first heating, cooling and second heating scan are reported in Figure 5a, 5b and 5c respectively, while the thermal properties of the PLA, PLA_PHB and PLA_PHB_OLA ternary systems after processing are summarized in Table 2.

The thermogram of neat PLA during the first heating scan displayed the glass transition temperature, the cold crystallization exotherm with its maximum at T_{cc} and the melting endotherm at T_m (Figure 5a). The T_g value for PLA neat film was about 60°C, while the exothermic peak was observed at about 95°C and the melting endothermic peak was obtained at about 150°C. In depth analysis, these thermograms revealed a sharp endothermic peak associated to the glass transition, typically attributed to the enthalpy relaxation on heating mostly due to the previous physical aging of the polymer. Moreover, during the cooling scan (Figure 5b) no exothermic crystallization peaks were obtained for PLA and this behaviour was also detected for all the PLA-based systems; the slight change in the baseline observed between 30 and 53°C was attributed to the glass transition (Figure 5b). DSC thermograms for the PLA_PHB blend underlined a slightly shift to lower T_g values with respect to neat PLA while the PLA_PHB blend showed a multi-step melting process with the first and second peaks (T'_m and T''_m) due to the PLA component and the third one (T'''_m) corresponding to the melting of PHB component measured at 173°C, in the pristine pellets, suggesting no complete miscibility between both polymers [4]. Moreover, the double melting peak at around 145–150°C and related to the PLA component could be attributed to the formation of different crystal structures. The same behavior was detected also for the second heating scan (Figure 5c).

As expected, the addition of OLA produced a significant reduction on the T_g values of PLA_PHB blends, clearly evident in both first heating and cooling scan. This effect could be explained by the plasticizing effect of OLA resulting in the increase of the molecular mobility of the polymer structure and lower glass transition temperatures. Furthermore, the OLA presence increased the ability of PLA to crystallize confirming the XRD results. This effect was evidenced by the increase of the exothermic peak corresponding to cold crystallization, with a shift to higher T_{cc} values on the ternary PLA_PHB_OLA systems, and by the crystallinity degree values reported

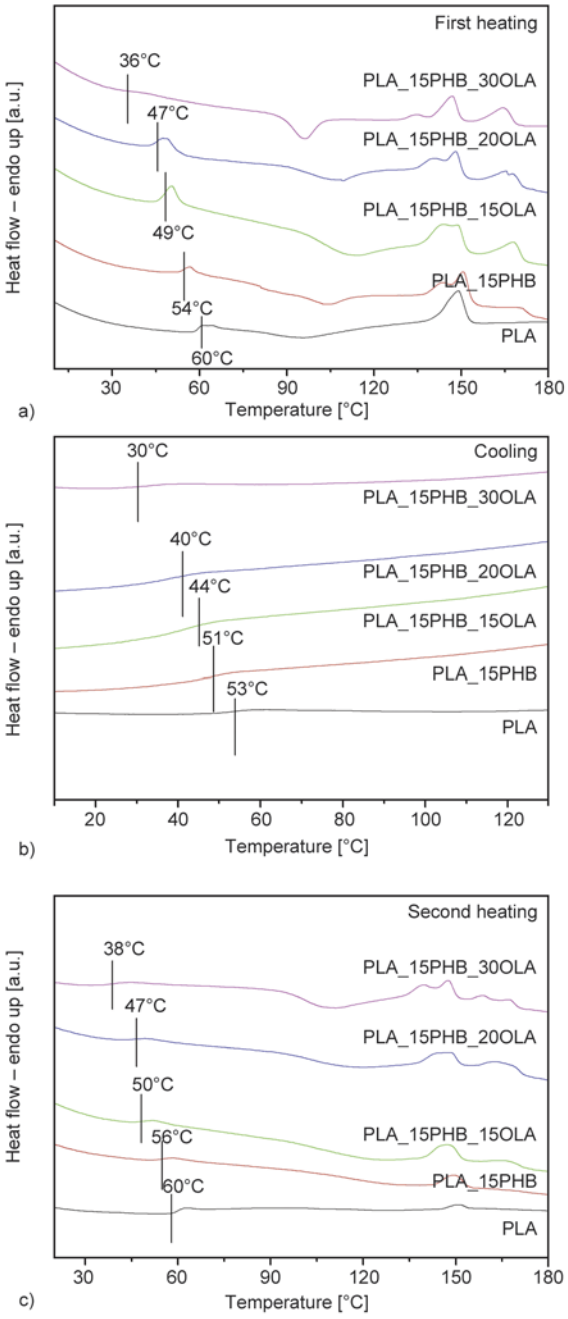

Figure 5. DSC thermograms for PLA, PLA_PHB and PLA_PHB_OLA based systems at the first heating after processing (a), during the cooling scan (b) and at the second heating scan (c).

Table 2. Thermal properties of PLA, PLA_PHB binary and PLA_PHB_OLA ternary systems at the first heating scan, after processing

Materials	T_g [°C]	T_{cc} [°C]	ΔH_{cc} [J·g^{-1}]	T'_m [°C]	T''_m [°C]	T'''_m [°C]	ΔH_m [J·g^{-1}]	X_c [%]
PLA	60.1±1.0	95.1±0.8	15.8±0.7	150.0±0.5	–	–	27.6±0.4	12.7±0.8
PLA_15PHB	55.4±1.2	103.6±0.5	9.3±0.6	144.0±0.9	150.2±0.5	170.4±1.0	25.4±0.5	20.4±0.7
PLA_15PHB_15OLA	49.4±1.4	111.5±0.3	19.1±0.8	143.4±0.2	148.4±0.7	167.9±0.5	27.6±0.8	13.1±1.0
PLA_15PHB_20OLA	47.2±1.3	107.7±0.5	18.2±0.7	140.7±0.2	148.1±0.5	166.8±0.5	33.2±0.4	24.8±0.8
PLA_15PHB_30OLA	36.2±1.4	95.6±0.5	22.6±0.7	134.6±0.5	146.1±0.6	164.8±0.5	34.1±0.2	22.5±0.8

in the Tables 2. Furthermore, the increase in chain mobility of PLA with a higher amount of OLA shifted the melting temperatures (T_m) to lower values (Table 2) and also the T'''_m, related to the PHB melting, was shifted to lower temperatures by the presence of OLA [20]. It is also assumed that OLA does not crystallize after processing and does not interfere in the PLA and PLA_PHB crystallization process, since just low-intensity melting peak at around 78°C was observed in the DSC thermogram in the first heating scan. No further crystallization and melting peaks were observed during the second heating scan.

Thermogravimetric analysis was also performed in order to establish the effect of OLA introduction on the PLA_PHB system thermal stability and the weight loss derivative curves (DTG) for neat PLA, PLA_PHB blend and PLA_PHB_OLA based formulations are reported in Figure 6.

Neat PLA film decomposed in a single step process with a maximum degradation peak (T_{max}) at 361°C, in agreement with values previously reported after processing [29] while a two-steps degradation behaviour was observed in the case of the PLA_PHB blend and the ternary PLA_PHB_OLA systems with a first peak at lower temperatures (around 280°C)

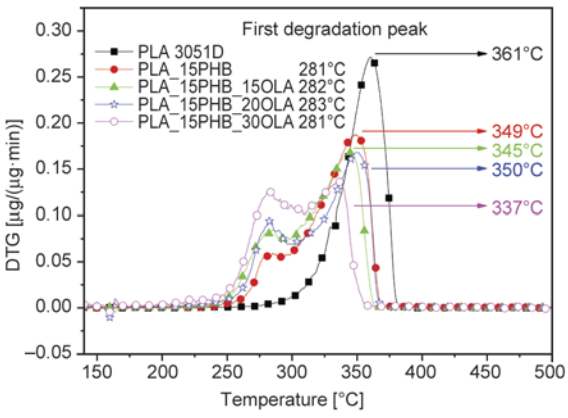

Figure 6. Thermogravimetric analysis of PLA, PLA_PHB and PLA_PHB_OLA based systems under nitrogen atmosphere

due to the PHB thermal degradation and a second degradation peak at higher temperatures attributed to the PLA degradation. Moreover, a shift to lower temperatures of the main degradation peak was detected for the PLA_PHB blend (T_{max} = 349°C) when compared to neat PLA. It should be noted that the introduction of OLA at 15 and 20 wt% did not result in a significant change in the PLA_PHB thermal stability (T_{max} = 345 and 350°C, respectively), ensuring the wide processing window with no risk of thermal degradation. However, a more evident decrease (about 15°C in the main degradation peak) was observed for the PLA_15PHB_30OLA (T_{max} = 337°C) blend respect to PLA_PHB formulation and an increase of the intensity of the first degradation peak (at lower temperature) was registered for all PLA_PHB_OLA systems with the increased OLA content that can modify the thermal stability of the system.

3.4. FTIR analysis

Figure 7 shows the FTIR spectra of the PLA, PLA_PHB and PLA_PHB_OLA films in the 2000–600 cm^{-1} region (Figure 7a) and in the 1900–1600 cm^{-1} region (Figure 7b). FTIR spectra displayed the typical absorption bands of PLA based systems. Several absorption bands specific for PHB and PLA were detected. Since differences in the initial crystallinity of polymers should be considered (PLA is primarily amorphous, whereas PHB is highly crystalline), the ν(C=O) band widths for PLA and PHB differed significantly. FTIR spectra showed a strong peak at 1755 cm^{-1}, which is related to the amorphous carbonyl stretching vibration of PLA and remains constant in all the PLA_PHB blends. In addition, a sharp peak at 1723 cm^{-1} was observed in the spectra of PHB-containing systems. This peak is attributed to the stretching vibrations of crystalline carbonyl groups. The FTIR spectra of PLA_PHB blends showed the two major carbonyl stretching bands due to PLA and PHB, respectively,

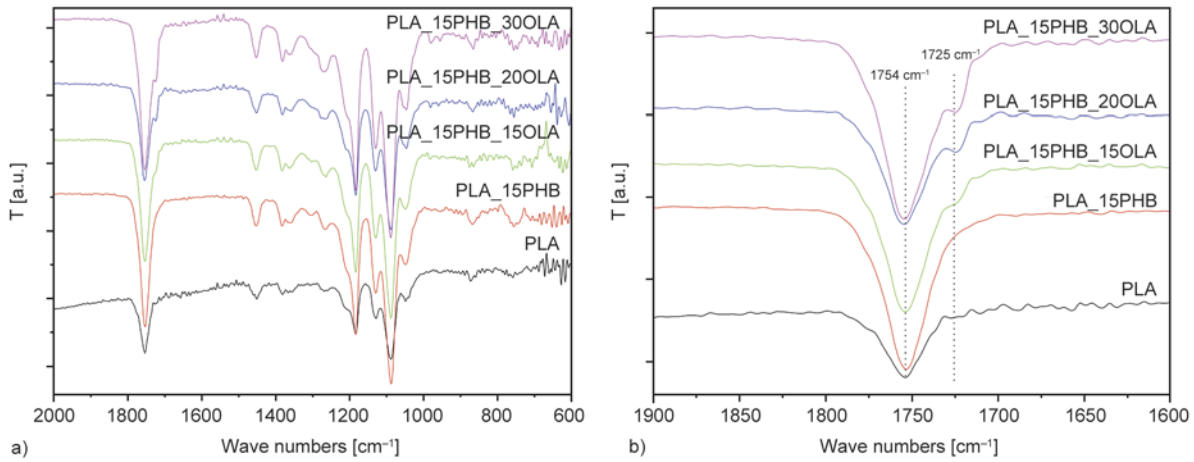

Figure 7. FT-IR spectra of PLA, PLA_PHB, and PLA_PHB_OLA films in ATR mode in the 2000–600 cm^{-1} frequency range (a) and 2000–1600 cm^{-1} (b).

and it was noticed that the intensity ratio of these two bands changed with the composition ratio [30]. As the OLA content was increased, the stretching vibrations of crystalline carbonyl groups increased gradually. However, no changes in the main carbonyl peak, which corresponds to PLA, were observed. This result indicates that PLA_PHB_OLA blends may be more easily crystallized as its proportion in the composite increased, forming phase-separated domains in the PLA matrix, and confirmed the DSC results.

3.5. Mechanical properties

The results of mechanical analysis for PLA, PLA_PHB and ternary PLA_PHB_OLA films are summarized in Table 3 and representative stress-strain curves are reported in Figure 8. As expected, the addition of the OLA plasticizer caused a substantial decrease in the materials toughness [21]. A progressive reduction in the elastic modulus was observed with the increase of the OLA content, when compared to neat PLA and PLA_PHB blends for 15, 20 and 30 wt% OLA content, evidencing the decrease in rigidity for the plasticized compositions.

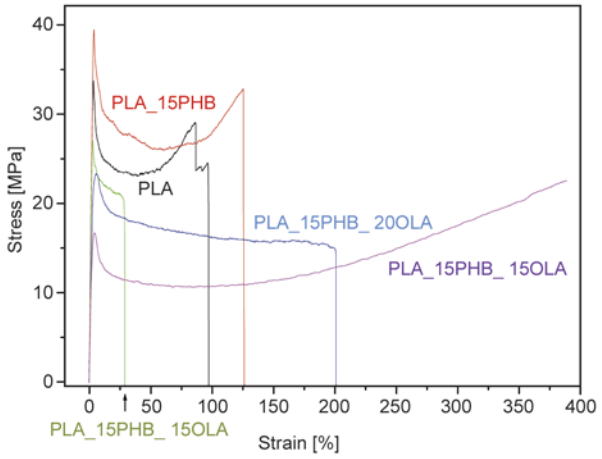

Figure 8. Representative stress-strain curve for the studied formulations

The higher modulus reduction was obtained at 30 wt% of OLA. In the meantime, the elongation at break of PLA_PHB films strongly increased with the addition of OLA (Table 3), showing an important enhancement in blends ductility that was well correlated with the decrease in T_g observed in DSC curves (Figure 5) and with the microstructure of the fracture surface analyzed by FESEM in Figure 3. The elongation at break increased to values as high as 400%, indicating that the properties of PLA_PHB

Table 3. Results from tensile test for PLA, PLA_PHB and PLA_PHB_OLA systems

Samples	Mechanical properties				
	σ_Y [MPa]	ε_Y [%]	σ_b [MPa]	ε_b [%]	E_{Young} [MPa]
PLA	40±7[a]	3.4±0.4	35±6[a]	100±30[a]	1300±180[a]
PLA_15PHB	40±5[a]	3.8±0.5	31±5[a]	140±60[a,c]	1220±140[a]
PLA_15PHB_15OLA	31±3[b]	3.1±0.3	23±2[b]	35±14[b]	1120±60[a,c]
PLA_15PHB_20OLA	23±4[c]	3.3±0.9	18±3[b]	220±100[c]	950±130[d]
PLA_15PHB_30OLA	16±3[d]	3.9±0.4	19±3[b]	370±20[d]	590±50[e]

[a–e]Different superscripts within the same column indicate significant differences between formulations ($p < 0.05$)

films can be easily tuned from rigid to ductile. Films with 30 wt% OLA showed the highest elongation at break and homogeneity, since we measured low values of standard deviations. This behaviour could be explained by the reduction of the macromolecular chains cohesion when the plasticizer penetrates through the polymer matrix [16, 20].

3.6. Barrier properties

It was observed that the addition of 15 wt% PHB to the PLA matrix induced a significant reduction ($p < 0.05$) in *OTR·e* value of PLA film of ca. 35 %. This positive effect in the oxygen barrier properties could be caused by the increase in the PLA crystallinity by the addition of a highly crystalline biopolymer, such as PHB, previously discussed in the DSC analysis and already reported by Arrieta *et al*. [5].

The introduction of 20 wt% of OLA to the PLA_PHB blend induced a significant ($p < 0.05$) increase in the *OTR·e* values up to ca. 70%. This result could be caused by the increase in the free volume of the PLA_PHB matrix by the addition of the plasticizer and it could explain the reduction in the resistance of this plasticized film to oxygen transmission, as reported by other authors for the same polymer blends [5, 24, 20, 31]. However, the increase in the OLA content up to 30 wt% showed no significant differences ($p < 0.05$) in *OTR·e* values comparing with PLA_PHB blends. This result could be explained by the development of higher PLA crystallinity in the PLA_15PHB_30OLA blend, as stated by the X-ray diffraction and DSC analysis. This increase in crystallinity and difference revealed in the crystallization phenomena could induce higher tortuosity for the oxygen molecules path through the polymer film, counteracting the decrease in the resistance of this film to oxygen transmission caused by the introduction of the plasticizer.

It is interesting to compare these *OTR·e* results for PLA_PHB blends with those obtained for other polymers currently used in food packaging applications, such as low density polyethylene (LDPE) and polyethylene terephthalate (PET). All PLA_PHB formulations showed lower *OTR·e* values than those obtained for LDPE (around 160 $cm^3 \cdot mm \cdot m^{-2} \cdot day^{-1}$), but they were higher than those for PET (around 3 $cm^3 \cdot mm \cdot m^{-2} \cdot day^{-1}$), indicating that the PLA_PHB blends could be acceptable for such applications with medium oxygen barrier. In addition, it should be highlighted that plasticized formulations showed *OTR·e* results lower than those obtained in a previous work for PLA plasticized with OLA at 15, 20 and 25 wt% under the same experimental conditions [20].

Table 4. Oxygen Transmission Rate per film thickness (*OTR·e*) and Water Vapor Permeability (*WVP*) coefficients for PLA, PLA_PHB and PLA_PHB_OLA systems

Samples	Barrier properties	
	OTR·e **[$cm^3 \cdot mm \cdot m^{-2} \cdot day^{-1}$]**	***WVP*·10^{14}** **[$kg \cdot m \cdot Pa^{-1} \cdot s^{-1} \cdot m^{-2}$]**
PLA	22.9±0.4[a]	1.88±0.21[a]
PLA_15PHB	14.9±0.8[b]	1.54±0.21[a,c]
PLA_15PHB_20OLA	25.5±2.1[a]	1.19±0.04[b,c]
PLA_15PHB_30OLA	18.6±1.4[b]	0.97±0.13[b]

[a–c]Different superscripts within the same column indicate significant differences between formulations ($p < 0.05$)

Water vapour permeability coefficients determined for the same blends are also summarized in Table 4. No significant reduction ($p < 0.05$) in *WVP* of PLA was observed after the addition of 15 wt% PHB as well as in *WVP* data for PLA_PHB blends with 20 wt% OLA. However, a positive effect in the water vapour barrier properties was detected for the PLA_PHB films plasticized with 30 wt% OLA, with a reduction ca. 37% ($p < 0.05$) in the *WVP* value of the unplasticized PLA_PHB film. Several counteracting factors, in different degree, could affect the water vapour permeability of these samples. As already discussed from the *OTR·e* results, the addition of OLA in high concentrations increases the free volume available in the PLA_PHB structure, reducing the resistance of films to water vapour transmission. But, in contrast, the development of crystallinity and the increase in the material hydrophobic character caused by OLA results in some decreases in *WVP* coefficients, inducing a positive effect in the barrier properties to water vapour.

In summary, it can be concluded that the addition of 30 wt% OLA enhanced significantly ($p < 0.05$) the oxygen and water vapour barrier properties of neat PLA and PLA_PHB composites by the development of crystalline structures in these blends.

3.7. Migration properties

One of the necessary conditions for a polymeric material to be used in food packaging applications is their overall migration limit, which should be lower than those limits established in the current legislation (European Commission Regulation, 2011) [27], ensuring that the total amount of non-volatile

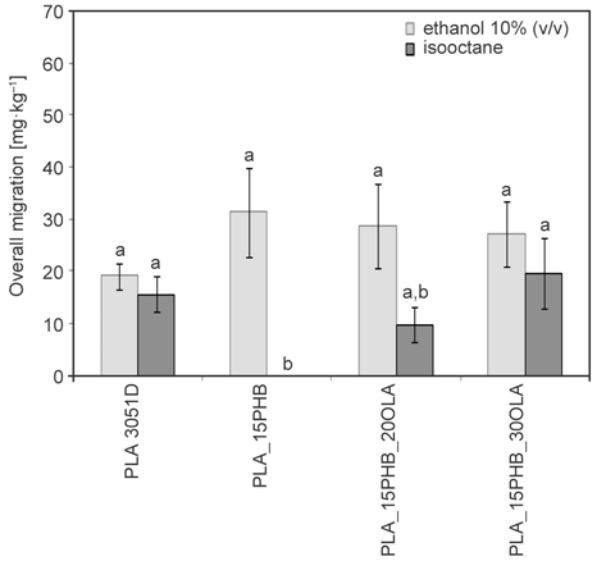

Figure 9. Overall migration values in ethanol 10% (v/v) and isooctane for PLA and PLA_PHB based systems. Different superscripts on the bars indicate significant differences between samples ($p < 0.05$).

substances that might transfer into foodstuff from polymers does not represent a risk to the consumer. The overall migration values of PLA and PLA_PHB composites in ethanol 10% (v/v) and isooctane were compared in Figure 9. It was observed that in all cases, the overall migration values in both food simulants were lower than the legislative limit 60 mg·kg^{-1}.

In the case of ethanol 10% (v/v), no significant differences ($p < 0.05$) were observed between the overall migration values for all samples. However, considering results obtained in the isooctane simulant, it was noted that the addition of PHB to the PLA matrix reduced significantly (not detected data, $p < 0.05$) the overall migration to values lower than the limit of detection of the used method, while plasticized samples showed similar values ($p < 0.05$) than neat PLA.

In general terms, overall migration in ethanol 10% (v/v) was higher than in isooctane for PLA_PHB and PLA_PHB_20OLA, while similar migration values in both simulants were detected for neat PLA and PLA_PHB_30OLA films. These results could be explained by the different polarity and solubility between both biopolymers, the potential migrant compounds and the food simulants. Since PLA, PHB and OLA are non-polar compounds and consequently they are insoluble in water, some other chemicals potentially present in these formulations, such as residual lactic acid and oligomers of lactic acid with low molar mass (due to the chain scission of PLA and OLA caused by processing) are polar compounds and they are water-soluble. These compounds could contribute to the total mass transfer in ethanol 10% (v/v), as reported by other authors [32–34]. It should be noted that after the migration test in ethanol 10% (v/v) all materials lost their transparency turning into opaque films. This change in their visual aspect could be due to the water absorption that produced hydrolytic degradation and chain scission, increasing the amount of low molar mass compounds able to migrate in this simulant. However, no visual changes in the surface of films immersed in isooctane were observed, and transparency was preserved after the migration test.

Another important factor is the testing temperature and total time applied to the migration test in ethanol 10% (v/v) (40°C for 10 days) and isooctane (20°C, 2 days). The first temperature is close to T_g values of these samples, as observed in DSC tests and, as a consequence, samples in ethanol 10% (v/v) could suffer some structural changes and the development of crystallinity that could facilitate the plasticizer exudation. In the case of migration in the non-polar simulant (isooctane), some increase in the migration values ($p < 0.05$) was detected at high OLA concentrations in the PLA_PHB blend. The non-polar nature of this plasticizer and its relative low average molar mass could explain this result, allowing their release in the food simulant.

4. Conclusions

Binary and ternary films made of PLA, PHB and OLA were successfully prepared under optimized extrusion conditions, followed by a filmature procedure. Mechanical, thermal, morphological and functional properties were investigated as a function of the OLA composition ratio and the adequate formulation was selected to get the desired performance in eco-friendly films.

The high efficiency of OLA as plasticizer was observed for PLA_PHB blends, as it caused a significant decrease on their glass transition temperature, which was well correlated with a considerable improvement of their ductile properties. A single T_g value was observed in all the studied formulations and no apparent phase separation was detected, confirming the high compatibility between OLA with the PLA_PHB matrix.

Mechanical properties underlined that the elongation at break increased as high as 400%, indicating that PLA_PHB films can be easily turned from rigid to ductile. Water vapor permeability (*WVP*) tests showed a modulation in all the system with OLA respect to neat PLA and PLA_PHB blends: *WVP* decrease in the PLA_15PHB_30OLA of 37% respect to PLA_PHB blend and of 48% respect to neat PLA films, while oxygen transmission rate (*OTR*) showed increased values respect to PLA_PHB film, but improved respect to the neat PLA films.

The improvement in the barrier properties are related with the higher crystallinity of the plasticized PLA_PHB blends ensuring a good protection to foodstuff by decreasing significantly the oxygen transmission rate and water vapor permeability values of neat PLA films.

Migration tests were performed by following the current legislation for food contact materials in both non-polar and polar simulants and no problems were observed since the obtained overall migration values were well below the legislative limit. According to the analyzed properties, the PLA_PHB blend with 30 wt% OLA was selected as the optimum formulation, since it offered the best compromise between ductile and oxygen and water vapor barrier properties, with no migration problems for perspective application as food packaging material.

Acknowledgements

This research was financed by the SAMSUNG GRO PROGRAMME 2012.

References

[1] Arrieta M. P., Fortunati E., Dominici F., Rayón E., López J., Kenny J. M.: PLA-PHB/cellulose based films: Mechanical, barrier and disintegration properties. Polymer Degradation and Stability, **107**, 139–149 (2014).
DOI: 10.1016/j.polymdegradstab.2014.05.010

[2] Lim J. S., Park K-I., Chung G. S., Kim J. H.: Effect of composition ratio on the thermal and physical properties of semicrystalline PLA/PHB-HHx composites. Materials Science and Engineering: C, **33**, 2131–2137 (2013).
DOI: 10.1016/j.msec.2013.01.030

[3] Boufarguine M., Guinault A., Miquelard-Garnier G., Sollogoub C.: PLA/PHBV films with improved mechanical and gas barrier properties. Macromolecular Materials and Engineering, **298**, 1065–1073 (2013).
DOI: 10.1002/mame.201200285

[4] Arrieta M. P., Fortunati E., Dominici F., Rayón E., López J., Kenny J. M.: Multifunctional PLA–PHB/cellulose nanocrystal films: Processing, structural and thermal properties. Carbohydrate Polymers, **107**, 16–24 (2014).
DOI: 10.1016/j.carbpol.2014.02.044

[5] Arrieta M. P., Samper M. D., López J., Jiménez A.: Combined effect of poly(hydroxybutyrate) and plasticizers on polylactic acid properties for film intended for food packaging. Journal of Polymers and the Environment, **22**, 460–470 (2014).
DOI: 10.1007/s10924-014-0654-y

[6] Arrnentano I., Bitinis N., Fortunati E., Mattioli S., Rescignano N., Verdejo R., López-Manchado M. A., Kenny J. M.: Multifunctional nanostructured PLA materials for packaging and tissue engineering. Progress in Polymer Science, **38**, 1720–1747 (2013).
DOI: 10.1016/j.progpolymsci.2013.05.010

[7] Madhavan Nampoothiri K., Nair N. R., John R. P.: An overview of the recent developments in polylactide (PLA) research. Bioresource Technology, **101**, 8493–8501 (2010).
DOI: 10.1016/j.biortech.2010.05.092

[8] Rasal R. M., Janorkar A. V., Hirt D. E.: Poly(lactic acid) modifications. Progress in Polymer Science, **35**, 338–356 (2010).
DOI: 10.1016/j.progpolymsci.2009.12.003

[9] Fan Y., Nishida H., Shirai Y., Tokiwa Y., Endo T.: Thermal degradation behaviour of poly(lactic acid) stereocomplex. Polymer Degradation and Stability, **86**, 197–208 (2004).
DOI: 10.1016/j.polymdegradstab.2004.03.001

[10] Noda I., Satkowski M. M., Dowrey A. E., Marcott C.: Polymer alloys of nodax copolymers and poly(lactic acid). Macromolecular Bioscience, **4**, 269–275 (2004).
DOI: 10.1002/mabi.200300093

[11] Zhang L., Xiong C., Deng X.: Miscibility, crystallization and morphology of poly(β-hydroxybutyrate)/poly (*D,L*-lactide) blends. Polymer, **37**, 235–241 (1996).
DOI: 10.1016/0032-3861(96)81093-7

[12] Zhang M., Thomas N. L: Blending polylactic acid with polyhydroxybutyrate: The effect on thermal, mechanical, and biodegradation properties. Advances in Polymer Technology, **30**, 67–79 (2011).
DOI: 10.1002/adv.20235

[13] Bucci D. Z., Tavares L. B. B., Sell I.: PHB packaging for the storage of food products. Polymer Testing, **24**, 564–571 (2005).
DOI: 10.1016/j.polymertesting.2005.02.008

[14] Arrieta M. P., del Mar Castro-López M., Rayón E., Barral-Losada L. F., López-Vilariño J. M., López J., González-Rodríguez M. V.: Plasticized poly(lactic acid)–poly(hydroxybutyrate) (PLA–PHB) blends incorporated with catechin intended for active food-packaging applications. Journal of Agricultural and Food Chemistry, **62**, 10170–10180 (2014).
DOI: 10.1021/jf5029812

[15] Imre B., Pukánszky B.: Compatibilization in bio-based and biodegradable polymer blends. European Polymer Journal, **49**, 1215–1233 (2013).
DOI: 10.1016/j.eurpolymj.2013.01.019

[16] Abdelwahab M. A., Flynn A., Chiou B-S., Imam S., Orts W., Chiellini E.: Thermal, mechanical and morphological characterization of plasticized PLA–PHB blends. Polymer Degradation and Stability, **97**, 1822–1828 (2012).
DOI: 10.1016/j.polymdegradstab.2012.05.036

[17] Ljungberg N., Wesslén B.: Preparation and properties of plasticized poly(lactic acid) films. Biomacromolecules **6**, 1789–1796 (2005).
DOI: 10.1021/bm050098f

[18] Kulinski Z., Piorkowska E.: Crystallization, structure and properties of plasticized poly(L-lactide). Polymer, **46**, 10290–10300 (2005).
DOI: 10.1016/j.polymer.2005.07.101

[19] Martin O., Avérous L.: Poly(lactic acid): Plasticization and properties of biodegradable multiphase systems. Polymer, **42**, 6209–6219 (2001).
DOI: 10.1016/S0032-3861(01)00086-6

[20] Burgos N., Martino V. P., Jiménez A.: Characterization and ageing study of poly(lactic acid) films plasticized with oligomeric lactic acid. Polymer Degradation and Stability, **98**, 651–658 (2013).
DOI: 10.1016/j.polymdegradstab.2012.11.009

[21] Burgos N., Tolaguera D., Fiori S., Jiménez A.: Synthesis and characterization of lactic acid oligomers: Evaluation of performance as poly(lactic acid) plasticizers. Journal of Polymers and the Environment, **22**, 227–235 (2014).
DOI: 10.1007/s10924-013-0628-5

[22] Xiao H., Liu F., Jiang T., Yeh J-T.: Kinetics and crystal structure of isothermal crystallization of poly(lactic acid) plasticized with triphenyl phosphate. Journal of Applied Polymer Science, **117**, 2980–2992 (2010).
DOI: 10.1002/app.32225

[23] Fiori S., Ara P.: Method for plasticizing lactic acid polymers. World Patent WO2009092825 (2009).

[24] ASTM E96/E96M-05: Standard test methods for water vapor transmission of materials (2005).

[25] Union Guidelines on Regulation (EU) N° 10/2011 on plastic materials and articles intended to come into contact with food. Official Journal of European Communities (2011).

[26] Commission directive 2002/72/EC relating to plastic materials and articles intended to come into contact with foodstuffs. Official Journal of European Communities (2002).

[27] Martino V. P., Jiménez A., Ruseckaite R. A.: Processing and characterization of poly(lactic acid) films plasticized with commercial adipates. Journal of Applied Polymer Science, **112**, 2010–2018 (2009).
DOI: 10.1002/app.29784

[28] Martino V. P., Ruseckaite R. A., Jiménez A.: Ageing of poly(lactic acid) films plasticized with commercial polyadipates. Polymer International, **58**, 437–444 (2009).
DOI: 10.1002/pi.2556

[29] Fortunati E., Armentano I., Zhou Q., Iannoni A., Saino E., Visai L., Berglund L. A., Kenny J. M.: Multifunctional bionanocomposite films of poly(lactic acid), cellulose nanocrystals and silver nanoparticles. Carbohydrate Polymers, **87**, 1596–1605 (2012).
DOI: 10.1016/j.carbpol.2011.09.066

[30] Vogel C., Wessel E., Siesler H. W.: FT-IR imaging spectroscopy of phase separation in blends of poly(3-hydroxybutyrate) with poly(L-lactic acid) and poly(ε-caprolactone). Biomacromolecules, **9**, 523–527 (2007).
DOI: 10.1021/bm701035p

[31] Laohakunjit N., Noomhorm A.: Effect of plasticizers on mechanical and barrier properties of rice starch film. Starch-Stärke, **56**, 348–356 (2004).
DOI: 10.1002/star.200300249

[32] Martino V. P., Ruseckaite R. A., Jiménez A., Averous L.: Correlation between composition, structure and properties of poly(lactic acid)/polyadipate-based nanobiocomposites. Macromolecular Materials and Engineering, **295**, 551–558 (2010).
DOI: 10.1002/mame.200900351

[33] Vu D. T., Kolah A. K., Asthana N. S., Peereboom L., Lira C. T., Miller D. J.: Oligomer distribution in concentrated lactic acid solutions. Fluid Phase Equilibria, **236**, 125–135 (2005).
DOI: 10.1016/j.fluid.2005.06.021

[34] Höglund A., Hakkarainen M., Albertsson A-C.: Migration and hydrolysis of hydrophobic polylactide plasticizer. Biomacromolecules, **11**, 277–283 (2009).
DOI: 10.1021/bm901157h

eXPRESS Polymer Letters Vol.9, No.7 (2015) 597–607
Available online at www.expresspolymlett.com
DOI: 10.3144/expresspolymlett.2015.56

A comparative investigation on strain induced crystallization for graphene and carbon nanotubes filled natural rubber composites

*D. H. Fu, Y. H. Zhan, N. Yan, H. S. Xia**

State Key Laboratory of Polymer Materials Engineering, Polymer Research Institute, Sichuan University, 610065 Chengdu, China

Received 18 November 2014; accepted in revised form 26 January 2015

Abstract. Natural rubber containing graphene and carbon nanotubes (CNTs) composites were prepared by ultrasonically-assisted latex mixing. Natural rubber filled by both graphene and CNTs show significant enhanced tensile strength, while graphene exhibits a better reinforcing effect than CNTs. Strain-induced crystallization in natural rubber composites during stretching was determined by synchrotron wide-angle X-ray diffraction. With the addition of CNTs or graphene, the crystallization for natural rubber occurs at a lower strain compared to unfilled natural rubber, and the strain amplification effects were observed. The incorporation of graphene results in a faster strain-induced crystallization rate and a higher crystallinity compared to CNTs. The entanglement-bound rubber tube model was used to analyze the chain network structure and determine the network parameters of composites. The results show that the addition of graphene or CNTs has an influence on the molecular network structure and improves the contribution of entanglement to the conformational constraint, while graphene has a more marked effect than CNTs.

Keywords: *rubber, strain-induced crystallization, tube model, graphene, carbon nanotube*

1. Introduction

Natural rubber (NR) is used extensively in a variety of applications, due to its outstanding elastic property and good cracking resistance, arising from its ability to crystallize upon stretching [1–4]. The addition of nanoparticles offers the opportunity to render versatility in NR and extend its applications that unlikely to achieve by using NR alone. Graphene (GE) and carbon nanotubes (CNTs) are among the most fascinating nanoparticles, which have received numerous studies because of their intrinsic excellent properties [5, 6], such as high modulus [7], tensile strength [8], thermal [9, 10] and electrical conductivity [11, 12]. GE has been used to prepare NR nanocomposites by an ultrasonically assisted latex mixing and *in-situ* reduction process [13–15], the mechanical properties were significantly improved at a low content of GE [14]. The reinforcement effect of graphene is believed to be related to its effect on strain induced crystallization (SIC).

Synchrotron X-ray diffraction (WAXD) allows the *in-situ* examination of SIC in NR composites during stretching [13, 16–20]. Results from extensive studies demonstrated the preferred chain orientations and prominent enhancement of SIC upon elongation in the filled rubber composites. Song *et al*. [19] investigated the SIC of natural rubber containing various amounts of CNTs and carbon black (CB) by synchrotron X-ray scattering. It was found that the rubber containing CNTs shows early onset point of SIC and CNTs helps to orient the chains and SIC during the uniaxial stretching. However, the CB in rubber

*Corresponding author, e-mail: xiahs@scu.edu.cn

act to interrupt the SIC. Ozbas *et al.* [20] compared the effect of graphene and CB on the SIC by synchrotron X-ray scattering. The results showed that the onset of crystallization occurs at significantly lower strains for GE-filled NR samples compared with CB-filled NR Neat-NR exhibits SIC around a strain of 2.25, while incorporation of 1 and 4 wt% GE shifts the crystallization to strains of 1.25 and 0.75, respectively. In contrast, loadings of 16 wt% CB do not significantly shift the critical strain for crystallization. Despite many studies conducted on the SIC of NR, a comparative study on the influences of GE and CNTs on the SIC and rubber network parameters is still missing.

The established molecular statistical theories of crosslinked and entangled polymers assume that the restricted phase space (due to the entanglements) available to the chains only affects crosslink fluctuations. Nevertheless, these theories give no insight into the relationship between the configurational constraint of entire network chain and stress-strain behavior of crosslinked network. Edwards [21, 22] developed the concept of the tube model by conceiving that the entanglements act along the entire contour length of network chain segments. The introduction of tube model not only allows to reveal non-isotropic crosslink fluctuations to all chain segments of the network via constraining virtual tubes around the network chains, but also enables proper crosslink separation and constraint contribution to stress-strain behavior. Although the tube model has reliability in investigating stress-strain behavior to determine the network parameters of the unfilled rubber, it is not applicable in depicting the filled rubber network because of its complexity [23]. Funt [24] first proposed an entanglement bound rubber tube (EBT) model to describe the contribution of entanglement, which extends tube model to the filled system. Thereafter, EBT model has been used to describe the effect of carbon black [25] and clay [26] on the mechanical behavior of rubber. However, few works concerned on the influence of GE and CNTs on the NR network structure through the EBT model.

In this study, the influences of GE and CNTs on the strain-induced crystallization were investigated by synchrotron WAXD measurements. EBT model was used in combination with stress-strain experiments to calculate the network parameters, and then to assess the contribution of entanglement to the mechanical property. The results provide new insight into the discrepancy of the reinforcing effect between GE and CNTs.

2. Experimental

2.1. Materials

The commercial used natural rubber (NR) in this study was NR (SCR 5) from Yunnan Natural Rubber Industry Co., Ltd, Kunming, China. NR latex (NR content: 60 wt%) was purchased from Chengdu Fangzheng Co., Ltd (China). Flake Graphite with an average thickness of ~75 μm was obtained from Qingdao Dahe Graphite Co., Ltd (China). Hydroxyl multi-walled carbon nanotubes (CNTs, ~3 wt%) with a diameter of 10~20 nm were obtained from Chengdu Institute of Organic Chemistry, Chinese Academy of Sciences. Formic acid was purchased from Tianjin Bodi Chemical Reagent Co., Ltd (China). Other reagents were obtained from Chendu Kelong Chemical Reagent Company (China).

2.2. Preparation of the NR composites

NR composites containing 1.76 wt% CNTs or GE were prepared through the previous route called ultrasonically assisted latex mixing and *in-situ* reduction process [14, 15]. Firstly, natural flake graphite was oxidized to graphene oxide (GO) according to the Hummer's method [27]. Then, 2.5 mg/mL GO aqueous solution was prepared by bath sonication (KQ-250DE, 40 kHz, Kunshan Ultrasonic Instrument Co., Ltd, China) at 40°C for 1 h. Then an appropriate quantity (16.6 g) of NR latex was sequentially dispersed into the GO solution by sonication for 1 h. After the coagulation and drying process, the NR/GO latex mixture was obtained. Then hydrazine hydrate was added into the GO/NR latex and the mixture was subjected to sonication. After the coagulation and drying process, the NR/GE masterbatch was obtained. Vulcanized NR samples were prepared in an open twin roll mill at room temperature according to the recipes outlined in Table 1. The resultant compounds were compression molded into sheets at a curing temperature of 150°C and a pressure of 10 MPa for 5 min, and then cooled for 3 min under pressure at room temperature.

For a comparative purpose, the natural rubber/carbon nanotubes (CNTs/NR) composites with 1.76 wt% filler content were also prepared by a latex mixing route.

Table 1. Recipes for preparing NR and NR composites containing 1.76 wt% CNTs or GE

Samples	NR	CNTs/NR	GE/NR
Raw NR	80	80	80
NR masterbatch containing 10 wt% GE or CNT	0	20	20
Zinc oxide	5	5	5
Stearic acid	2	2	2
Sulfur	3	3	3
Antioxidant (4010NA)	2	2	2
Accelerator (CBS[a])	1.5	1.5	1.5
Accelerator (MBT[b])	0.1	0.1	0.1

[a]CBS, N-cyclohexyl-2-benzothiazole-sulfenamide
[b]MBT, 2-mercaptobenzothiazole

2.3. Characterization

Synchrotron wide-angle X-ray diffraction (WAXD) measurements were carried out at room temperature using a U7B beam-line in the National Synchrotron Radiation Laboratory, Hefei, China. The wavelength was 0.154 nm. The specimen was symmetrically stretched at a strain rate of 10 mm/min to the predetermined elongation, allowing the X-ray to irradiate almost the same specimen position. The exposure time for each image was 180 s. The two-dimensional (2D) WAXD patterns were recorded by a Mar CCD 165 X-ray detector system and analyzed by the Fit2D software package.

The tensile strength was tested using an Instron (5567) universal test machine at room temperature. The deformation rate was 500 mm/min. The initial width and thickness of those samples were 4 and 2 mm, respectively. All tests were carried out on a minimum of five samples and the reported results are average values.

The swelling behavior was tested as follows: the cured samples were cut into strips with dimensions of 30 mm×5 mm×2 mm, and then immersed in toluene at 25°C for 48 h to reach their equilibrium swelling. Afterward, the samples were dried at 60°C until constant weights were obtained. The toluene uptake per gram of rubber (Q) was determined using Equation (1):

$$Q = \frac{w_s - w_d}{w_o \cdot \varphi_{rubber}} \quad (1)$$

where w_s is the swollen weight, w_d is the dried weight, w_o is the original weight and φ_{rubber} is the mass fraction of the rubber in the composites. The filler-rubber interaction in the composite was evaluated by the Q_f/Q_g (Q_f and Q_g are the toluene uptakes per gram for filled and neat rubber respectively) [28]. The lower Q_f/Q_g value means the higher interaction extent between the filler and matrix [29].

The bound rubber content was tested based on the method reported by Leblanc and Hardy [30]. Uncured sample (0.5 g) was cut into small pieces and placed into a steel wire net (m_1). The net was closed and weighed (m_2), and then immersed in toluene at room temperature for 72 h during which the sample was washed with fresh solvent every 24 h. The net was slowly removed from the solvent and dried at 40°C under vacuum for a few hours until a constant weight (m_3) was achieved. The amount of bound rubber (as the weight percent, wt%) of the initial rubber content of the uncured sample was given by Equation (2):

$$BdR[\%] = \frac{m_0 - (m_2 - m_3)}{m_0} \cdot 100 \quad (2)$$

where m_0 is the rubber content in the sample given by $m_0 = (m_2 - m_1) \cdot \varphi_{rubber}$ (m_1 is the mass of the empty net and φ_{rubber} is the mass fraction of the rubber in the composites.), m_2 is the mass of the net plus the unextracted sample, and m_3 is the mass of the basket plus the extracted dried sample.

3. Results and discussion

3.1. Stress-strain behavior

The stress-strain curves for the unfilled NR and NR nanocomposites with GE or CNTs are shown in Figure 1. The NR exhibits marked increase in tensile strength with low contents of GE or CNTs. The tensile strength was increased by 98.4% from 12.4 MPa for unfilled NR to 24.6 MPa for the nanocomposite with 1.76 wt% GE. The NR/CNTs containing 1.76 wt% of CNTs showed a tensile strength of 18.6 MPa. It is clear that GE shows an evidently

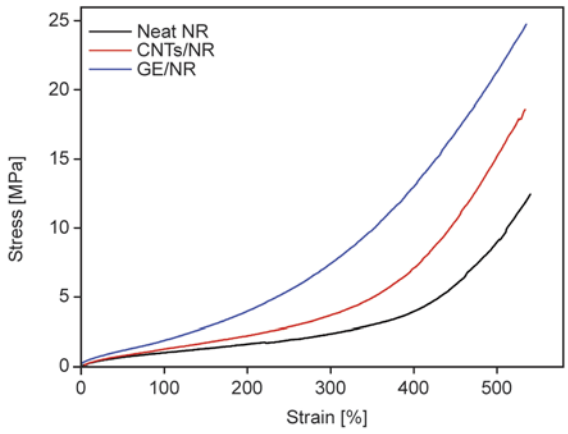

Figure 1. The stress-strain curves of filled and unfilled NR

better reinforcing effect on NR than CNTs. Additionally, both GE and CNTs at low contents exhibit the comparable reinforcing effect to the conventional filler at high loading, indicating the reinforcing advantages of nanoparticles.

In order to understand the reinforcing effect of GE and CNTs, we compared the crosslink density, bound rubber content and filler-rubber interaction of the rubber nanocomposites. The crosslink chains density (v_e) can be obtained according to Equation (3) [31]:

$$\sigma = v_e kT(\alpha - \alpha^{-2}) \quad (3)$$

where σ is the force per unit area, v_e is the crosslink chains density, k is the Boltzmann constant, T is the absolute temperature, and α is the elongation ratio ($\alpha = l/l_0$, in which l_0 is the initial length of the sample and l is that of the elongated sample). The bound rubber content was tested based on the method reported by Leblanc and Hardy [30] (Equation (2)). The filler-rubber interaction in the composites was evaluated by Q_f/Q_g. The crosslink density, bound rubber content and filler-rubber interaction are listed in Table 2. The crosslink chains density for GE/NR is more than twice higher than that of NR, also much higher than that of CNTs/NR. In addition, the GE/NR composite has a very high bound rubber content, nearly three times higher than the CNTs/NR composite, which suggests stronger interaction between GE and NR. The lower Q_f/Q_g value of NR/GE also indicates a stronger interaction between GE and NR matrix. From those data on the crosslink density, bound rubber content and filler-rubber interaction of the rubber nanocomposites, it can be understood why graphene has a much better reinforcing effect on natural rubber. In order to get deeper understanding into the reinforcing mechanism, further investigations were conducted experimentally by Synchrotron Wide-angle X-ray Diffraction and theoretically through the entanglement-bound rubber tube model.

Table 2. The crosslink density, bound rubber content and filler-rubber interaction for the filled and unfilled NR

Sample	NR	CNTs/NR	GE/NR
$v_e \cdot 10^4$ [mol/cm^3]	0.79±0.01	0.92±0.01	1.72±0.03
BdR [%]	0	11.4±0.2	30.3±0.4
Q_f/Q_g	–	0.89±0.01	0.85±0.01

3.2. Strain induced crystallization during stretching

It has long been recognized that the excellent tensile properties of NR originate from its strain-induced crystallization ability. It is of great significance to explore the relation between nanoparticles and strain induced crystallization. SIC was studied via *in-situ* synchrotron wide-angle X-ray diffraction. The 2D WAXD patterns for unfilled NR and NR containing GE or CNTs during stretching are shown in Figure 2. All images were normalized with respect to the sample thickness change, sample absorption, and beam fluctuation. The intensities of these reflections increase with strain during stretching. NR/GE composite has stronger diffraction intensity compared to unfilled NR and NR/CNTs at the same strain. The evolution of strain-induced crystallization can be identified by the linear diffraction profiles taken along the equator from the 2D WAXD patterns collected at different strains during stretching (Figure 3). The resultant peaks on the equatorial diffraction profiles were fitted with a Gaussian function (Equation (4)):

$$I(x) = h \cdot \frac{\exp[-(x - x_c)^2]}{2w^2} \quad (4)$$

where $I(x)$ is the intensity at position x, x_c is the position at the scattering maximum, and h and w are the parameters related to the peak height and peak width, respectively. It can be seen that two distinct diffraction peaks located at $2\theta \sim 15.3°$ corresponding to the 200 plane and $2\theta \sim 19°$ corresponding to the 120 plane increase with strain, and the crystallization occurred at a lower strain for GE/NR compared to that for unfilled NR and CNTs/NR composites. The equatorial reflection peak intensities of I_{eq} (200) and I_{eq} (120) were used to assess the crystallinity via quantitative evaluation in mass fractions of crystal and amorphous phase. The crystallinity calculation from the resultant Gaussian peak is described as Equation (5) [32]:

$$X_c = \frac{A_c}{A_c - A_a} \quad (5)$$

where A_c and A_a represent the integrated intensities of the crystalline and amorphous part, respectively. Figure 3b shows the variation of crystallinity with strain for unfilled NR, GE/NR and CNTs/NR com-

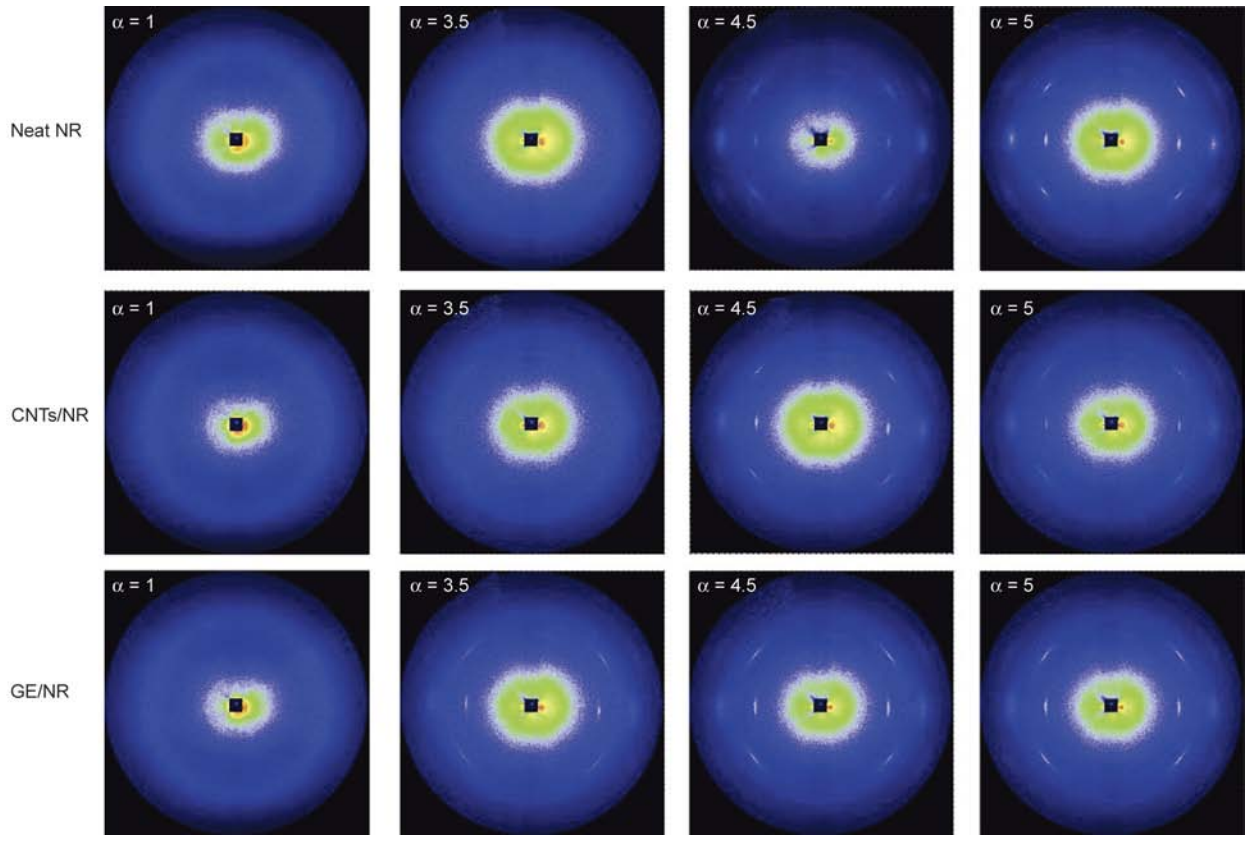

Figure 2. Sequential changes of WAXD patterns of neat NR, CNTs/NR and GE/NR

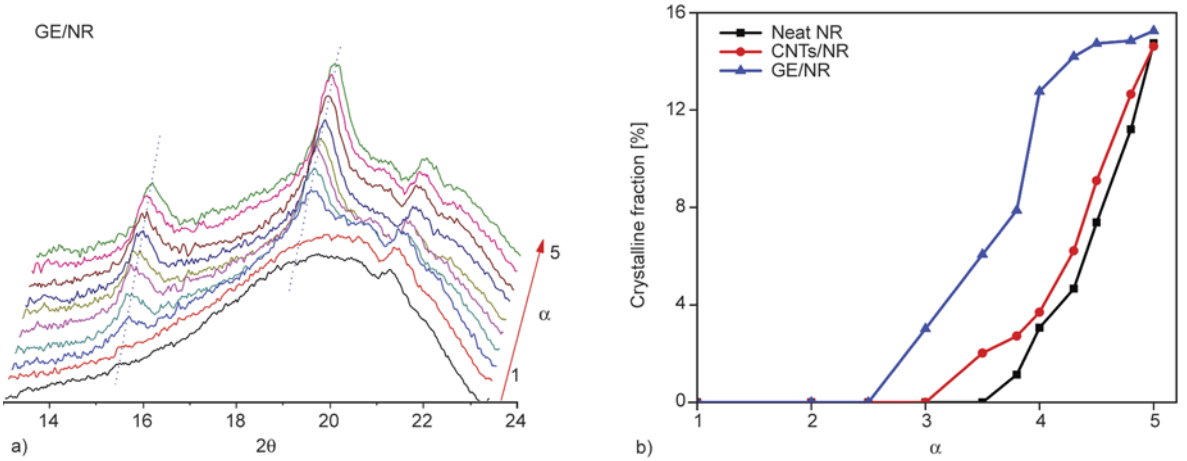

Figure 3. (a) Equatorial diffraction profiles taken from 2D WAXD patterns at selected extension ratios of GE/NR; (b) the crystallinity as a function of extension ratio for unfilled and filled NR composites

posites respectively. The crystallinity for three kinds of materials increase with respect to strain, and CNTs or GE filled NR composites exhibit higher crystallinity compared to unfilled NR at the same strain. GE/NR composite has the highest crystallinity among the three kinds of material. The crystallites formed along the chains during stretching can be regarded as quasi-fillers or alternatively as additional cross-links in the rubber network, which plays a crucial role in enhancing mechanical properties of NR.

The onset extension ratio of crystallization (α^0) was obtained by the interception of the linear regression lines derived in the plot of crystallinity against strain. The calculated α^0 value for the unfilled NR, CNTs/NR and GE/NR are 3.5, 3.0 and 2.5 respectively. It is clear that SIC occurs at a lower α^0 value in the filled NR samples, and GE/NR exhibits the lowest α^0 value among the three samples. The low α^0 value in GE/NR is thought to correlate with the high strain amplification effect of GE on NR matrix. The

Table 3. Onset extension ratios of crystallization for unfilled NR and filled NR

Samples	α^0	$\alpha_r^0(\varphi)$	$\alpha_r^0(b)$
NR	3.5	3.5	3.5
CNTs/NR	3.0	3.0	3.3
GE/NR	2.5	2.5	3.2

α^0: the experimental values, $\alpha^0(\varphi)$: the corrected values considering the filler volume fraction, and $\alpha^0(b)$: the corrected values considering the volume fraction of the fillers plus bound rubber.

effective strain of rubber portion in GE/NR is higher than the nominal macroscopic one by assuming GE un-deformable.

The relationship between the effective extension ratio and volume fraction (φ) of the filler is formulated as Equation (6) [33]:

$$\alpha_r^0(\varphi) = \frac{\alpha^0 - \varphi}{1 - \varphi} \tag{6}$$

The α^0 values are converted in terms of Equation (6), and listed in Table 3. Because of the low filler content, the corrected value $\alpha_r^0(\varphi)$ does not change compared with the experimental values (α^0). In filled rubber, the bound rubber layer around un-deformable filler particles is regarded as immobile, because of the intense physical and chemical interactions. The variation of the strain amplification effect in GE/NR and CNTs/NR composites were interpreted in terms of different bound rubber contents in the two composites. On the basis of Leblanc and Hardy's methods [30], the measured bound rubber contents for CNTs/NR and GE/NR samples are 11.4 and 30.3% (Table 2), respectively. The corrected onset strain $\alpha_r^0(b)$ considering the filler plus bound rubber volume fraction are shown in Table 3. The corrected $\alpha_r^0(b)$values for filled NR are closer to the uncorrected values α^0, but still much smaller than the onset strain of unfilled NR. The addition of filler can dominate the rubber network structure and strain amplification effect. Also the GE or CNTs particles can act as nucleation centers of the NR crystallites. Raul *et al.* [34] thought that the addition of GE or CNTs makes the chains overstrained, and the crystallization was accelerated around particles.

3.3. Lateral crystallite size

Crystallite size is an important parameter in characterizing the crystallization behavior of rubber. The widths of peaks I_{eq} (200) and I_{eq} (120) were estimated and width (w) value was converted into the half-width β_{hkl} (represented by radian) according to the procedure described by Tosaka *et al.* [35]. The crystallite size was estimated using the Scherrer equation (Equation (7)):

$$L_{hkl} = \frac{k\lambda}{\beta_{hkl}\cos\theta} \tag{7}$$

where L_{hkl} is the crystallite size in the direction perpendicular to the (hkl) plane which is parallel to the drawing direction, λ is the wavelength, and θ is the Bragg angle (half of the scattering angle). The Scherrer factor k is 0.89 when β_{hkl} is the half width of the (hkl) reflection in the radial direction [36]. Figure 4 shows the variations of the L_{200} and L_{120} crystallite sizes during stretching. Both I_{eq} (200) and I_{eq} (120) decrease with strain, this is because the mean distance between the stretched chains acting as precursor of crystallite decreases, resulting in a decrease in the average crystallite size [36]. Since both GE and CNTs can act as the nuclei to induce the formation of crystallites during stretching, the filled NR samples show smaller crystallite sizes compared to the unfilled NR at the same strain. GE/NR

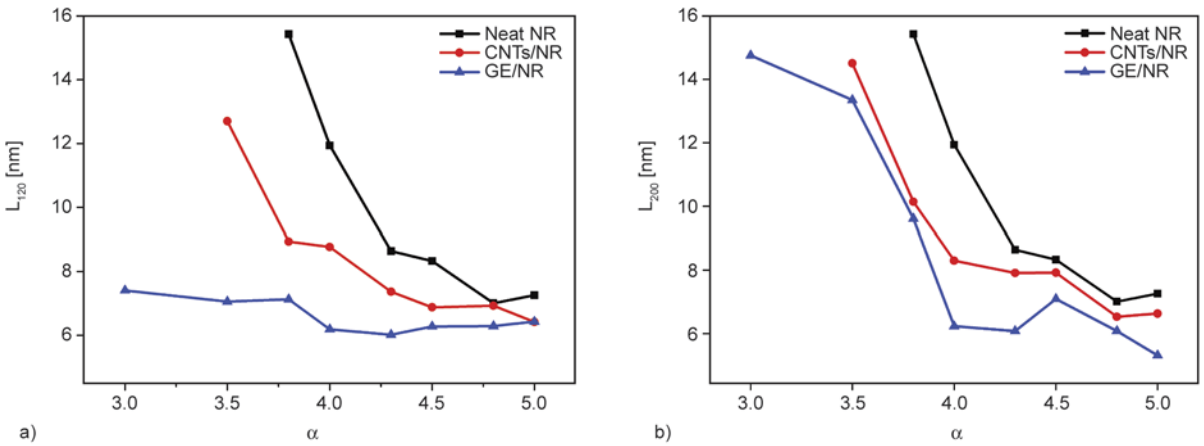

Figure 4. Variation of lateral crystallite size: (a) L_{120} and (b) L_{200} during stretching

has the smallest crystallite size among the three samples, because of the stronger interaction between GE and rubber.

3.4. Entanglement-bound rubber tube (EBT) model

EBT model was used to analyze the rubber network microstructure, to gain insight into the reinforcing effect of GE or CNTs on NR materials on molecular level. In EBT model, the packing effect arising from the inability of molecular chains to pass though their neighborhood imparts topological constraint acting on the entire network chains, and restricts the chains from fluctuating within small length scale. The EBT model allows an appropriate separation of crosslinks and constraint contribution to the stress-strain behavior, and enables the determination of crosslink density.

Based on the EBT model, the elastic free energy w_f that considers the finite extensibility of the chain together with the tube constraint can be expressed by two elastic moduli G_c and G_e, which are closely related to the constants C_1 and C_2 in the Mooney-Rivlin equation [37]. The nominal stress σ is obtained by differentiation $\sigma = \partial w_f/\partial\alpha$ [38]. Based on the model, the constitutive equation of an incompressible sample can be expressed as Equations (8) and (9):

$$\sigma^* = \frac{\sigma}{\alpha - \alpha^{-2}} = G_c + G_e \cdot f(\alpha) \tag{8}$$

$$f(\alpha) = \frac{2(\alpha^{\beta/2} - \alpha^{-\beta})}{\beta(\alpha^2 - \alpha^{-1})}, \quad f(\alpha = 1) = 1 \tag{9}$$

where σ^* is the reduced stress. σ is the nominal stress. α is the extension ratio. G_c is the elastic modulus resulting from the crosslink constraint, and G_e is related to the topological tube-like constraint. β is an empirical constant which describes the relation between the deformed tube in the stretched state and an undeformed tube corresponding to the equilibrium state, β is generally taken as 1 [25]. G_e correlated with the tube lateral dimension within bulk rubber can be calculated by Equation (10):

$$G_e = \frac{v_s l_s^2 k_B T}{4\sqrt{6}\, d_0^2} \tag{10}$$

where v_s is the density of the statistical segments taken as 3.85 nm^{-3} [26], l_s is the average length of Kuhn's statistical segment (0.88 nm for NR). k_B is the Boltzmann constant. The lateral tube dimension (d_0) with a relationship with the mean number of statistical segments between successive entanglements (n_e) is expressed as Equation (11):

$$d_0 = l_s\sqrt{n_e} \tag{11}$$

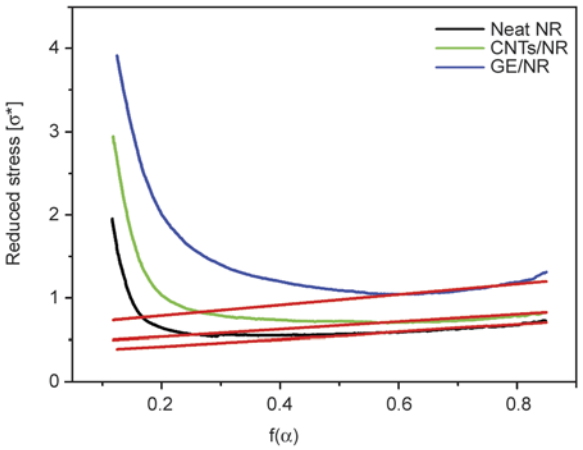

Figure 5. Mooney-Rivlin plots of the unfilled NR and NR composites. The red lines were obtained by linear fitting for the Mooney-Rivlin plots in the region of intermediate deformation

According to the Equation (8) and (9), the stress-strain curves in Figure 1 are converted into the form of a Mooney-Rivlin plot, σ^* vs. $f(\alpha)$, as shown in Figure 5. Considering that EBT model is not fulfilled at large strains on the basis of molecular statistical theory [39], our analysis is limited in the intermediate deformation region. The parameters G_e (related to the topological tube like constraint) and G_c (contributed by the chemical crosslink) in Equation (8) can be determined from the slope and y-axis interception of the linear part of intermediate deformation, as shown in the Mooney plot σ^* vs. $f(\alpha)$ (Figure 5), and the results are shown in Table 4. Given the fact that stress-strain behaviors of NR composite show strong dependence on both chemical crosslink and topological constraints contributions, the initial decrease in stress with increasing strain α can be ascribed to the slippage of entanglement [25]. At high strains, however, Mooney-Rivlin curves exhibit a noticeable upturn related to the rapidly increase of stress, which can be attributed to the strain induced crystallization [40] and the finite extensibility of chains [39]. As shown in Table 4, with the addition of filler, both network parameters G_c and G_e increase. Also it can be noted that the G_c and G_e values for GE/NR composite are higher than those for CNTs/NR composite. As shown in Figure 5, GE/NR composite

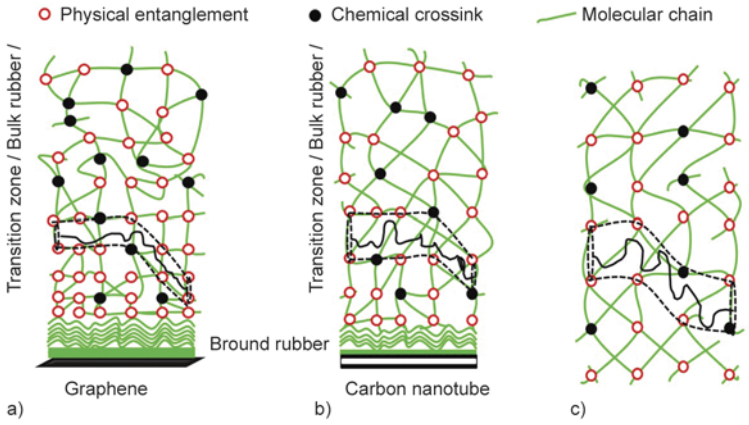

Figure 6. Schematic diagram of the entanglement bound rubber tube model, (a) GE/NR (b) CNTs/NR (c) NR

shows an upturn at a smaller strain than CNTs/NR composites, indicating that GE is more helpful for strain induced crystallization.

The average molecular mass of the network chains (M_c) is related to G_c according to the equation of $M_c = \rho_p RT/G_c$, ρ_p is the polymer density, R is the gas constant. The decrease of M_c with increasing GE content is equal to an increase in the formation of polymer-filler couples and short bridging chains between filler particles which enlarges the extension of the filled network or the highly bounded clusters of filler particles [26]. Because of the stronger interfacial interactions between GE and rubber, GE/NR composites exhibit more increase in the parameters G_c and G_e than CNTs/NR composites. To understand the effect of fillers on the rubber chain network, EBT model is schematically represented in Figure 6.

The EBT model assumed that a number of entanglements, which are believed to dominate the rubber property, are formed in the transition zones between the tightly adsorbed bound and bulk rubbers far from the filler surface phases [25]. The parameters G_c and G_e values shown in Table 4 increased due to the strong interaction between fillers and rubber matrix in the transition zones. With the addition of filler, the tube dimension d_0 decreases, also the mean number of Kuhn's statistic chain segments between two successive entanglements (n_e), as well as the average molecular mass of the chain (M_c) decrease. Our results are similar with those for rubber network filled with clay reported by López-Manchado *et al*. [26].

The well dispersed GE or CNTs nanoparticles with high specific surface area have more chance, compared to the conventional filler with low specific surface, to interact with rubber matrix, and are capable of making majority of rubber confined even at a lower content. TEM and SEM micrographs confirm the homogeneous dispersion of GE or CNTs in NR matrix in our previous report [14, 41]. So, as corroborated by molecular network parameters, the addition of GE or CNT reduces the tube dimensions, by the presence of adjacent chains, which restricts the movement of the rubber chains to a lower range. The chain is nanoscopically confined, forming a highly ordered and entangled structure due to the intense filler-rubber interactions, which limits the lateral fluctuation of the chain to a lower volume and reduces the number of possible chain configuration associated to the chain entropy [26]. In addition, the tube dimension for the GE/NR systems is smaller than that for CNTs/NR. This can be attributed to a more significant contribution of the entanglements in the transition zone due to the stronger filler-rubber interaction in the GE/NR composite. The lower Q_f/Q_g value and higher bound rubber content of GE/NR shown in Table 2, confirm the strong interaction between the GE and NR matrix.

Table 4. Network molecular parameters of unfilled and filled rubbers

	G_c^{*a} [MPa]	G_e^{*b} [MPa]	d_0 [nm]	n_e	M_c
NR	0.34	0.43	1.71	3.76	5389
CNTs/NR	0.44	0.45	1.67	3.59	4164
GE/NR	0.66	0.63	1.41	2.57	2776

It is known that strain induced crystallization of NR results from the entropy drop during stretching, and this allows a thermodynamic description for SIC. The melting temperature (T_m) of NR increases during stretching. When T_m exceeds the room temperature, NR molecular chains are overstrained and get into a supercooled state, and the onset of crystallization take place, as shown in Equation (12) [42]:

$$\frac{1}{T_{m,s}} = \frac{1}{T_{m,0}} + \frac{\Delta S_{def}}{\Delta H} \quad (12)$$

where $T_{m,s}$ is the melting temperature in the stretched state, $T_{m,0}$ the melting temperature in the unstretched state, ΔH the melting enthalpy, and ΔS_{def} the difference of the entropy between the stretched and unstretched states. The onset of SIC of NR composites is dependent on ΔS_{def}, which is a function of strain.

The entropy change of the filled rubber is consisted of two parts: (1) the entropy reduction caused by the addition of filler (ΔS_f), which was attributed to the interactions between rubber chains and the filler; (2) deformation entropy (ΔS_{def}) during stretching, as shown in Figure 7. ΔS_f of CNTs/NR and GE/NR composites are expressed as ΔS_1 and ΔS_3, respectively. ΔS_{def} of CNTs/NR and GE/NR composites are expressed as ΔS_2 and ΔS_4, respectively. On the assumption that the total entropy change required for the onset of SIC in the filled and unfilled rubber is the same, i.e. $\Delta S_0 \approx \Delta S_1 + \Delta S_2 \approx \Delta S_3 + \Delta S_4$, as ΔS_f of GE/NR composites is higher than that of CNTs/NR, *i.e.* $\Delta S_3 > \Delta S_1$ due to a more ordered structure for GE/NR composites, ΔSdef of GE/NR composites should be lower than that of CNTs/NR, i.e. $\Delta S_4 < \Delta S_2$, which means the onset of strain-induced crystallization of GE/NR composites appeared at a lower strain.

4. Conclusions

Natural rubber composites containing two kinds of fillers, CNTs and graphene were prepared by an ultrasonically-assisted latex mixing process. A significant improvement in tensile strength was achieved for both graphene and CNTs filled NR, while graphene has a better reinforcing effect. The role of CNTs and graphene on strain-induced crystallization of NR was investigated by means of synchrotron WAXD. The addition of graphene in NR results in faster strain-induced crystallization rate and a higher crystallinity compared to CNTs, which contributes to a better reinforcing effect. The NR molecular network parameters of graphene/NR and CNTs/NR composites were determined by applying the EBT model in combination with Mooney-Rivlin plots. Due to the larger specific surface area, Graphene has more chance to interact with rubber than CNTs, resulting in the decreased tube dimension, and sequentially the reduction of configurational entropy of rubber molecular chains. Graphene/NR composites have lower deformation entropy during stretching than CNTs/NR composites.

Acknowledgements

This work is supported by National Natural Science Foundation of China (NNSFC 51433006) and the major project of Chinese Ministry of Education (313036). Professor Liangbin Li of National Synchrotron Radiation Laboratory (NSRL) in University of Science and Technology of China are also greatly appreciated for the help in Synchrotron WAXD experiments.

References

[1] Toki S., Sics I., Ran S., Liu L., Hsiao B. S., Murakami S., Senoo K., Kohjiya S.: New insights into structural development in natural rubber during uniaxial deformation by *in-situ* synchrotron X-ray diffraction. Macromolecules, **35**, 6578–6584 (2002). DOI: 10.1021/ma0205921

[2] Trabelsi S., Albouy P-A., Rault J.: Stress-induced crystallization around a crack tip in natural rubber. Macromolecules, **35**, 10054–10061 (2002). DOI: 10.1021/ma021106c

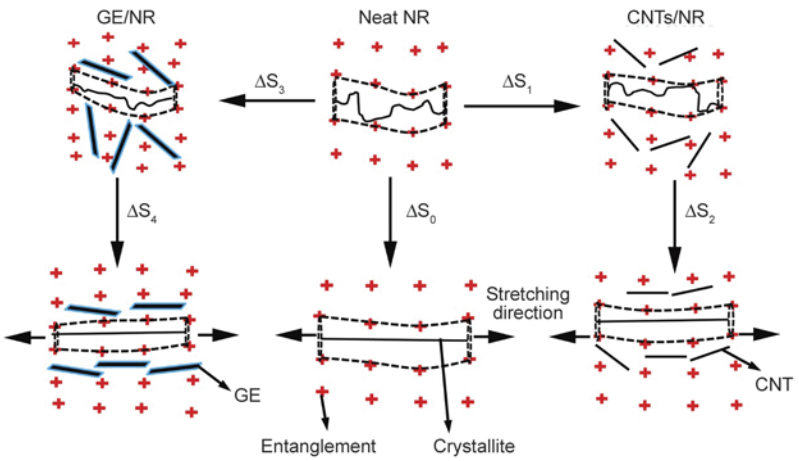

Figure 7. Schematic representation of structural evolution and entropy change of filled and unfilled rubber during stretching

[3] Toki S., Hsiao B. S.: Nature of strain-induced structures in natural and synthetic rubbers under stretching. Macromolecules, **36**, 5915–5917 (2003).
DOI: 10.1021/ma034729e

[4] Ikeda Y., Yasuda Y., Hijikata K., Tosaka M., Kohjiya S.: Comparative study on strain-induced crystallization behavior of peroxide cross-linked and sulfur cross-linked natural rubber. Macromolecules, **41**, 5876–5884 (2008).
DOI: 10.1021/ma800144u

[5] Sun X., Sun H., Li H., Peng H.: Developing polymer composite materials: Carbon nanotubes or graphene? Advanced Materials, **25**, 5153–5176 (2013).
DOI: 10.1002/adma.201301926

[6] Kim H., Abdala A. A., Macosko C. W.: Graphene/polymer nanocomposites. Macromolecules, **43**, 6515–6530 (2010).
DOI: 10.1021/ma100572e

[7] Treacy M. M. J., Ebbesen T. W., Gibson J. M.: Exceptionally high Young's modulus observed for individual carbon nanotubes. Nature, **381**, 678–680 (1996).
DOI: 10.1038/381678a0

[8] Lee C., Wei X., Kysar J. W., Hone J.: Measurement of the elastic properties and intrinsic strength of monolayer graphene. Science, **321**, 385–388 (2008).
DOI: 10.1126/science.1157996

[9] Berber S., Kwon Y-K., Tománek D.: Unusually high thermal conductivity of carbon nanotubes. Physical Review Letters, **84**, 4613–4616 (2000).
DOI: 10.1103/PhysRevLett.84.4613

[10] Balandin A. A., Ghosh S., Bao W., Calizo I., Teweldebrhan D., Miao F., Lau C. N.: Superior thermal conductivity of single-layer graphene. Nano Letters, **8**, 902–907 (2008).
DOI: 10.1021/nl0731872

[11] Ebbesen T. W., Lezec H. J., Hiura H., Bennett J. W., Ghaemi H. F., Thio T.: Electrical conductivity of individual carbon nanotubes. Nature, **382**, 54–56 (1996).
DOI: 10.1038/382054a0

[12] Geim A. K., Novoselov K. S.: The rise of graphene. Nature Materials, **6**, 183–191 (2007).
DOI: 10.1038/nmat1849

[13] Yan N., Xia H., Zhan Y., Fei G.: New insights into fatigue crack growth in graphene-filled natural rubber composites by microfocus hard-X-ray beamline radiation. Macromolecular Materials and Engineering, **298**, 38–44 (2013).
DOI: 10.1002/mame.201200044

[14] Zhan Y., Wu J., Xia H., Yan N., Fei G., Yuan G.: Dispersion and exfoliation of graphene in rubber by an ultrasonically-assisted latex mixing and *in-situ* reduction process. Macromolecular Materials and Engineering, **296**, 590–602 (2011).
DOI: 10.1002/mame.201000358

[15] Zhan Y., Lavorgna M., Buonocore G., Xia H.: Enhancing electrical conductivity of rubber composites by constructing interconnected network of self-assembled graphene with latex mixing. Journal of Materials Chemistry, **22**, 10464–10468 (2012).
DOI: 10.1039/C2JM31293J

[16] Joly S., Garnaud G., Ollitrault R., Bokobza L., Mark J. E.: Organically modified layered silicates as reinforcing fillers for natural rubber. Chemistry of Materials, **14**, 4202–4208 (2002).
DOI: 10.1021/cm020093e

[17] Carretero-Gonzalez J., Verdejo R., Toki S., Hsiao B. S., Giannelis E. P., López-Manchado M. A.: Real-time crystallization of organoclay nanoparticle filled natural rubber under stretching. Macromolecules, **41**, 2295–2298 (2008).
DOI: 10.1021/ma7028506

[18] Li F., Yan N., Zhan Y., Fei G., Xia H.: Probing the reinforcing mechanism of graphene and graphene oxide in natural rubber. Journal of Applied Polymer Science, **129**, 2342–2351 (2013).
DOI: 10.1002/app.38958

[19] Song H. H., Kang M. K., Jeon H-J., Kwag G., Choi H.: Strain-induced crystallization and mechanical properties of carbon nanotubes reinforced natural rubber. in 'Technical Proceedings of the 2007 NSTI Nanotechnology Conference and Trade Show, Santa Clara, California' Vol 2, 164–165 (2007).

[20] Ozbas B., Toki S., Hsiao B. S., Chu B., Register R. A., Aksay I. A., Prud'homme R. K., Adamson D. H.: Strain-induced crystallization and mechanical properties of functionalized graphene sheet-filled natural rubber. Journal of Polymer Science Part B: Polymer Physics, **50**, 718–723 (2012).
DOI: 10.1002/polb.23060

[21] Edwards S. F.: The statistical mechanics of polymers with excluded volume. Proceedings of the Physical Society, **85**, 613–624 (1965).
DOI: 10.1088/0370-1328/85/4/301

[22] Edwards S. F.: The statistical mechanics of polymerized material. Proceedings of the Physical Society, **92**, 9–16 (1967).
DOI: 10.1088/0370-1328/92/1/303

[23] Leblanc J.: Insight into elastomer-filler interactions and their role in the processing behaviour of rubber compounds. Progress in Rubber and Plastics Technology, **10**, 112–129 (1994).

[24] Funt J. M.: Dynamic testing and reinforcement of rubber. Rubber Chemistry and Technology, **61**, 842–865 (1988).
DOI: 10.5254/1.3536222

[25] Heinrich G., Vilgis T. A.: Contribution of entanglements to the mechanical properties of carbon black-filled polymer networks. Macromolecules, **26**, 1109–1119 (1993).
DOI: 10.1021/ma00057a035

[26] López-Manchado M. A., Valentín J. L., Carretero J., Barroso F., Arroyo M.: Rubber network in elastomer nanocomposites. European Polymer Journal, **43**, 4143–4150 (2007).
DOI: 10.1016/j.eurpolymj.2007.07.023

[27] Hummers W. S., Offeman R. E.: Preparation of graphitic oxide. Journal of the American Chemical Society, **80**, 1339 (1958).
DOI: 10.1021/ja01539a017

[28] Lorenz O., Parks C. R.: The crosslinking efficiency of some vulcanizing agents in natural rubber. Journal of Polymer Science, **50**, 299–312 (1961).
DOI: 10.1002/pol.1961.1205015404

[29] Ismail H., Nasaruddin M. N., Ishiaku U. S.: White rice husk ash filled natural rubber compounds: The effect of multifunctional additive and silane coupling agents. Polymer Testing, **18**, 287–298 (1999).
DOI: 10.1016/S0142-9418(98)00030-0

[30] Leblanc J., Hardy P.: Evolution of bound rubber during the storage of uncured compounds. Kautschuk und Gummi, Kunststoffe, **44**, 1119–1124 (1991).

[31] Treloar L. R. G.: The physics of rubber elasticity. Oxford University Press, Oxford (1975).

[32] Wu J., Schultz J. M., Yeh F., Hsiao B. S., Chu B.: *In-situ* simultaneous synchrotron small- and wide-angle X-ray scattering measurement of poly(vinylidene fluoride) fibers under deformation. Macromolecules, **33**, 1765–1777 (2000).
DOI: 10.1021/ma990896w

[33] Poompradub S., Tosaka M., Kohjiya S., Ikeda Y., Toki S., Sics I., Hsiao B. S.: Mechanism of strain-induced crystallization in filled and unfilled natural rubber vulcanizates. Journal of Applied Physics, **97**, 103529/1–103529/9 (2005).
DOI: 10.1063/1.1900927

[34] Rault J., Marchal J., Judeinstein P., Albouy P. A.: Stress-induced crystallization and reinforcement in filled natural rubbers: ^{2}H NMR study. Macromolecules, **39**, 8356–8368 (2006).
DOI: 10.1021/ma0608424

[35] Tosaka M., Murakami S., Poompradub S., Kohjiya S., Ikeda Y., Toki S., Sics I., Hsiao B. S.: Orientation and crystallization of natural rubber network as revealed by WAXD using synchrotron radiation. Macromolecules, **37**, 3299–3309 (2004).
DOI: 10.1021/ma0355608

[36] Klug H. P., Alexander L. E.: X-ray diffraction procedures: For polycrystalline and amorphous materials. Wiley, New York (1974).

[37] Klüppel M., Schramm J.: A generalized tube model of rubber elasticity and stress softening of filler reinforced elastomer systems. Macromolecular Theory and Simulations, **9**, 742–754 (2000).
DOI: 10.1002/1521-3919(20001201)9:9<742::AID-MATS742>3.0.CO;2-4

[38] Edwards S. F.: The theory of rubber elasticity. British Polymer Journal, **9**, 140–143 (1977).
DOI: 10.1002/pi.4980090209

[39] Wang M. C., Guth E.: Statistical theory of networks of non-Gaussian flexible chains. The Journal of Chemical Physics, **20**, 1144–1157 (1952).
DOI: 10.1063/1.1700682

[40] Flory P. J.: Effects of molecular structure on physical properties of butyl rubber. Industrial and Engineering Chemistry, **38**, 417–436 (1946).
DOI: 10.1021/ie50436a023

[41] Zhan Y. H., Liu G. Q., Xia H. S., Yan N.: Natural rubber/carbon black/carbon nanotubes composites prepared through ultrasonic assisted latex mixing process. Plastics, Rubber and Composites, **40**, 32–39 (2011).
DOI: 10.1179/174328911X12940139029284

[42] Tosaka M.: A route for the thermodynamic description of strain-induced crystallization in sulfur-cured natural rubber. Macromolecules, **42**, 6166–6174 (2009).
DOI: 10.1021/ma900954c

eXPRESS Polymer Letters Vol.9, No.7 (2015) 608–623
Available online at www.expresspolymlett.com
DOI: 10.3144/expresspolymlett.2015.57

Targeted kinetic strategy for improving the thermal conductivity of epoxy composite containing percolating multi-layer graphene oxide chains

T. Zhou[1], H. Koga[2], M. Nogi[2], T. Sugahara[2], S. Nagao[2], T. T. Nge[2], K. Suganuma[2], H-W. Cui[2], F. Liu[1], Y. Nishina[3]*

[1]School of Materials Science and Engineering, Nanjing University of Science and Technology, 210094 Nanjing, China
[2]The Institute of Scientific and Industrial Research, Osaka University, Mihogaoka 8-1, Ibaraki, 567-0047 Osaka, Japan
[3]Research Core for Interdisciplinary Science, Okayama University, Tsushimanaka, Kita-ku, 700-8530 Okayama, Japan

Received 27 November 2014; accepted in revised form 26 January 2015

Abstract. By adding 2 wt% multi-layer graphene oxide (MGO) to an epoxy resin, the thermal conductivity of the composite reached a maximum, 2.03 times that of the epoxy. The presence of 2 wt%MGO percolating chains leads to an unprecedentedly sharp rise in energy barrier at final curing stage, but an increased epoxy curing degree (α_{IR}) is observed; however, this α_{IR} difference nearly disappears after aging or thermal annealing. These results suggest that the steep concentration gradient of –OH, originated from the 2 wt%MGO percolating chains, exerts the vital driving force on the residual isolated/trapped epoxy to conquer barrier for epoxy-MGO reaction. A modified Shrinking Core Model customized for the special layered-structure of MGO sheet was proposed to understand the resistance variation during the intercalative epoxy-MGO reaction. It shows that the promoted intercalative crosslinking is highly desirable for further improving the thermal conductivity of the composite, but it meets with increased resistance. Guided by the kinetic studies, targeted optimization on the cure processing strategy was accordingly proposed to promote the intercalative crosslinking, a thermal conductivity, 2.96 times that of the epoxy, was got with only a small amount (30°C) increase of the post-heating temperature.

Keywords: *polymer composites, nanocomposites, thermal properties, graphene oxide*

1. Introduction

The thermal conductivity of materials are becoming increasingly important in tandem with the need for more efficient heat removal in numerous advanced systems such as printed electronics [1], automotive and aerospace products [2]. Due to the fascinating and especially, technologically useful properties, worldwide, an enormous amount of research effort goes into the utilization of graphene materials (GMs), particularly in strengthening polymers. Strategies involving GM content, exfoliation and dispersion state of GM, GM/polymer interfacial interaction, etc. have been taken into account; however, the property improvements are still far from expectations and the thermal conductivity in particular [3–5]. The polymerization of monomers into the polymer matrix is of vital importance to the final properties of composites, several kinetic works reported the effect of GMs on the polymerization [6–11], specifically, Wu *et al*. [6] found a vulcanization stage dependence of activation energy (E) variation of graphene/natural rubber system with Ozawa and Kissinger methods; Wang and Qiu [7] noticed an accelerated isothermal melt crystallization of poly (l-lactic acid) by graphene oxide (GO) with isoconversional method; Jing and Qiu [8] used Avrami

*Corresponding author, e-mail: ztltianle999@hotmail.com

equation and revealed that the isothermal melt crystallization rate of poly(3-hydroxybutyrate) depends on the GO loading and the crystallization temperature; Zhang *et al*. [9] used Kissinger equation and noticed that GO decreases the *E* of nylon 6; Qiu *et al*. [10] used isoconversional method and found that the effect of GO on the *E* of a tetrafunctional tetraglycidyl-4,4′-diaminodiphenylmethane cured with 4,4′-diaminodiphenylsulfone depends on GO content and curing stage; and with Kamal and Ryan's model as well as Isayev and Deng's model, Allahbakhsh *et al*. [11] revealed that *E* of GO/ethylene-propylene-diene rubber system depends on the GO content and the dispersion quality of GO. Notably, hardly any kinetic works directly contribute to the performance improvement of GM/polymer composites, worse still, the polymerizing strategy for the polymer matrices are extensively misused for the GM/polymer composites.

MGO based composites can be produced via *in-situ* intercalative polymerization [12]. Successful polymerizations of epoxy, polyaniline, polypyrrole, acrylic, poly(vinyl alcohol), poly(methyl methacrylate) and poly(arylene disulfide) with MGO have been reported [13–18]. However, most of these studies did not pay attention to the resistance variation of the progressive intercalation process.

In this study, the effect of multi-layer GO (MGO) percolating chains on the curing kinetics of diglycidyl ether of bisphenol-A (DGEBA)/2-ethyl-4-methylimidazole (EMI-2,4) system (a widely used epoxy system in industries) was studied. Formation mechanism of the MGO/epoxy percolating network was explored, for the first time based on the real-time *E* variation. A modified Shrinking Core Model customized for the special layered-structure of MGO sheet was proposed to understand the resistance variation during the intercalative epoxy-MGO reaction. The main aim is to effectively improve the thermal conductivity of epoxy composite containing percolating MGO chains by targeted kinetic strategy.

2. Experimental

2.1. Materials

So far, GO has been extensively utilized in polymer composites. Besides the lower cost and higher yield production than graphene, GO is heavily oxygenated (its basal plane carbon atoms are decorated with –OH and C–O–C groups, while –OH and –COOH groups at the edge), not only enabling an improved GO/polymer interfacial interaction and better dispersion state of GO in matrix, but also reducing the interplanar forces and increasing the inter-layer spacing, beneficial to *in-situ* intercalative polymerization [3–5]. Furthermore, monolayer or few-layer GO not necessarily gives the best reinforcement since too much amount of wrinkling of GO weakens its effectiveness for forming conductive network, therefore, MGO is more desirable in this work. MGO/water mixture (Rap GO TQ2, low oxidation grade) was supplied by NiSiNa materials Co., Ltd, Japan. Before being used, MGO/water mixture was moderately centrifugated (10 000 rpm, 10 min) with abundant ethanol for 3 times to replace water solvent with ethanol solvent as well as removing any agglomerated MGO.

Epoxy resin employed was a nominally difunctional epoxy resin, i.e. Epon 828 (DGEBA with epoxy value of 0.48–0.52 mol/100 g, supplied by Shanghai Resin Co. Ltd., China). Curing agent EMI-2,4 was supplied by Wako Pure Chemical Industries, Ltd., Japan. The employed ratio of DGEBA and EMI-2,4 was 100:6. Graphite particles (sized at 500 μm, carbon content >99%) were supplied by Xinfangyuan Co. Ltd., China. Other agents were analytically pure grade and supplied by Wako Pure Chemical Industries, Ltd., Japan.

2.2. Preparation of MGO/DGEBA/EMI-2,4 mixture

MGO/ethanol mixture was sonicated for 1.5 h in advance to break down agglomerates. A certain amount of MGO/ethanol mixture was mixed with epoxy precursor (DGEBA) and EMI-2,4, then the mixture was stirred with a rotation speed of 2000 rpm as well as a simultaneous revolution speed of 2000 rpm for 6 times (each time for 5 min) by using Thinky Mixer (ARV310, Thinky Co. Japan), a vacuum pressure reduction function of which removed solvents and submicron air bubbles as well as giving an outstanding dispersion performance (This step is unique in comparison with other methods for nanocarbon-based composite preparation, not only because most of solvent can be removed during the mixing process, but also because excellent dispersion of nanocarbon fillers is guaranteed as the solvent reduces). Each time after mixing for 5 min, an ice bath was utilized to keep the temperature of mixture around 283 K (low-temperature treatment produces better nanofiller dispersion state than high-

temperature treatment [19] as well as preventing from an untimely occurrence of curing), then the mixture was weighted to determine the precise amount of MGO introduced into matrix and the amount of MGO/water mixture needed to add. Repeating this process until the MGO content was 0.5, 1, 2, 2.2, 2.5 or 3% by weight of epoxy resin.

2.3. Preparation of MGO/epoxy composite

MGO/epoxy composite was prepared by *in-situ* polymerization. Although Thinky Mixer uses sophisticated approaches in removing solvents during mixing and thus reducing the defects of voids and pores in the final composite, it is necessary to degass the mixture after the casting step to remove the air absorbed during this step. Basic preparation process involved (a) casting the mixture in mould, (b) repeatedly degassing the mixture in vacuum drying oven at 313 K until no air bubble appears on the surface of the mixture, (c) curing the mixture at 313 K for 1 h, 378 K for 1.5 h, and 458 K for 1.5 h (improved cure processing strategies were listed in the Results and discussion part), and (d) cooling to room temperature, then demoulding.

2.4. Characterization

Morphological studies were carried out using transmission electron microscopy (TEM, JEM-3000F, JEOL Japan Co., Ltd.) and field emission scanning electron microscopy (FE-SEM, JSM-6700F, JEOL Japan Co., Ltd.). Specimens were coated with a thin platinum layer before FE-SEM observation.

Infrared spectra were tested using a FTIR spectrometer (Perkin-Elmer frontier, Perkin-Elmer Japan Co., Ltd.) for evaluating the functional groups of MGO as well as the epoxy curing degree (α_{IR}) of cured samples. FTIR spectra were obtained by an accumulation of 16 scans in a range of frequency from 4000 to 700 cm^{-1} with a resolution of 4 cm^{-1}. Attenuated total reflectance spectra were collected from the polymeric films. A set of three specimens was tested for each material after pre-dried in air at 373 K for 12 h.

Wide-angle X-ray diffractometry (WXRD) (Rigaku RINT RAPID II, 40 kV, 20 mA) with CuKa radiation (X-ray wavelength k = 0.154 nm) was used to examine the crystal structure of the samples. The range of diffraction angles (2θ) was 0~50°. A set of three specimens was tested for each material.

Approximately 4 mg MGO/DGEBA/EMI-2,4 mixture was weighed accurately into an aluminum differential scanning calorimetry (DSC) sample pan and then covered with an aluminum lid. DSC measurements were carried out by using a NETZSCH DSC 204 F1 system (NETZSCH Instruments Japan Co., Ltd.). The DSC was calibrated with high purity indium; a-Al_2O_3 was used as the reference material. Dynamic experiments were carried out under an argon flow rate of 25 mL/min and a temperature ranging from 313 to 623 K at different heating rates of 10, 15, 20, 25 K/min. The reaction was considered to be complete when the rate curve leveled off to a baseline. The cured sample was left in the DSC cell and cooled to the room temperature. Then the cured samples were tested by FITR and α_{IR} was obtained by measuring the reactive absorbance of the epoxy band (914 cm^{-1}) against the absorbance of the band associated with the benzene ring (1610 cm^{-1}) which acts as a reference in spectra. These absorbances were calculated in the spectra processed by a baseline correction to obtain comparable results. To determine the glass transition temperature (T_g) of reacted product, the cured sample was scanned again by DSC to 623 K at 10 K/min. The intermediate point of the heat flow step of the second diagram was defined as DSC T_g. A set of three specimens was tested for each material.

Thermal diffusivity (δ, mm^2/s) at room temperature was measured on square plate samples (10×10×1 mm^3) by laser flash method (nanoflash LFA 447 system, NETZSCH Instruments Japan Co., Ltd, a total of 5 shots were taken per sample set), specific heat (C, J/gK) at room temperature was measured on disk samples (6 mm diameter, 1 mm thickness) by DSC (NETZSCH DSC 204 F1 system, NETZSCH Instruments Japan Co., Ltd.), and bulk density (ρ, g/cm^3) of specimen was measured by water displacement. For each measurement, three samples were tested five times. After that, thermal conductivity (λ, W/mK) was calculated by Equation (1):

$$\lambda = \delta \cdot C \cdot \rho \quad (1)$$

Coefficient of thermal expansion (CTE) was tested on square plate samples (25×5×1 mm3) by SII TMA/SS7100 (Hitachi High-Tech Science Co., Japan, tensile mode with a 5 mN load) at a heating rate of 5 K/min in N_2 atmosphere. The CTE values were

determined from the second run of 303~443 K profiles. A set of three specimens was tested for each material.

Thermal degradation behavior was characterized by TGA (TG-DTA200se/h/24/1 system, NETZSCH Instruments Japan Co., Ltd.) at a scan rate of 10 K/min to 1023 K in N_2. A set of three specimens was tested for each material. Specimens were predried in air at 373 K for 12 h to remove absorbed water.

3. Results and discussion

3.1. Morphology and characterization of MGO

Morphology and characterization of MGO greatly determine its contribution to the performance improvement of composites. Typical TEM image of a MGO sheet (Figure 1a) exhibits a crumpled paper-like morphology, core section of the sheet (see the inset in Figure 1a) presents 8.4 nm in thickness, implying that many MGO sheets utilized in this work are composed of ~17 stacked single-layer sheets since the average thickness of individually exfoliated GO sheet is ~0.486 nm [20]. Selected-area electron diffraction (SED) of those stacks (Figure 1b) displays weak and diffuse rings, suggesting the loss of long-range ordering, though it is not as perfect as pristine graphene, however, blurry hexagonal symmetry of graphene was maintained. Also, parallel dark fringes are noted in the inset in Figure 1a and the spacing between neighboring fringes is ~0.34 nm, consistent with the spacing between (002) planes of graphite.

Dimensions of MGO sheets, as shown in the FE-SEM image (Figure 1c), are from submicron to several micrometers and a relatively large sheet is about 12×20 μm^2. The sheet surface exhibits a bumpy tex-

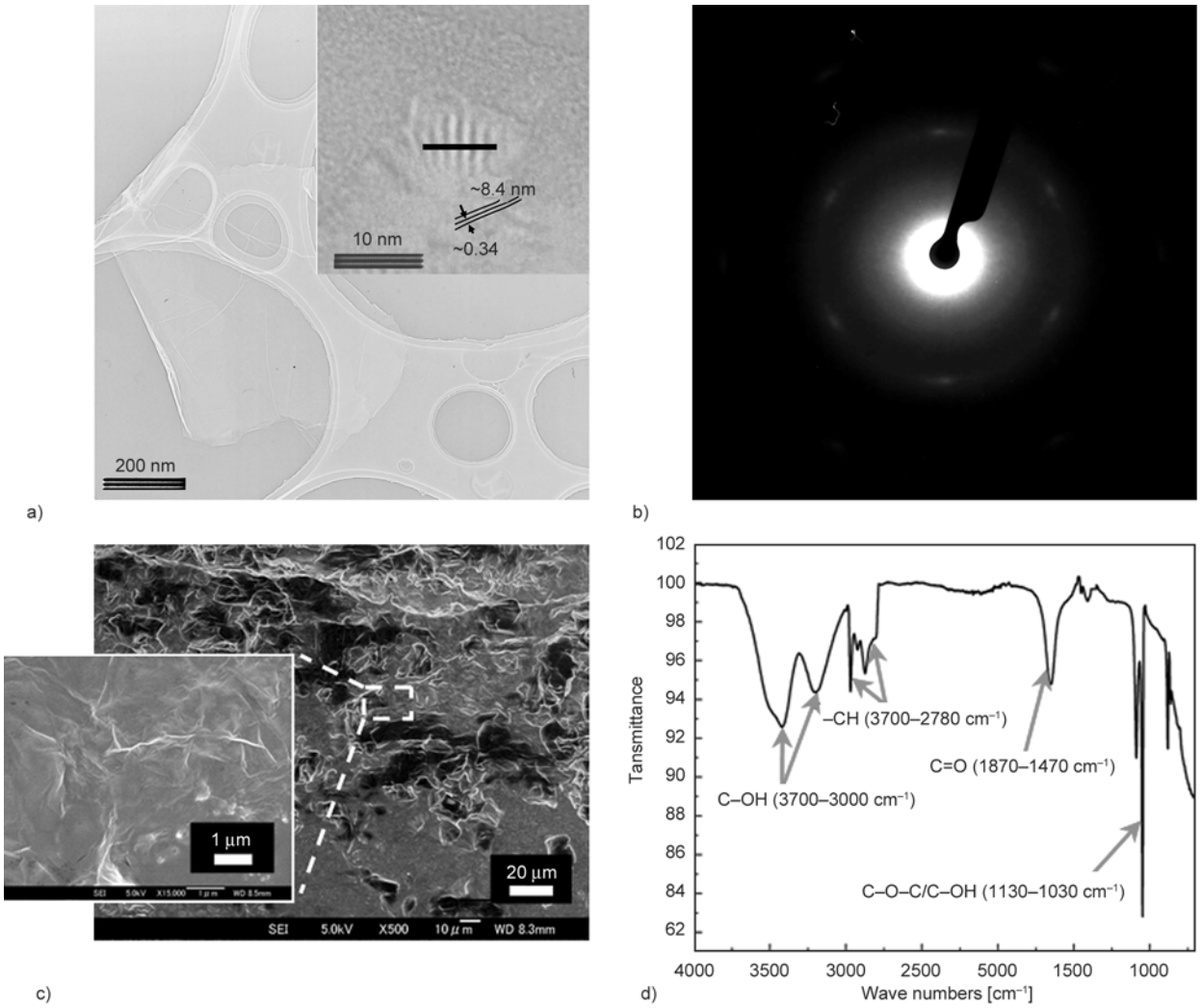

Figure 1. (a) Typical TEM image of a MGO sheet (inset: cross-section) and (b) its SED pattern; (c) FE-SEM images (inset: enlargement of the boxed region) and (d) FTIR spectrum (insets: explanatory notes for functional groups) of MGO sheets

ture where many corrugations with several hundred nanometers are discernible (see the insert in Figure 1c). Besides the extremely small thickness, isolated oxygen reaction sites contribute to the wrinkled topology of MGO sheets at nanoscale [21] since the most characteristic feature in FTIR spectrum (Figure 1d) is the broad, intense band of –OH (3700–3000 cm^{-1}) as well as other bands associated with C–O functionalities (i.e. C=O and C–O–C/C–OH) [11, 15].

3.2. Improving the thermal conductivity of epoxy by using MGO

Firstly, strategies involving MGO content, exfoliation and dispersion state of MGO, and MGO/epoxy interfacial interaction were taken into account as follows:

As shown in Figure 2, the thermal conductivity of MGO/epoxy composites increases with the increasing MGO content (0.5, 1, 2 wt%), 2 wt% MGO surpassed percolation threshold (falls within 1~2 wt%) and gave a maximum thermal conductivity, 2.03 times that of the epoxy. These results are comparable with the values reported in [22–25]. Further improving the thermal conductivity by increasing MGO content (> 2 wt%) is impossible to realize since a dramatically increased viscosity had already been noticed as preparing the 2 wt% MGO/epoxy composite with big agglomerates and trapped air bubbles impossible to be cleared in the case of higher MGO loading (see the agglomerates and through-holes emerging in the insets).

The level of exfoliation and dispersion of MGO play crucial roles in determining the ultimate performance of composites since restacking of MGO sheets significantly reduces their effectiveness for forming conductive network [21, 26].

XRD is an important tool for analyzing the exfoliation level of MGO in composites [26]. As shown in Figure 3a, WXRD pattern of graphite particles exhibits a sharp characteristic peak centered at 2θ = 26.6° and a small one centered at 2θ = 43.3°, which are assigned to the diffraction of (002) and (100) planes of well-ordered graphenes, respectively [27]. The as-received MGO product keeps the small one and the sharp characteristic peak disappears, which is associated with a high disorder in the direction perpendicular to MGO layers [27]. (The sharp peak at 2θ = 26.6° in graphite usually shifts to 14.1–14.9° in graphite oxide, however, the peak would disappear as

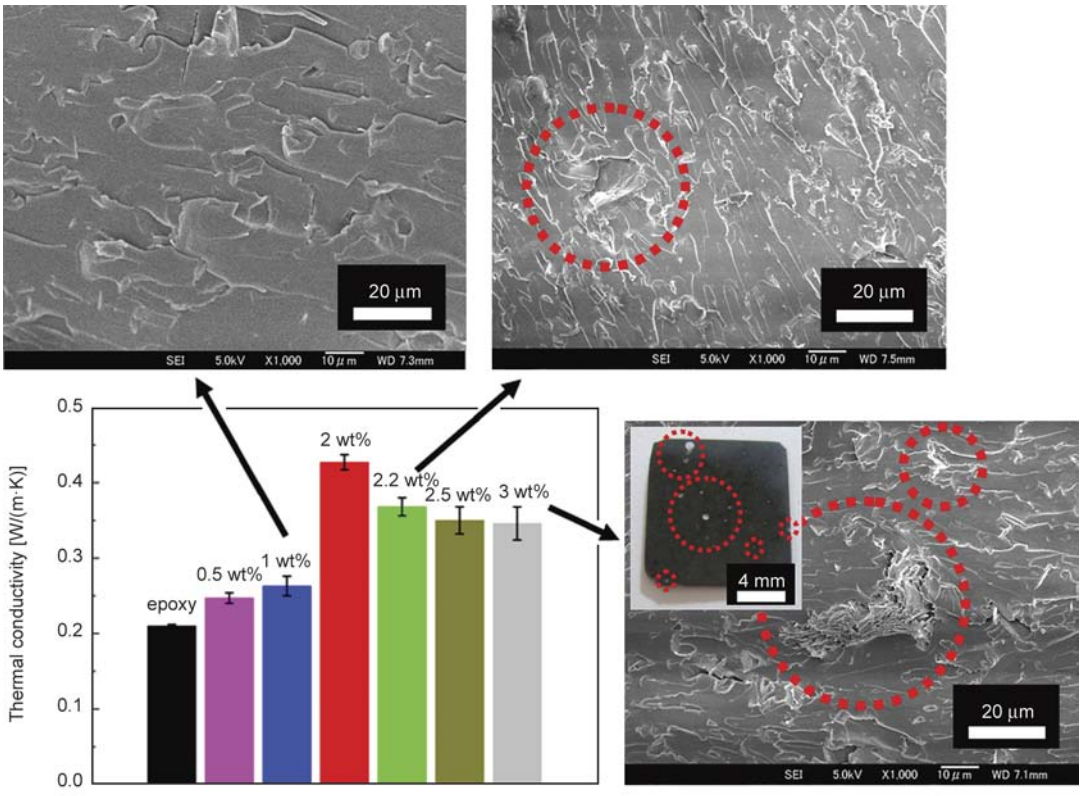

Figure 2. Thermal conductivities of MGO/epoxy composites; insets: FE-SEM images of the fracture surface of 1, 2.2, 3 wt% MGO/epoxy composites and photograph of 3 wt% MGO/epoxy composite, circles show MGO agglomerates or through-holes

graphite oxide exfoliates into singer sheets [18]. The small peak centered at $2\theta = 43.3°$ usually remains in graphite oxide [27] or MGO sheets [17]). Notably, after dispersed in matrix, WXRD patterns of all the studied MGO/epoxy composites except 3 wt% MGO loading only show a broad diffraction peak derived form the amorphous epoxy (centered at $2\theta = 18.5°$); the small peak disappears, which indicates a complete disorder in the direction perpendicular to GO layers, corresponding to an exfoliation of MGO by intercalation in epoxy matrix [18, 26–28]. Subsequently, the small diffraction peak of MGO appears (see the red circle), verifying that MGO restacks or is partially exfoliated in epoxy matrix at the 3 wt% loading.

The dispersion level of GO can be analyzed in the SEM observation [20, 21]. As MGO loading is low, only a few scattered waves are observed on the fracture surface of 1 wt% MGO composite (see Figure 2). For high GO loading, in the case of poorly-dispersed GO, the fracture surface exhibits relatively rough with some river-like structures, whereas epoxy with highly-dispersed GO presents a rougher fracture surface [20, 21]. As compared with the FE-SEM images in Figure 2 for 2.2, 3 wt% MGO loadings, it can be observed that a rougher fracture surface exhibits in the FE-SEM image of Figure 3b, numerous tortuous and fine river-like structures with hackles and ribbons exist on the fracture surface, indicating that 2 wt% MGO were highly dispersed in the epoxy matrix (the white square in Figure 3c is magnified to verify the existence of individual MGO sheet). In summary, WXRD and FE-SEM results demonstrate that the mixing method utilized in this work

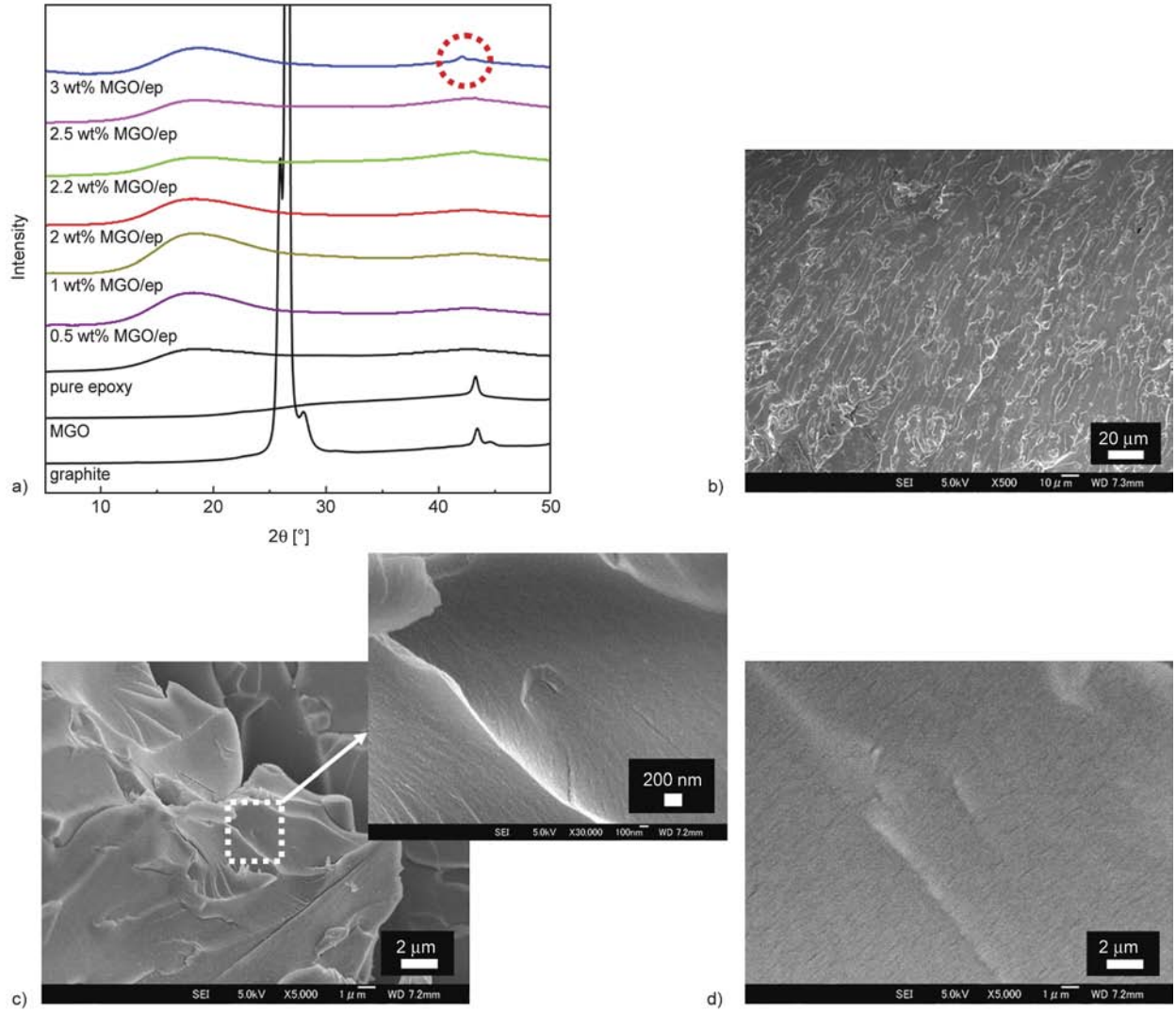

Figure 3. WXRD patterns of graphite, MGO, pure epoxy, and MGO/epoxy composites (circle shows a small peak); FE-SEM images of the fracture surface of (b–c) 2 wt% MGO/epoxy composite (inset: enlargement of the boxed region) and (d) pure epoxy

was effective in exfoliating and dispersing the 2 wt% MGO, and no significant restacking of MGO occurred. MGO agglomerates, through-holes, and restacking/partial exfoliation of MGO are verified to be responsible for the less enhancements in thermal conductivity with higher MGO loading (>2 wt%).

It is rational to expect an ideal MGO/DGEBA interfacial interaction since the interface in GO/polymer composites was reported to be strengthened by grafting DGEBA molecules onto GO sheets [20, 29]. Pure epoxy is featureless as the smooth area in Figure 3d with a typical brittle fracture process, improved surface roughness in Figure 3c is accompanied by a plastic deformation of epoxy matrix with an increased resistance to the deformation, demonstrating a strong bonded MGO/epoxy interface in the 2 wt% MGO/epoxy composite. Considering the negative effects of surfactants e.g. is detrimental to the inherent conductive properties of fillers [30], in this work, surface treatment of MGO using surfactants was believed unnecessary.

Overall, with these strategies 2 wt% MGO surpassed percolation threshold (falls within 1~2 wt%) and achieved a maximum thermal conductivity enhancement of epoxy (2.03 times that of the epoxy). Then, one issue emerged, i.e. how to further improve the thermal conductivity of the epoxy containing MGO percolating chains.

3.3. Exploring the formation mechanism of the 2 wt% MGO/epoxy percolating network based on the real-time $E(\alpha)$

2 wt% MGO/epoxy percolating network dominates the properties of final product; its formation process was monitored using dynamic DSC. In dynamic DSC curve, the total area S of the exothermal peak (region between the exotherm and the baseline) is in direct proportion to the specific total heat ΔH [J/g] released during the reaction.

3.3.1. Reaction mechanism of the 2 wt% MGO/DGEBA/6 wt% EMI-2,4 system

Curing mechanism of DGEBA/EMI-2,4 system (see Figure 4a) involves: (a) sequential two-step reactions (the completion of adduct reactions (I–II) is necessary prior to the etherification reaction (III)), (b) adduct products A2 act as the catalyst initiating the following etherification reaction and thus the origins of crosslinking, and (c) etherification reaction determines the final performance of cured product because epoxy molecules cross-link into the global network during this reaction stage, and it is autocatalytic since A2 is continually regenerated during the reaction [31].

In this study, low EMI-2,4 content, 6% by weight of DGEBA, was utilized to suppress the adduct reactions but with the generated A2 enough for initiating the etherification reaction [31], as a result, etherification reaction dominates the reaction with only one main peak appearing in each curve in Figure 5a, the heat derived from the adduct reactions (including the adduct reaction between the epoxide groups of MGO and the EMI-2,4) can be neglected, thus, ΔH can be considered as a constant over the whole reaction and the reaction rate $d\alpha/dt = d\ (\Delta H_T/\Delta H)/dt = (1/\Delta H)dH/dt$.

Besides, DGEBA-MGO reaction occupies an important position in the cure reaction, considering the fact that the massive –OH on/within MGO sheets also exerts catalytic effect in initiating the etherification reaction with DGEBA, establishing C–O–C bonds at the MGO/epoxy interface as depicted in Figure 4b, which was supported by the works on the coupling of epoxy onto GO sheets [20, 29] as well as the usage of oxidized graphene as curing agent in assisting the crosslinking of epoxy [32, 33], and also was supported in this work by the evidence that ΔH value of the 2 wt% MGO/epoxy composite exceeds that of pure epoxy standardized by the same epoxy curing degree α_{IR} (see Table 1), i.e. ΔH (2 wt% MGO/epoxy composite, 544.2 J/g) > 0.99/0.92 ΔH (pure epoxy, 495.2 J/g).

The parabolic shape of the curves of $d\alpha/dt$ vs. α in Figure 5b indicates that the addition of 2 wt% MGO doesn't change the autocatalytic mechanism of DGEBA/EMI-2,4 system [31].

3.3.2. Reaction kinetics of the 2 wt% MGO/DGEBA/6 wt% EMI-2,4 system

All kinetic studies can start with the basic equation, and for thermosetting resins, $d\alpha/dt$ is expressed as Equation (2) [31]:

$$\frac{d\alpha}{dt} = Ae^{-E/RT}f(\alpha) \tag{2}$$

where A is the frequency factor, E is the activation energy, R is the gas constant, T is the absolute temperature at time t, and $f(\alpha)$ is a function of conversion α.

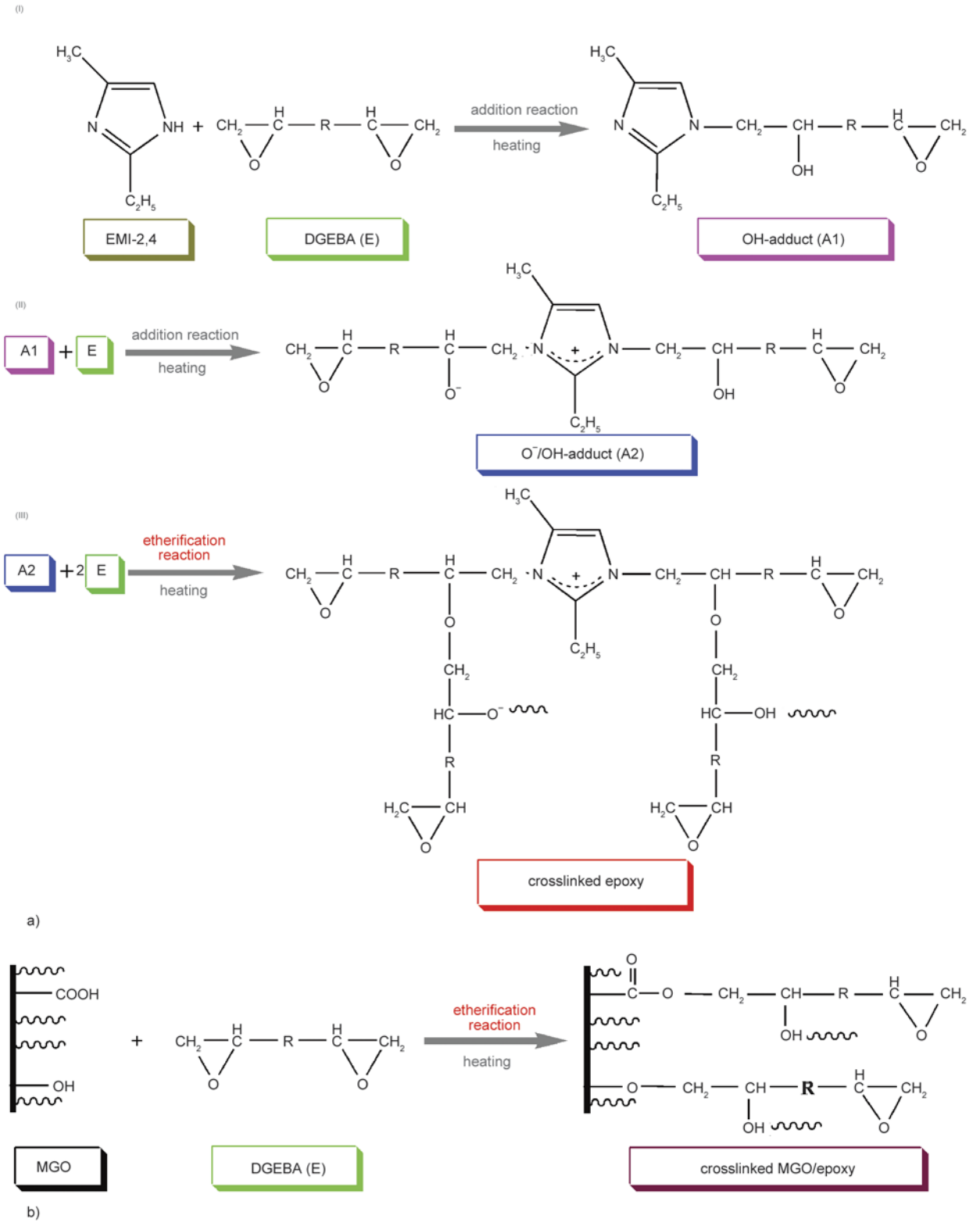

Figure 4. (a) curing mechanism of DGEBA/EMI-2,4 system and (b) schematic presentation of DGEBA-MGO reactions

then: $\ln\left(\frac{d\alpha}{dt}\right) = \ln A - \frac{E}{RT} + \ln f(\alpha)$

let $Af(\alpha) = F(\alpha)$, then get Equation (3):

$$\ln\left(\frac{d\alpha}{dt}\right) = -\frac{E}{RT} + \ln F(\alpha) \quad (3)$$

Isoconversional method, by which the effect of nano-sized SiC particles on the curing kinetics of DGEBA/6 wt%EMI-2,4 system was well established [31, 34], was also employed herein. From Equation (3), a plot of $\ln(d\alpha/dt)$ vs. $1/T$ at the same α from a series of DSC experiments at different heating rates would result

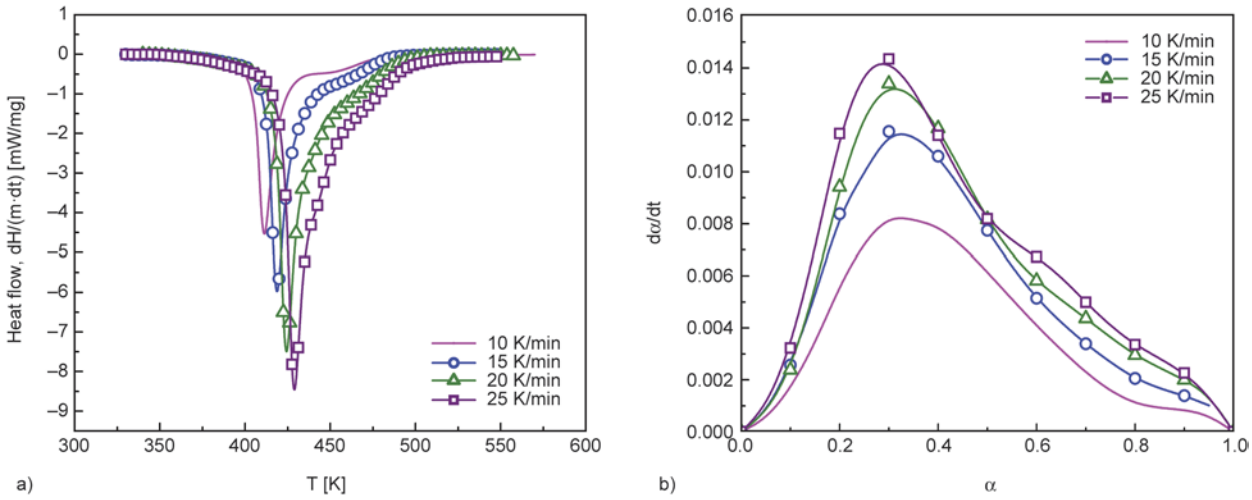

Figure 5. DSC curves (a) and plots of dα/dt vs. α (b) of the 2 wt% MGO/DGEBA/6 wt% EMI-2,4 system. Curves are given only for showing the tendency.

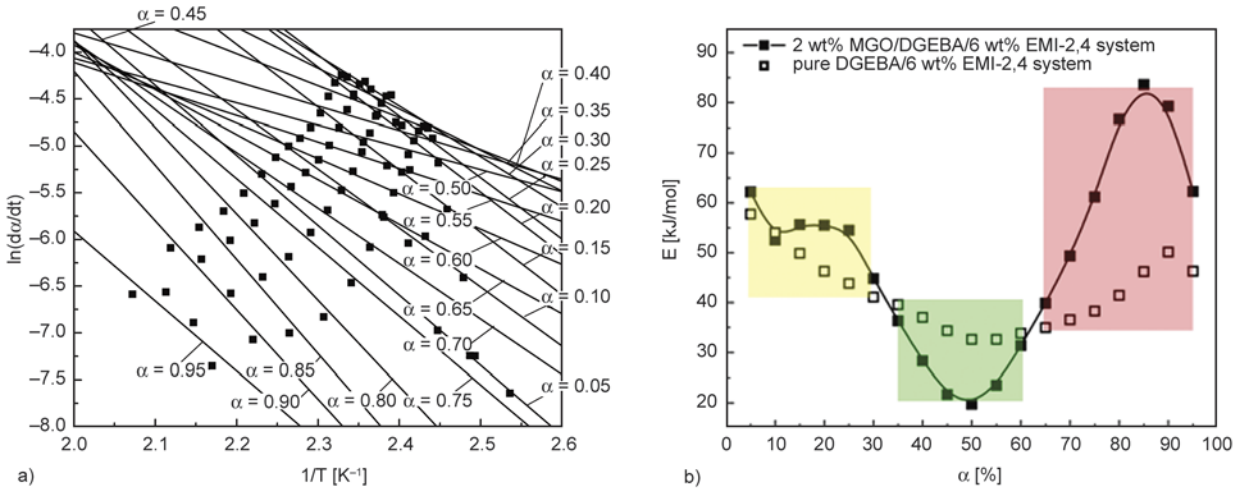

Figure 6. (a) Plots of ln(dα/dt) vs. 1/T of 2 wt% MGO/DGEBA/6 wt% EMI-2,4 system; (b) plots of E vs. α of 2 wt% MGO/DGEBA/6 wt% EMI-2,4 system (curve is given only for showing the tendency) and DGEBA/6 wt% EMI-2,4 system (for comparison)

in a straight line with a slope of $-E/R$. Repeating this procedure, $E(\alpha)$ values corresponding to different α can be obtained. Figure 6a presents the plots of ln(dα/dt) vs. 1/T for various α (α = 0.05, 0.10, …, 0.90, 0.95), based on which the plots of $E(\alpha)$ vs. α were obtained (see Figure 6b). It can be seen that $E(\alpha)$ of the 2 wt% MGO filled system changes momentarily, spanning within 19.7~83.6 KJ/mol, a broader scope than that of DGEBA/6 wt% EMI-2,4 system (34.3~63.8 KJ/mol). The advantage of isoconversional method is that it determines $E(\alpha)$ without assuming any model and uses most of the information from curing curves, thus compared with a single E averaged over the whole reaction obtained by other methods, $E(\alpha)$ has the advantage in detecting the complexity of reaction process, such as the change from chemical-kinetic control to diffusion control [34].

3.3.3. Formation mechanism of the 2 wt% MGO/epoxy percolating network based on the real-time $E(\alpha)$

A stage-dependent influence of 2 wt% MGO percolating chains on $E(\alpha)$ is noticed in Figure 6b. Although low content of EMI-2,4 was used to suppress adduct reactions, adduct products A2 are the origins of crosslinking, thus analysis on the formation process of the 2 wt% MGO/epoxy percolating network, based on the real-time $E(\alpha)$ presented in Figure 6b, starts as follows:

(a) Adduct reactions (see Stages (i–ii) in Figure 7). Adduct reactions preferentially occur around MGO percolating chains, the preferred heat-flow pathways as pre-heating temperature is applied (Stage (i)), however, each EMI-2,4 molecule only reacts with two neighboring epoxy

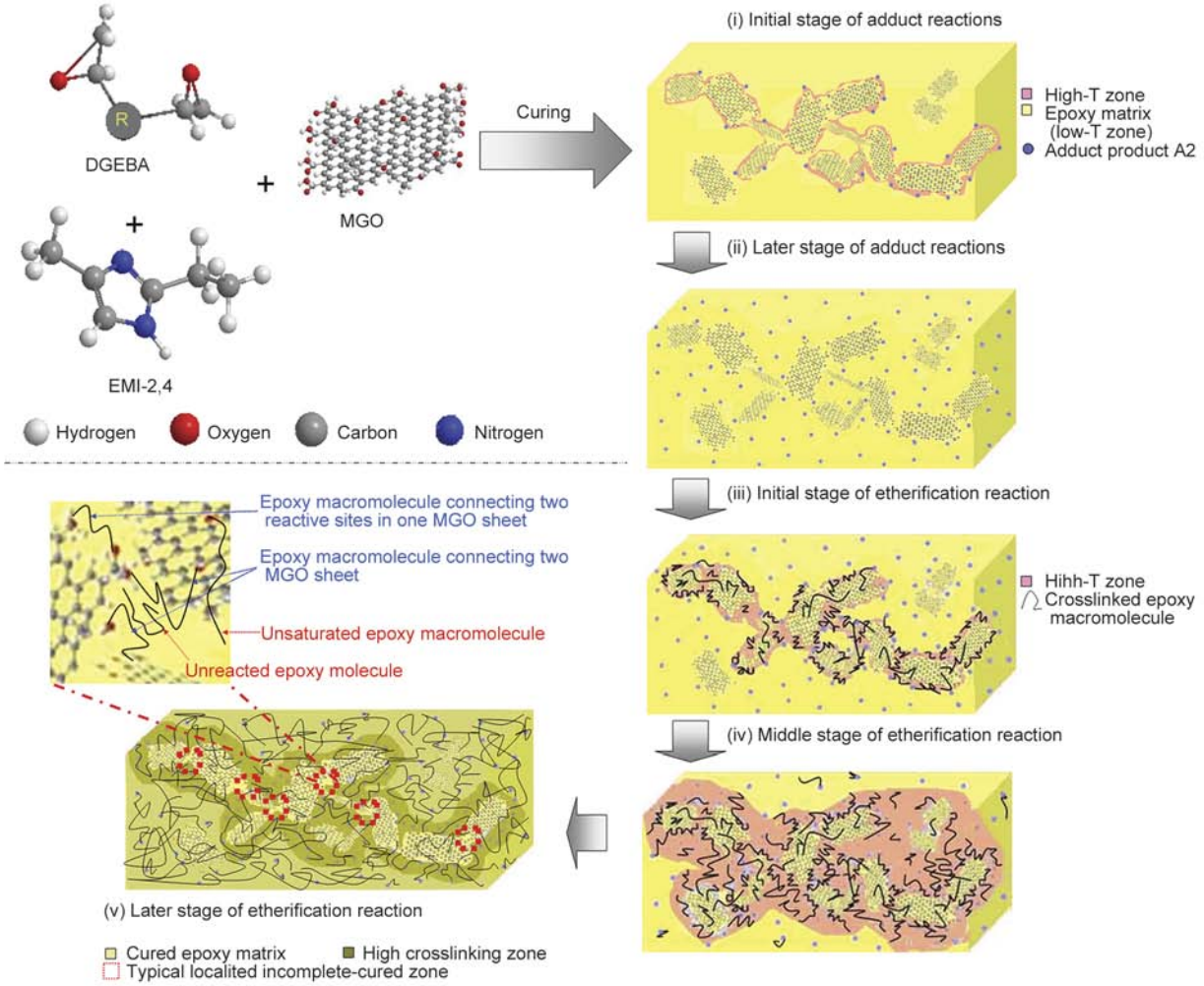

Figure 7. Schematic presentation of the crosslinking process of the MGO/epoxy percolating network

molecules before adduct reactions finish, finally, evenly distributed EMI-2,4 leads to evenly distributed resultant A2 (Stage (ii)).

(b) Etherification reaction (see Stages (iii–v) in Figure 7).

Once curing temperature is applied, etherification reaction also prefers to occur firstly around/within the heat-flow preferred MGO percolating chains (see Stage (iii)). Initially ($\alpha \leq 0.1$), catalyst A2 and epoxy molecules diffuse around freely to find and react with each other; some epoxy molecules graft directly onto MGO, thus the MGO percolating chains are soon wrapped by crosslinked epoxy. Then, large amount of epoxy need skirt around these crosslinked MGO/epoxy to find and react with unreacted/unsaturated epoxy, reflected by an increased E ($0.1 < \alpha \leq 0.3$) as compared with that of counterpart stage of pure epoxy system.

Subsequently, localized networks grow into surrounding MGO-poor zone (Stage (iv)). The process is intrinsically fluent due to its autocatalytic nature [34], and particularly, driven by the temperature gradient within sample, reflected by the marked decrease in E ($0.35 \leq \alpha \leq 0.6$) as compared with pure epoxy system and an advanced gelation (liquid-to-rubber transition, inflection point: pure epoxy: $\alpha = 0.55$; composite: $\alpha = 0.5$).

Significantly, at the final curing stage ($\alpha \geq 0.65$), even if further increases the curing temperature to post-heating temperature, an unprecedentedly sharp rise in E appears as compared with that of pure epoxy system, suggesting an unprecedented energy barrier hindering the residual epoxy to diffuse and react, especially those isolated within MGO-MGO interspace (see the enlargement of the boxed zones in Stage (v)) or trapped within the zone around MGO percolating chains where etherification is intensively initiated (see Stage (v)).

During the curing process, it is possible that T_g increases over heating temperature, then system vitrifies (rubber-to-glass transition) and reaction

becomes diffusion controlled. The effect of 2 wt% MGO percolating chains on T_g arises from an antagonistic competition of two effects. Apart from a catalytic activity of graphitic layers on the curing of epoxy/diamine system, so far increased T_g for epoxy resins in presence of small amount of GO (≤0.5 wt% GO [21, 32]) are mainly attributed to the reaction of epoxide with functional groups of GO [27]. In this work, the chemical bonding in MGO/epoxy interface, as well as physical hindrance of 2 wt% MGO percolating chains, greatly hampered epoxy motion as reflected by the sharp rise in E at the final curing stage, which contributes to an increase in T_g since T_g increases with the increasing restriction imposed by crosslinking on epoxy motion [31]. On the other hand, 2 wt% MGO percolating chains disrupt the crosslinking of matrix [27] and the tremendous MGO/epoxy interface creates extra free volume assisting the epoxy motion [31], which contributes to a lowering effect on T_g.

Most importantly, although the curing of pure epoxy system met with lower energy barrier as shown in Figure 6b, α_{IR} of pure epoxy finally saturated at 0.92, lower than that of 2 wt% MGO/epoxy composite (0.99, see Table 1). In fact such difference is observed only for freshly prepared samples, α_{IR}s of both pure epoxy and 2 wt% MGO/epoxy composite approached 1.0 (the difference nearly disappears) after aging at room temperature for 6 months or thermal annealing at 523 K for 1 week (crosslinking can proceed as a consequence of aging or thermal annealing [27]). These results clearly suggest that the steep concentration gradient of –OH, originated from the 2 wt% MGO percolating chains, exerted the vital driving force on the residual epoxy (isolated within MGO-MGO interspace or trapped within the zone around MGO percolating chains where etherification was intensively initiated) to conquer barrier for epoxy-MGO reaction, leading to the final lowering effect on T_g and higher α_{IR} of 2 wt% MGO/epoxy composite (see Table 1).

3.4. Promoting intercalative crosslinking within MGO makes epoxy composite with improved thermal conductivity

Through kinetic investigation, it is clarified that epoxy-MGO reaction plays an important role at the initial and final curing stage of epoxy containing 2 wt% MGO percolating chains. MGO based composites can be produced via *in-situ* intercalative polymerization [12]. Now, we turn our attention to the full utilization of *in-situ* intercalative crosslinking for the performance improvement of the composite, which need the guidance of the understanding on epoxy-MGO reaction.

Epoxy-MGO reaction can be studied based on Shrinking Core Model (SCM), the best representation for reacting fluid-particle systems [34–36]. In this work, the original sphere-shell model was modified with a cylinder-shell model customized for the special layered-structure of MGO sheet, as depicted in Figure 8.

Table 1. DSC-determined total heats of reaction (ΔH) and glass transition temperatures (T_g) at 10 K/min heating rate; FTIR-determined epoxy curing degree (α_{IR})

Sample	ΔH [J/g]	T_g [K]	α_{IR}
2 wt% MGO/DGEBA/EMI-2,4 system	544.2±2.9	399.7±0.5	0.99±0.01
DGEBA/EMI-2,4 system	495.2±1.2	418.6±0.6	0.92±0.01

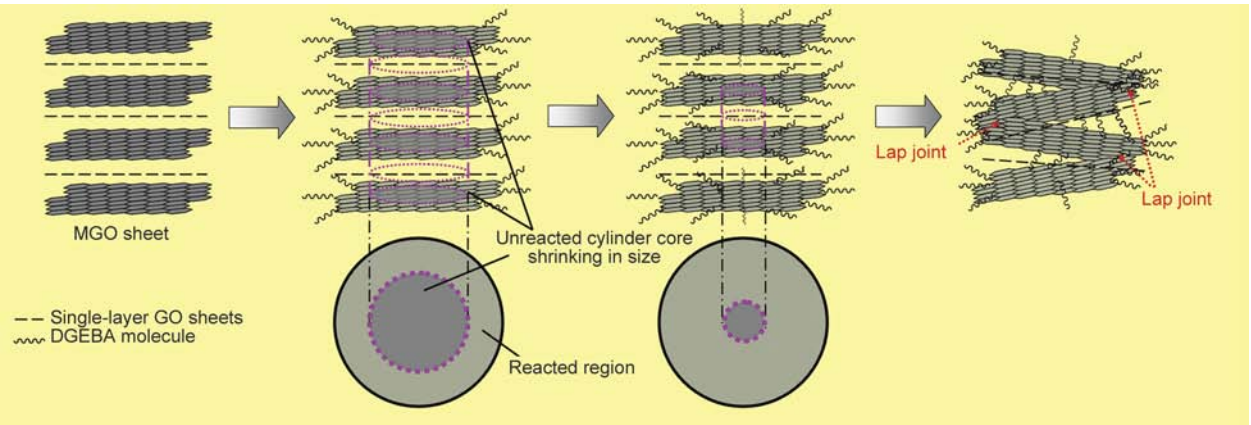

Figure 8. Schematic presentation of epoxy-MGO intercalative crosslinking by modified Shrinking Core Model

Epoxy-MGO reaction occurs first at the outer skin of MGO sheet, and then the zone of reaction would move into inter-layer and leave behind reacted cylindrical region. Three steps occur in succession: (1) diffusion of DGEBA molecule through the liquid film surrounding the MGO chains to the surface of MGO, (2) penetration into the inter-layer spacing of MGO and diffusion of DGEBA molecule through the reacted region to the surface of unreacted cylinder core part, (3) reaction of DGEBA molecule with the unreacted cylinder core at the interface of reacted region and unreacted core region. The resistance of the different steps usually varies greatly from one and the other; in such cases we may consider that the step with the highest resistance to be rate-controlling.

In fact, the relative importance of these steps will vary as the intercalation progresses, for example, the liquid film resistance increases as the concentration of –OH, which is the driving force for the diffusion, is decreasing as the intercalation proceeds. Therefore, the progressive intercalation crosslinking is controlled in succession by chemical reaction, reacted layer diffusion, and film diffusion. These resistances act in series, and the total resistance increases as the intercalation proceeds, which also contributes to the increase of E at the final curing stage ($\alpha \geq 0.65$). A representative schematic of resultant epoxy/MGO intercalative crosslinking structure is depicted in Figure 8 despite other possible configurations for the complexity of the reaction. Promoted intercalative crosslinking increases the probability of layer-layer lap (based on the fact that each epoxy molecule bears two terminal epoxide groups and it is inevitable that some epoxy molecules bridge neighboring layers, shorten interlayer gap, and produce more lap joints) and thus enhances the cross-plane thermal-transport ability of MGO. Therefore, promoted intercalative crosslinking is highly desirable as can open a new door for further improving the thermal conductivity of the epoxy composite containing MGO percolating chains, although it meets with higher resistance.

As proved by WXRD results, there is a complete disorder in the direction perpendicular to GO layers, corresponding to an exfoliation of 2 wt% MGO by intercalation in epoxy matrix. However, a lowered T_g due to the presence of 2 wt% MGO percolating chains keeps the whole cure reaction under long-term chemical kinetic control [34], therefore, it can be inferred that the *in-situ* intercalative crosslinking mainly occurs at the fringe of MGO layers, and the presently utilized cure processing strategy of pure epoxy is basically adequate for the isolated/trapped epoxy molecules to conquer barriers for such intercalation at the fringe of MGO layers, but for promoting the intercalative crosslinking, systematic experiments need to be done to optimize the cure processing strategies.

Guided by the above exploration on the formation mechanism of the 2 wt% MGO/epoxy percolating network based on real-time $E(\alpha)$ as well as the analysis of epoxy-MGO reaction based on modified SCM, targeted optimization on the cure processing strategy was accordingly proposed, which obeys the following rules: (1) at the initial stage, the curing temperature or time should be a little bit increased or prolonged, respectively, (2) at the middle stage, the curing temperature or time could be moderately decreased or shortened, respectively, (3) at the later stage, the curing temperature or time should be considerably increased or prolonged, respectively. Since the increased temperature is preferred to the prolonged time from the point of high efficiency, referring to the dynamic DSC curves in Figure 5a, a series of improved cure processing strategies was designed as tabulated in Table 2 (the curing parameters at the middle stage were fixed).

The resulting thermal conductivities presented in Figure 9 clearly shows that, increased pre-heating or post-heating temperature does bring positive effect and comparatively, pre-heating temperature has less significant effect, which can be ascribed to the fact that the deficiency in the pre-heating stage could be compensated by the following middle and/or later curing stage. Notably, S3 strategy imparts a remarkable increase in thermal conductivity (2.96 times that of epoxy), much higher than that of composite cured by the basic strategy (2.03 times that of epoxy) and similar 2 wt% GO/epoxy composites reported [2, 37]. Further increases in thermal conductivity due to further increased curing temperatures in S4–S8 strategies is at slight degrees, specifically, to a maximum, 3.05 times that of pure epoxy (S5 strategy), indicating that thermal conductivity enhancement saturates at the S3 strategy, a strategy unprecedentedly promoting the intercalative crosslinking within MGO sheets.

Interestingly, a similar saturation phenomenon was also noticed in CTE values. As shown in Figure 10a, composite cured by the basic strategy displays a

Table 2. Basic (cure processing strategy of pure epoxy) and improved strategies for 2 wt% MGO/epoxy composite, the curing parameters at the middle stage were fixed as 378 K×1.5 h; thermal degradation data determined from TGA curves

Strategies	Curing parameters	T_{onset} [K]	T_{half} [K]	T_{max} [K]	Char residual at 1023 K [%]
Basic	313 K×1 h, 458 K×1.5 h	686.4±0.1	710.8±0.2	710.9±0.2	13.2±0.1
S1	333 K×1 h, 458 K×1.5 h	686.4±0.1	710.3±0.1	710.5±0.2	13.2±0.2
S2	353 K×1 h, 458 K×1.5 h	686.4±0.2	710.4±0.2	710.2±0.1	13.2±0.1
S3	313 K×1 h, 488 K×1.5 h	693.5±0.2	719.4±0.3	719.3±0.2	12.2±0.1
S4	333 K×1 h, 488 K×1.5 h	693.3±0.1	719.9±0.2	719.6±0.3	12.4±0.1
S5	353 K×1 h, 488 K×1.5 h	693.2±0.2	720.1±0.2	719.9±0.2	12.3±0.1
S6	313 K×1 h, 518 K×1.5 h	695.9±0.3	721.4±0.1	720.5±0.2	12.3±0.1
S7	333 K×1 h, 518 K×1.5 h	695.9±0.2	720.4±0.1	720.8±0.3	12.0±0.2
S8	353 K×1 h, 518 K×1.5 h	695.8±0.2	721.9±0.2	721.5±0.1	12.1±0.1

23% reduction in CTE due to the relatively rigid characteristic of MGO and the restricted epoxy motion near MGO/resin interface evidenced by the typical plastic deformation on the fracture surface in Figure 3c. The obtained CTE value is comparable with the reported results [22, 38]. With S3 strategy, a further marked decrease, up to a 43% reduction in CTE, was achieved; then further decrease in CTE due to further increased curing temperature is at a slight extent, specifically from 43% to the maximum 44% reduction in CTE (S8 strategy), which confirms that S3 strategy unprecedentedly promoted the intercalative crosslinking thus making MGO sheets act at full capacity in restricting the thermal expansion behavior of epoxy by their inter-layer MGO/resin interface.

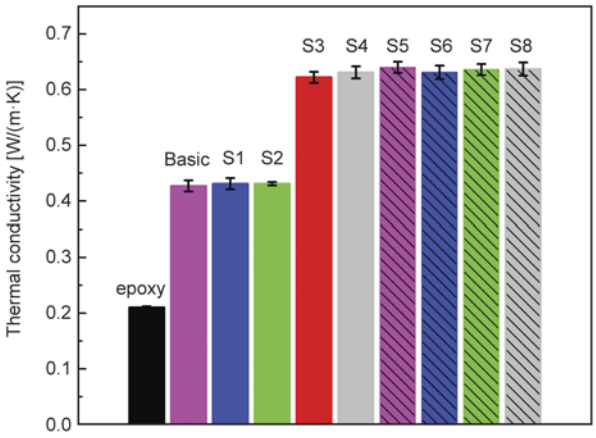

Figure 9. Thermal conductivities of 2 wt% MGO/epoxy composites obtained by the basic (cure processing strategy of pure epoxy) or improved cure processing strategies

Furthermore, TGA and DTG curves (Figure 10b) exhibit a delayed thermal degradation by 2 wt% MGO/epoxy percolating network. For the highly-overlapped TGA and DTG cures obtained by improved cure processing strategies, the thermal degradation onset temperature T_{onset} (determined by the intersection of two tangents at the first inflection point), the half-weight-loss temperature T_{half}, the maximum thermal degradation temperature T_{max} (determined by the peak of DTG curve), and the char residual at 1023 K were summarized in Table 2. It

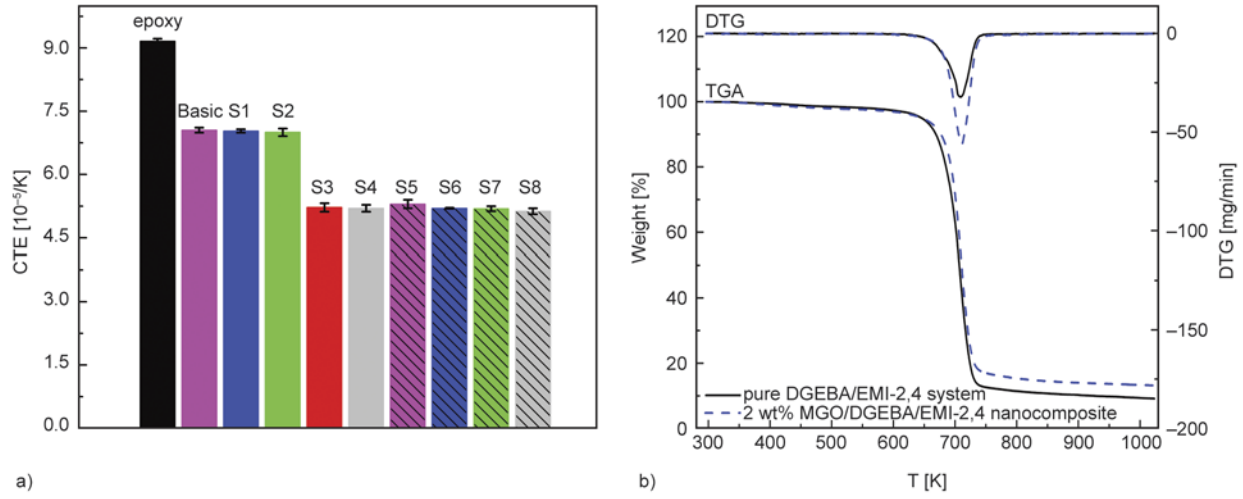

Figure 10. (a) CTE values of 2 wt% MGO/epoxy composites obtained by the basic or improved cure processing strategies, (b) TGA and DTG curves of 2 wt% MGO/epoxy composite obtained by the basic cure processing strategy

is a common practice to consider T_{half} or T_{max} (at which weight losing rate is the maximum) as an indicator for the beginning of structural decomposition. Clearly, a significant increase in T_{onset}, T_{half} and T_{max} (specifically, 7.1, 8.6 and 8.4 K, respectively) appears at the S3 strategy with a slight further enhancement of thermal stability in S4–S8 strategies (2.4, 2.5 and 2.2 K, respectively), which reconfirms an unprecedentedly promoted intercalative crosslinking by S3 strategy thus favoring the strengthening of the effectiveness of percolating network in inhibiting the thermal degradation behavior [15].

Overall, S3 strategy is considered as the optimized cure processing strategy in this work after taking both the efficiency and the performance enhancement into account.

4. Conclusions

In this work, strategies involving MGO content (0.5, 1, 2, 2.2, 2.5, 3 wt%), exfoliation and dispersion level of MGO, and MGO/epoxy interfacial interaction were firstly taken into account to improve the thermal conductivity of epoxy. With 2 wt% MGO content, the thermal conductivity of epoxy composite reached a maximum, 2.03 times that of the epoxy. Then, one issue emerged, i.e. how to further improve the thermal conductivity of the epoxy containing 2 wt% MGO percolating chains.

Formation mechanism of 2 wt% MGO/epoxy percolating network was explored, for the first time based on real-time $E(\alpha)$. The presence of 2 wt% MGO percolating chains leads to an unprecedentedly sharp rise in E at final curing stage ($\alpha \geq 0.65$), but an increased α_{IR} (0.99) is observed as compared with that of pure epoxy (0.92). In fact such α_{IR} difference is observed only for freshly prepared samples, it nearly disappears after aging or thermal annealing. These results suggest that the steep concentration gradient of –OH, originated from the 2 wt% MGO percolating chains, exerts the vital driving force on the residual isolated/trapped epoxy to conquer barrier for epoxy-MGO reaction.

Through kinetic investigation, it is clarified that epoxy-MGO reaction plays an important role at the initial and final curing stage. A modified Shrinking Core Model customized for the special layered-structure of MGO sheet was proposed to understand the resistance variation during the intercalative epoxy-MGO reaction. It shows that the promoted intercalative crosslinking is highly desirable for further improving the thermal conductivity of the epoxy composite containing MGO percolating chains, but it meets with increased resistance.

Guided by these kinetic studies, targeted optimization on the cure processing strategy was accordingly proposed to promote the intercalative crosslinking, a thermal conductivity, 2.96 times that of the epoxy, was obtained with only a small amount (30°C) increase of the post-heating temperature.

The promoted intercalative crosslinking was confirmed by CTE and TGA results. This study provides a good example of using a targeted kinetic strategy in effectively improving the thermal conductivity of the epoxy containing MGO percolating chains.

Acknowledgements

The authors are grateful for the financial support of National Natural Science Foundation of China (No. 51203074), Fundamental Research Funds for the Central Universities (No. NUST 2011YBXM163), Jiangsu Overseas Research & Training Program for University Prominent Young & Middle-aged Teachers and Presidents, and Special Foundation for 'first-grade Zijin's Star' of 'Excellence initiative' Project of Nanjing University of Science and Technology (No. AB41339).

References

[1] Suganuma K.: Introduction to printed electronics. Springer Science, New York (2014). DOI: 10.1007/978-1-4614-9625-0

[2] Song S. H., Park K. H., Kim B. H., Choi Y. W., Jun G. H., Lee D. J., Kong B-S., Paik K-W., Jeon S.: Enhanced thermal conductivity of epoxy–graphene composites by using non-oxidized graphene flakes with non-covalent functionalization. Advanced Materials, **25**, 732–737 (2013). DOI: 10.1002/adma.201202736

[3] Sadasivuni K. K., Ponnamma D., Thomas S., Grohens Y.: Evolution from graphite to graphene elastomer composites. Progress in Polymer Science, **39**, 749–780 (2014). DOI: 10.1016/j.progpolymsci.2013.08.003

[4] Deng H., Lin L., Ji M., Zhang S., Yang M., Fu Q.: Progress on the morphological control of conductive network in conductive polymer composites and the use as electroactive multifunctional materials. Progress in Polymer Science, **39**, 627–655 (2014). DOI: 10.1016/j.progpolymsci.2013.07.007

[5] Sun X., Sun H., Li H., Peng H.: Developing polymer composite materials: Carbon nanotubes or graphene? Advanced Materials, **25**, 5153–5176 (2013). DOI: 10.1002/adma.201301926

[6] Wu J., Xing W., Huang G., Li H., Tang M., Wu S., Liu Y.: Vulcanization kinetics of graphene/natural rubber nanocomposites. Polymer, **54**, 3314–3323 (2013). DOI: 10.1016/j.polymer.2013.04.044

[7] Wang H., Qiu Z.: Crystallization kinetics and morphology of biodegradable poly(L-lactic acid)/graphene oxide nanocomposites: Influences of graphene oxide loading and crystallization temperature. Thermochimica Acta, **527**, 40–46 (2012). DOI: 10.1016/j.tca.2011.10.004

[8] Jing X., Qiu Z.: Crystallization kinetics and thermal property of biodegradable poly(3-hydroxybutyrate)/graphene oxide nanocomposites. Journal of Nanoscience and Nanotechnology, **12**, 7314–7321 (2012). DOI: 10.1166/jnn.2012.6461

[9] Zhang F., Peng X., Yan W., Peng Z., Shen Y.: Non-isothermal crystallization kinetics of *in situ* nylon 6/graphene composites by differential scanning calorimetry. Journal of Polymer Science Part B: Polymer Physics, **49**, 1381–1388 (2011). DOI: 10.1002/polb.22321

[10] Qiu S. L., Wang C. S., Wang Y. T., Liu C. G., Chen X. Y., Xie H. F., Huang Y. A., Cheng R. S.: Effects of graphene oxides on the cure behaviors of a tetrafunctional epoxy resin. Express Polymer Letters, **5**, 809–818 (2011). DOI: 10.3144/expresspolymlett.2011.79

[11] Allahbakhsh A., Mazinani S., Kalaee M. R., Sharif F.: Cure kinetics and chemorheology of EPDM/graphene oxide nanocomposites. Thermochimica Acta, **563**, 22–32 (2013). DOI: 10.1016/j.tca.2013.04.010

[12] Nicolosi V., Chhowalla M., Kanatzidis M. G., Strano M. S., Coleman J. N.: Liquid exfoliation of layered materials. Science, **340**, 1226419/1–1226419/18 (2013). DOI: 10.1126/science.1226419

[13] Huang Y. F., Lin C. W.: Polyaniline-intercalated graphene oxide sheet and its transition to a nanotube through a self-curling process. Polymer, **53**, 1079–1085 (2012). DOI: 10.1016/j.polymer.2012.01.025

[14] Bora C., Dolui S. K.: Fabrication of polypyrrole/graphene oxide nanocomposites by liquid/liquid interfacial polymerization and evaluation of their optical, electrical and electrochemical properties. Polymer, **53**, 923–932 (2012). DOI: 10.1016/j.polymer.2011.12.054

[15] Zeng M., Wang J., Li R., Liu J., Chen W., Xu Q., Gu Y.: The curing behavior and thermal property of graphene oxide/benzoxazine nanocomposites. Polymer, **54**, 3107–3116 (2013). DOI: 10.1016/j.polymer.2013.03.069

[16] Fabbri P., Valentini L., Bon S. B., Foix D., Pasquali L., Montecchi M., Sangermano M.: *In-situ* graphene oxide reduction during UV-photopolymerization of graphene oxide/acrylic resins mixtures. Polymer, **53**, 6039–6044 (2012). DOI: 10.1016/j.polymer.2012.10.045

[17] Huang Y. F., Lin C. W.: Facile synthesis and morphology control of graphene oxide/polyaniline nanocomposites *via in-situ* polymerization process. Polymer, **53**, 2574–2582 (2012). DOI: 10.1016/j.polymer.2012.04.022

[18] Kim H., Abdala A. A., Macosko C. W.: Graphene/polymer nanocomposites. Macromolecules, **43**, 6515–6530 (2010). DOI: 10.1021/ma100572e

[19] Zaman I., Phan T. T., Kuan H-C., Meng Q., Bao La L. T., Luong L., Youssf O., Ma J.: Epoxy/graphene platelets nanocomposites with two levels of interface strength. Polymer, **52**, 1603–1611 (2011). DOI: 10.1016/j.polymer.2011.02.003

[20] Wan Y-J., Tang L-C., Gong L-X., Yan D., Li Y-B., Wu L-B., Jiang J-X., Lai G-Q.: Grafting of epoxy chains onto graphene oxide for epoxy composites with improved mechanical and thermal properties. Carbon, **69**, 467–480 (2014). DOI: 10.1016/j.carbon.2013.12.050

[21] Tang L-C., Wan Y-J., Yan D., Pei Y-B., Zhao L., Li Y-B., Wu L-B., Jiang J-X., Lai G-Q.: The effect of graphene dispersion on the mechanical properties of graphene/epoxy composites. Carbon, **60**, 16–27 (2013). DOI: 10.1016/j.carbon.2013.03.050

[22] Ahmadi-Moghadam B., Taheri F.: Effect of processing parameters on the structure and multi-functional performance of epoxy/GNP-nanocomposites. Journal of Materials Science, **49**, 6180–6190 (2014). DOI: 10.1007/s10853-014-8332-y

[23] Wang F., Drzal L. T., Qin Y., Huang Z.: Mechanical properties and thermal conductivity of graphene nanoplatelet/epoxy composites. Journal of Materials Science, **50**, 1082–1093 (2015). DOI: 10.1007/s10853-014-8665-6

[24] Zhang K., Zhang Y., Wang S.: Effectively decoupling electrical and thermal conductivity of polymer composites. Carbon, **65**, 105–111 (2013). DOI: 10.1016/j.carbon.2013.08.005

[25] Zhang K., Zhang Y., Wang S.: Enhancing thermoelectric properties of organic composites through hierarchical nanostructures. Scientific Reports, **3**, 3448/1–3448/7 (2013). DOI: 10.1038/srep03448

[26] Guan L-Z., Wan Y-J., Gong L-X., Yan D., Tang L-C., Wu L-B., Jiang J-X., Lai G-Q.: Toward effective and tunable interphases in graphene oxide/epoxy composites by grafting different chain lengths of polyetheramine onto graphene oxide. Journal of Materials Chemistry A, **2**, 15058–15069 (2014). DOI: 10.1039/C4TA02429J

[27] Mauro M., Acocella M. R., Corcione C. E., Maffezzoli A., Guerra G.: Catalytic activity of graphite-based nanofillers on cure reaction of epoxy resins. Polymer, **55**, 5612–5615 (2014). DOI: 10.1016/j.polymer.2014.09.019

[28] Wan Y-J., Gong L-X., Tang L-C., Wu L-B., Jiang J-X.: Mechanical properties of epoxy composites filled with silane-functionalized graphene oxide. Composites Part A: Applied Science and Manufacturing, **64**, 79–89 (2014).
DOI: 10.1016/j.compositesa.2014.04.023

[29] Shen B., Zhai W., Tao M., Lu D., Zheng W.: Chemical functionalization of graphene oxide toward the tailoring of the interface in polymer composites. Composites Science and Technology, **77**, 87–94 (2013).
DOI: 10.1016/j.compscitech.2013.01.014

[30] Krishnan D., Kim F., Luo J., Cruz-Silva R., Cote L. J., Jang H. D., Huang J.: Energetic graphene oxide: Challenges and opportunities. Nano Today, **7**, 137–152 (2012).
DOI: 10.1016/j.nantod.2012.02.003

[31] Zhou T., Gu M., Jin Y., Wang J.: Studying on the curing kinetics of a DGEBA/EMI-2,4/nano-sized carborundum system with two curing kinetic methods. Polymer, **46**, 6174–6181 (2005).
DOI: 10.1016/j.polymer.2005.03.114

[32] Shen X-J., Pei X-Q., Fu S-Y., Friedrich K.: Significantly modified tribological performance of epoxy nanocomposites at very low graphene oxide content. Polymer, **54**, 1234–1242 (2013).
DOI: 10.1016/j.polymer.2012.12.064

[33] Patil V., Dennis R. V., Rout T. K., Banerjee S., Yadav G. D.: Graphene oxide and functionalized multi walled carbon nanotubes as epoxy curing agents: A novel synthetic approach to nanocomposites containing active nanostructured fillers. RSC Advances, **4**, 49264–49272 (2014).
DOI: 10.1039/c4ra09693b

[34] Zhou T., Gu M., Jin Y., Wang J.: Isoconversional method to explore the cure reaction mechanisms and curing kinetics of DGEBA/EMI-2,4/nano-SiC system. Journal of Polymer Science Part A: Polymer Chemistry, **44**, 371–379 (2006).
DOI: 10.1002/pola.21150

[35] Knorr T., Kaiser M., Glenk F., Etzold B. J. M.: Shrinking core like fluid solid reactions – A dispersion model accounting for fluid phase volume change and solid phase particle size distributions. Chemical Engineering Science, **69**, 492–502 (2012).
DOI: 10.1016/j.ces.2011.11.002

[36] Shi B-H., Fan S-S., Lou X.: Application of the shrinking-core model to the kinetics of repeated formation of methane hydrates in a system of mixed dry-water and porous hydrogel particulates. Chemical Engineering Science, **109**, 315–325 (2014).
DOI: 10.1016/j.ces.2014.01.035

[37] Kim J., Yim B-S., Kim J-M., Kim J.: The effects of functionalized graphene nanosheets on the thermal and mechanical properties of epoxy composites for anisotropic conductive adhesives (ACAs). Microelectronics Reliability, **52**, 595–602 (2012).
DOI: 10.1016/j.microrel.2011.11.002

[38] Wang S., Tambraparni M., Qiu J., Tipton J., Dean D.: Thermal expansion of graphene composites. Macromolecules, **42**, 5251–5255 (2009).
DOI: 10.1021/ma900631c

eXPRESS Polymer Letters Vol.9, No.7 (2015) 624–635
Available online at www.expresspolymlett.com
DOI: 10.3144/expresspolymlett.2015.58

Influence of deformation temperature on structural variation and shape-memory effect of a thermoplastic semi-crystalline multiblock copolymer

W. Yan[1,2], *L. Fang*[1], *U. Noechel*[1], *K. Kratz*[1], *A. Lendlein*[1,2*]

[1]Institute of Biomaterial Science and Berlin-Brandenburg Center for Regenerative Therapies, Helmholtz Zentrum Geesthacht, Kantstr. 55, 14513 Teltow, Germany
[2]Institute of Chemistry, University of Potsdam, 14476 Potsdam, Germany

Received 17 November 2014; accepted in revised form 31 January 2015

Abstract. A multiblock copolymer termed as PCL-PIBMD, consisting of crystallizable poly(ε-caprolactone) (PCL) segments and crystallizable poly(3*S*-isobutyl-morpholine-2,5-dione) (PIBMD) segments, has been reported as a material showing a thermally-induced shape-memory effect. While PIBMD crystalline domains act as netpoints to determine the permanent shape, both PCL crystalline domains and PIBMD amorphous domains, which have similar transition temperatures (T_{trans}) can act as switching domains. In this work, the influence of the deformation temperature (T_{deform} = 50 or 20°C), which was above or below T_{trans}, on the structural changes of PCL-PIBMD during uniaxial deformation and the shape-memory properties were investigated. Furthermore, the relative contribution of crystalline PCL and PIBMD amorphous phases to the fixation of the temporary shape were distinguished by a toluene vapor treatment approach. The results indicated that at 50°C, both PCL and PIBMD amorphous phases can be orientated during deformation, resulting in thermally-induced crystals of PCL domains and joint contribution to the switching domains. In contrast at 20°C, the temporary shape was mainly fixed by PCL crystals generated via strain-induced crystallization.

Keywords: *biodegradable polymers, shape-memory polymer, multiblock copolymer, polydepsipeptide*

1. Introduction

Shape-memory polymers (SMPs) can be deformed from their permanent shape and temporarily fixed in a second shape. The original shape can be recovered by application of suitable external stimulus, such as e.g. heat [1–6]. Suitable molecular architectures consisting of netpoints determining the permanent shape and molecular switches fixing the temporary shape are required to enable a shape-memory effect (SME) in polymers [1–3]. Multiblock copolymers (MBCs) consisting of at least two segregated domains, thus, are considered as a versatile molecular architecture in creating SMPs [1, 2, 6–8]. Recently, a novel class of MBCs composed of crystallizable poly(ε-caprolactone) (PCL) segments and crystallizable poly(3*S*-isobutyl-morpholin-2,5-dione) (PIBMD) segments was introduced and termed as PCL-PIBMD. It has been reported that excellent SME can be found in PCL-PIBMD with 50 wt% PIBMD segments [6–8]. In addition, while PIBMD crystals with a high melting temperature (T_m) of 170°C act as permanent physical netpoints, the melting temperature of PCL crystallites ($T_{m,PCL} \approx 38$°C) is close to the glass transition temperature of PIBMD ($T_{g,PIBMD} \approx 42$°C) domains [6–8]. Therefore, both the PCL crystalline phase and the PIBMD amorphous phase form the switching domains.

*Corresponding author, e-mail: andreas.lendlein@hzg.de

The deformation temperature (T_{deform}) has significant effects on deformation behaviors of semi-crystalline polymers on the microscopic and macroscopic scale [9, 10], with structural variations during the deformation playing a dominant role in determining their mechanical properties [11, 12]. It also has been reported that T_{deform} can affect the SME of semi-crystalline MBCs, i.e., if the samples are deformed at a temperature lower than the thermal transition temperature (T_{trans}) of switching domains, reduction in fixity ratio (R_f) and switching temperature (T_{sw}) can be observed as well as a higher maximum stress (σ_m) is required [13–14]. Therefore, it is necessary to explore the mechanisms of structural evolutions in semi-crystalline MBCs deformed at different temperatures to gain further insights into structure/property−function relations for mechanical properties and the shape-memory capability. As far as PCL-PIBMD is concerned, the PIBMD amorphous phase in PCL-PIBMD will be in the rubbery state if PCL-PIBMD is deformed at a temperature higher than $T_{g,PIBMD}$. Its structural response during deformation should be different from the case in which the PIBMD amorphous phase is in the glassy state if PCL-PIBMD is deformed at a temperature lower than $T_{g,PIBMD}$. Such difference is anticipated to cause distinct SMEs as well as the variation in the relative contributions of PIBMD amorphous phase and PCL crystals to switching domains.

In this work, the structural variations of PCL-PIBMD (with a 50 wt% PIBMD) deformed to a strain of 200% at T_{deform} = 20 or 50°C, which are below and above $T_{g,PIBMD}$, were studied by means of differential scanning calorimetry (DSC), atomic force microscopy (AFM), wide-angle X-ray scattering (WAXS) and small-angle X-ray scattering (SAXS). The corresponding shape-memory properties were evaluated via cyclic, thermomechanical tensile testing. Furthermore, a new method of toluene vapor treatment was applied in order to separate the relative contributions of PCL crystalline phase and PIBMD amorphous phase to switching domains.

2. Experimental

2.1. Materials

PCL-diol with number average molecular weight (M_n) of 2700 g·mol^{-1} and a polydispersity of 1.7 was obtained from Solvay Caprolactones (Warrington, UK). PIBMD-diol with a number averaged molecular weight M_n = 9300 g·mol^{-1} was prepared by ring open polymerization of morpholine-2,5-diones in the melt using $Sn(Oct)_2$ as catalyst according to Ref. [6]. Other reagents, such as 2,2(4),4-trimethyl-hexamethylene diisocyanate, (TMDI, Aldrich, Taufkirchen, Germany), amino acids (Aldrich, Taufkirchen, Germany) and solvents (Merck, Darmstadt, Germany) were of commercial grade and used without further purification.

As reported in Ref. [6], for synthesis of PCL-PIBMD containing 50 wt% PIBMD, 24.0 g PCL-diol was reacted with 22.5 g PIBMD-diol and 3.32 mL TMDI in 110 mL *N*-methylpyrrolidone at 80°C for 24 h by using 43 µL dibutyltin dilaurate as catalyst. Subsequently, another 100 µL TMDI was added to the mixture to react for another 24 h. After reaction, the mixture was diluted with 200 mL 1,2-dichloroethane and precipitated in a tenfold excess of diethyl ether. The product was collected by suction filtration and dried in a vacuum at room temperature for 24 h. The M_n of the PCL-PIBMD product was 53 000 g·mol^{-1} with polydispersity of 2.0, determined by gel permeation chromatography (GPC).

2.2. Film preparation

PCL-PIBMD (2.28 g) was dissolved in chloroform (50 mL) overnight at ambient temperature. The solution casting was carried out in glass petri dishes (diameter = 80 mm, Duran Group, Wertheim, Germany) with subsequent evaporation of chloroform for 5 days. The resulting film thickness was 270±30 µm, measured using a thickness gauge (Hans Schmidt, Waldkraiburg, Germany).

2.3. Characterization methods

2.3.1. Gel permeation chromatography (GPC)

Multidetector GPC measurements were performed using chloroform as eluent with a flow rate of 1 mL·min^{-1} and 0.2 wt% toluene as internal standard at 35°C. The system was equipped with a precolumn, two 300 mm×8.0 mm linear M columns (Polymer Standards Service GmbH, (PSS) Mainz, Germany) an isocratic pump 2080 and an automatic injector AS 2050 (both Jasco, Tokyo, Japan). Three detectors were used: a UV detector UV-1575 (Jasco, 275 nm): a RI detector Shodex RI-101 (Showa Denko, Japan) and the viscometer SEC-3010 (WGE, Dr. Bures, Dallgow, Germany) which were combined by a split. The molecular weights were determined using a universal calibration with polystyrene standards with M_n between 580 g·mol^{-1} and

975 000 g·mol^{-1} (PSS) and with the help of the SEC software WINGPC Unity (PSS).

2.3.2. Atomic force microscopy (AFM)

The morphologies of solution cast films before and after deformation at different T_{deform}s were investigated by AFM (Multimode with NanoScope V Controller, Veeco Instruments Inc.) with a temperature controller (Veeco Thermal Application Controller). The typical scan rate was 0.8–1.0 Hz. The silicon cantilevers (OLYMPUS OMCL AC200TS-R3), having a driving frequency of around 150 KHz and a spring constant of 9 N·m^{-1}, were used for measurements. The tip has a radius of 7 nm and its back and side angles are 35° and 18°, respectively.

2.3.3. Differential scanning calorimetry (DSC)

DSC experiments were conducted on a Netzsch DSC 204 Phoenix (Selb, Germany) at a heating rate of 10°C·min^{-1} in sealed aluminum pans. The polymer samples were cooled down from room temperature to 0°C before they were heated to 200°C, while the T_m and related melting enthalpies (ΔH) were determined from DSC curves. A non-deformed PCL-PIBMD sample was measured after being preconditioned by annealing at 75°C for 10 min, then cooling down to 50°C and keeping for 10 min at T_{deform}, and afterwards cooling to 0°C with a cooling rate of 5°C·min^{-1} by using DSC to simulate the main thermal treatment applied during programming. The deformed samples were prepared as described in the following section 2.3.4.

2.3.4. Cyclic, thermomechanical tensile tests

Cyclic, thermomechanical, tensile tests were performed on a tensile tester (Zwick Z1.0, Ulm, Germany) equipped with a thermo chamber and a temperature controller (Eurotherm Regler, Limburg, Germany). Each cycle consisted of a shape-memory creation procedure (SMCP) and recovery modules, which can be performed under two different conditions: stress-free or constant-strain. The cycles were repeated three times per test.

Programming (SMCP) was performed using test specimens which were cut from the solution cast films according to the type DIN EN ISO 527-2/1BB (length = 20 mm, width = 2 mm). The specimen was heated up from room temperature to the upper working temperature (T_{high} = 75°C). After 10 min, the temperature was reduced to T_{deform} = 50 or 20°C at 5°C·min^{-1}. After another 5 min, the specimen was deformed to the strain of ε_m = 200% at a deformation speed of 1 mm·min^{-1}. Subsequently, the deformed specimen was kept at T_{deform} for 5 min to allow relaxation. Then, the specimen was cooled down to lower temperature (T_{low} = 0°C) under constant-strain condition and equilibrated for 10 min. Finally, the stress was removed and the temporary fixed elongation temporary strain (ε_u) was determined.

Recovery under stress-free condition was induced by heating the programmed sample from 0 to 75°C at 2°C·min^{-1} under stress-free condition. The switching temperature (T_{sw}) and recovery strain (ε_p) were determined.

Recovery under constant-strain condition was carried out after completion of the programming module by increasing the temperature from 0 to 75°C at 2°C·min^{-1}. σ_{max} and its corresponding temperature ($T_{\sigma,max}$) were determined at the maximum value of σ in the stress-temperature curve. The stress was completely released after reaching T_{high} to allow the sample recovery. The characteristics for quantification of SME, R_f and shape recovery ratio (R_r), can be calculated by Equations (1) and (2) [1]:

$$R_f = \frac{\varepsilon_u(N)}{\varepsilon_m} \tag{1}$$

$$R_r = \frac{\varepsilon_m - \varepsilon_p(N)}{\varepsilon_m - \varepsilon_p(N-1)} \tag{2}$$

where N is the present N^{th} cycle of cyclic test.

2.3.5. Wide-angle X-ray scattering (WAXS)

WAXS measurements were performed on the Bruker D8 Discover X-ray diffraction system with a two-dimensional detector from Bruker AXS (Karlsruhe, Germany). The X-ray generator was operated at 40 kV and 40 mA on a copper-anode. The collimator was chosen 0.8 mm (beam size). The two-dimensional detector (Hi-Star) was operated in 1024× 1024 pixel mode. The distance sample-detector was 150 mm and the wavelength λ = 0.15418 nm. The detector was positioned at an angular position 2θ = 25° in order to cover an angular range from 2θ = 7.2 to 43.5°. Exposure time was 120 s per scattering pattern. The raw patterns (two-dimensional) were all isotropic, thus a one-dimensional curve contains the same information as the 2D-pattern. Then an integration over an angle chi χ = 120° and the whole 2θ-range was performed in order to obtain 1D-scatter-

ing curves using 5-point normalized binning. Non valid data points outward of the detector were not considered for integration. The scattering curves of semi-crystalline samples were decomposed into individual peaks, belonging either to the amorphous or the crystalline phase with the Bruker-software TOPAS®. A big amorphous bump was always present at $2\theta = 20°$, crystalline peaks were found at various positions. The peaks of the two phases (amorphous and crystalline) were fitted with Pearson VII functions [15]. The relation of the peak position and breadth (FWHM) with the crystal size (l_c) is given by the Sherrer equation (Equation (3), parameter $k = 0.9$) [15]:

$$l_c = \frac{k \cdot \lambda}{B \cdot \cos\theta} \tag{3}$$

where B = FWHM (in radians); θ = half scattering angle; λ = wavelength of X-rays.

A custom built tensile device was used for uniaxial deformation using type ISO 527-2/1BB dumbbell test bars (20×2×1 mm) at a cross-head speed of 1 mm·min^{-1}. Heating was provided by a heating gun (heating rate ~10°C·min^{-1}, non-linear), whereby cooling was enabled by a cooled Nitrogen flux (Cooling rate ~10°C·min^{-1}, non-linear). The temperature was monitored by a thermocouple touching the sample. For *in situ* WAXS measurements, the test specimens were fixed in the custom build tensile device. The sample was deformed to 200% strain at T_{deform} after annealing at 75°C for 10 min, and then cooled down to 0°C and kept for 10 min, which was the same procedure as in SMCP. WAXS patterns were collected at each programming stage.

2.3.6. Small-angle X-ray scattering (SAXS)

SAXS was performed on a Bruker Nanostar diffractometer (Bruker AXS, Karlsruhe, Germany), operating 40 kV and 35 mA on a copper anode. Point focussed X-rays were monochromated and parallelized by Montel-optics and collimated by a 750/400/1000 µm 3-pinhole combination, thus a 400 µm beam having a wavelength of 0.15418 nm (CuKα) was obtained. The distance sample to the detector was 1070 mm calibrated with Silver behenate standard. A Vantec-2000 detector (2048×2048 pixel, 68 µm pixel size) was employed to record scattered intensities, the primary beam was stopped (6 mm lead beamstop) close before the detector. The primary and secondary beam paths as well as the sample chamber were operated under vacuum (~10^{-3} mbar). Samples were placed into a small powder-sample holder (0.2 mm thickness) and exposed 1 h to obtain a two dimensional scattering pattern which was corrected for spatial distortion and background subtracted (weighted with sample transmission). Isotropic scattering patterns were integrated (azimuthal average over 360°) by 5-point binning with a 0.001° (2θ) step size from $2\theta = 0.1$ to 3.2° leading into one-dimensional scattering curves of scattered intensity *vs*. scattering angle (I *vs*. 2θ). Anisotropic scattering patterns were integrated over a 10° wide azimuthal range along the axis of symmetry (fiber axis, s_3) Furthermore scattering angle was converted into scattering vector s, being $|s| = s = (2/\lambda)\sin\theta$ and a Kratky-plot (Lorenz correction Is^2 *vs*. s) was utilized to extract the long period L from the position of the peak maxima as $L = s^{-1}$ [16].

2.3.7. Toluene vapor treatment

The deformed specimens were treated in a vacuum desiccator which was first evacuated and then filled with saturated toluene vapor for 45 min. The lengths of deformed specimens after treatment, $l_{r,toluene}$, were recorded to calculate the partial recovery ratio in toluene, $R_{r,toluene}$, by Equation (4). After toluene vapor treatment, the sample was heated to 75°C to allow for complete recovery. The final recovery ratio after heating, $R_{r,heating}$, was calculated using the lengths of the sample after heating, $l_{r,heating}$ according to Equation (5). The content of toluene which was absorbed in the specimens was 8.0%, which was detected by GPC.

$$R_{r,touluene} = \frac{l_\varepsilon - l_{r,touluene}}{l_\varepsilon - l_0} \tag{4}$$

$$R_{r,heating} = \frac{l_\varepsilon - l_{r,heating}}{l_\varepsilon - l_0} \tag{5}$$

where l_0 is the original length of sample and l_ε is the deformed length of sample.

The content of toluene, which was absorbed in the vapor treated PCL-PIBMD test specimens, was quantified by chromatography experiments using the GPC equipment described in 2.3.1. A series of DMF/toluene mixtures with varying toluene concentration ranging from 0.02 to 10 wt% were analyzed with the GPC system for creation of a calibration curve. 0.1 g pieces were cut from the middle of the deformed specimens after toluene vapor treatment and then

dissolved in DMF resulting in a 0.2 wt% concentration and then investigated with the GPC system. The obtained toluene signal was evaluated by using the standard calibration curve.

3. Results and discussion

3.1. Thermal properties

The thermal properties of deformed PCL-PIBMD films were examined using DSC and compared to that obtained for a preconditioned non-deformed sample (see paragraph 2.3.3). As shown in Figure 1, only a PIBMD melting peak at 168°C can be observed in the non-deformed PIBMD sample. The reason might be that the existing PIBMD crystalline domains highly restricted the crystallization of PCL domains during the preconditioning procedure when cooled from 75 to 0°C with a cooling rate of 5°C·min^{-1}. Therefore, before deformation at 20 or 50°C, only PIBMD crystals existed in PCL-PIBMD, while all PCL domains were in the amorphous state. The PIBMD amorphous phase with a $T_{g,PIBMD} \approx 42$°C is in the glassy state at 20°C or in the rubbery state at 50°C. After deformation at 20 or 50°C, both PCL and PIBMD melting peaks were observed in the heating scan, demonstrating that the generation of oriented PCL chains during deformation facilitated the crystallization of PCL domains. A magnified view of the PCL melting peaks is shown in Figure 1b. A pronounced PCL melting peak in the range from 26 to 45°C with $\Delta H_{m,PCL} = 27$ J·g^{-1} was obtained for the sample deformed at 20°C, while deformation at 50°C resulted in a broad endothermic peak ranging from 27 to 54°C, having a slightly higher $\Delta H_{m,PCL}$ of 29 J·g^{-1}. The difference in the melting temperature interval indicates that PCL crystals with a higher crystal thickness exist only in samples deformed at 50°C. As shown in Table 1, the melting enthalpies of PCL domains in the sample deformed at 50°C were higher than the sample deformed at 20°C, suggesting a higher degree of crystallinity of PCL domains after deformation at a higher T_{deform}. The variation of T_{deform} did not significantly influence the melting enthalpy of the PIBMD crystals (27~29 J·g^{-1}). Compared to the non-deformed samples with a PIBMD melting enthalpy of 22 J·g^{-1}, it can be anticipated that strain-induced crystallization was responsible for the observed increase in crystallinity when the samples were deformed to 200%.

3.2. Surface morphologies

AFM experiments were performed to visualize the surface morphologies of PCL-PIBMD samples after deformation at various temperatures, as presented in Figure 2. Polymer crystals as typical spherulites,

Table 1. Thermal properties of deformed and non-deformed PCL-PIBMD solution cast films calculated from DSC measurements

T_{deform} [°C]	$T_{m,PCL}$ [°C]	$\Delta H_{m,PCL}$ [J·g^{-1}]	$T_{m,PIBMD}$ [°C]	$\Delta H_{m,PIBMD}$ [J·g^{-1}]
Non-programmed	–	–	168	22
20	40	21	168	27
50	41	29	170	29

Note: the estimated error for T is ±1°C, for ΔH is ±2 J·g^{-1}.

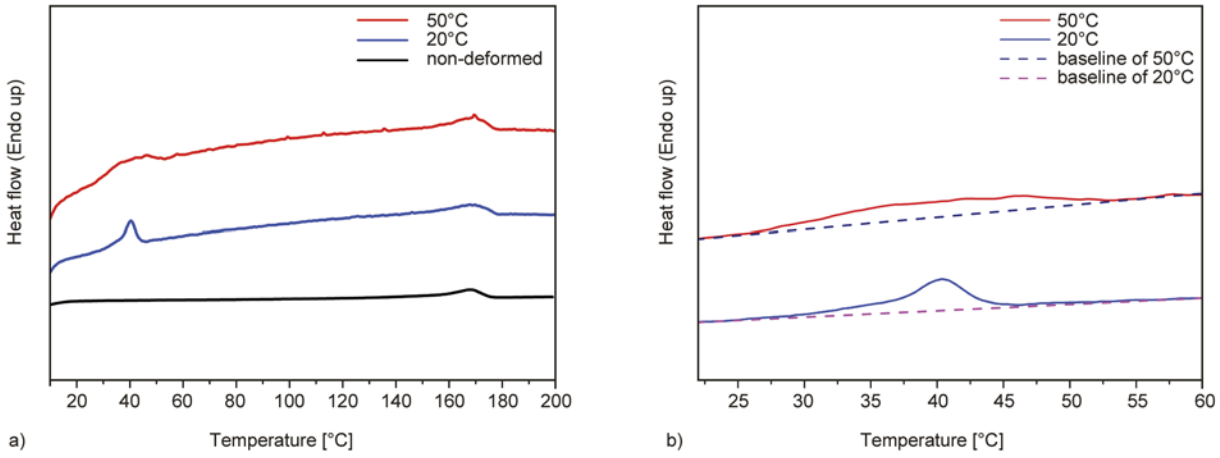

Figure 1. DSC heating curves of (a) deformed and non-deformed PCL-PIBMD solution cast films and (b) maginified view of PCL crystals melting peaks

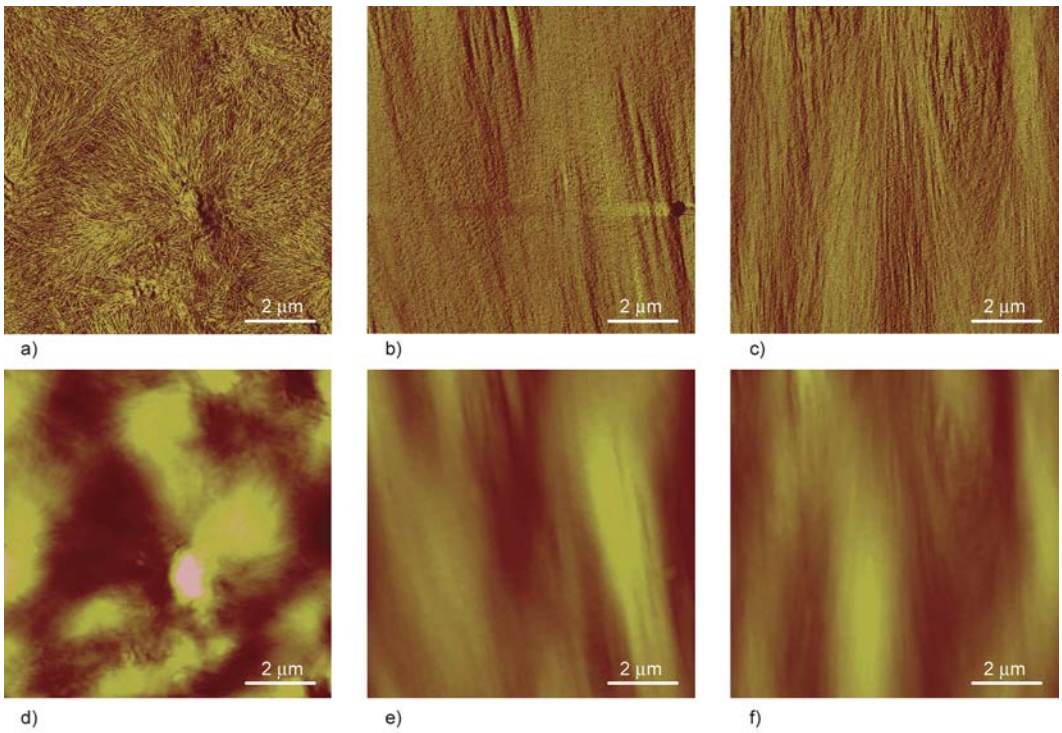

Figure 2. AFM phase images (a, b, c) and height images (d, e, f) of PCL-PIBMD films before (a, d) and after deformation to 200% strain at 50°C (b, e) and 20°C (c, f). The deformation direction was vertical

which are composed of highly ordered edge-on lamellae, were observed in the non-deformed sample as shown in Figures 2a and 2d. The large spherulites did not change evidently when increasing the temperature from 20 to 60°C (not presented here), indicating that those crystals originated from PIBMD domains. These results matched with the DSC data. It can also be observed that PIBMD crystals are enriched on the top surface of solution cast film. Further investigations with the spin coated PCL-PIBMD films (data not shown here) demonstrated that that PCL segments were preferentially enriched on the top layer in the molten state, indicating a smaller surface energy of PCL compared to PIBMD. The newly formed PIBMD crystals broke out the ordered phase separated morphology and fully wetted the free surface, while the crystallization of PCL domains was confined in the PIBMD lamellae, forming fractionated crystals. Thus, only large PIBMD spherulites can be observed on the topography of PCL-PIBMD films. More importantly, compared to the initial morphology without deformation, it can be illustrated from AFM phase images that the PIBMD spherulites were deformed along the deformation direction, as shown in Figures 2b–2c and 2e–2f. In addition, higher levels of structural orientations of PIBMD crystals can be observed if PCL-PIBMD film was deformed at 50°C.

3.3. Crystalline structures

For exploring the nanostructural changes during the deformation of PCL-PIBMD samples *in-situ* 2D WAXS patterns were recorded at different temperatures, which are displayed in Figure 3a. At 50°C, a strong reflection as an inner bright ring ($2\theta = 8.8°$) was identified with several other weak reflections as shown in Figures 3a (I and IV), all of which belong to the PIBMD crystals. Isotropic scattering indicated that randomly distributed PIBMD lamellae did not present evident orientation before deformation. With stretching to 200% at 50°C (Figure 3a II), an equatorial scattering maximum appeared at the inner ring ($2\theta = 8.8°$) of PIBMD crystal reflections as indicated by the arrow, illustrating the orientation of PIBMD crystals perpendicular to the deformation direction. The deformed sample was then cooled to 0°C (Figure 3a III) while the deformation was fixed. The ring of (110) reflection ($2\theta = 21.3°$) showed a strong equatorial scattering maximum, which suggested the generation of PCL crystals perpendicular to the deforming direction. For the sample deformed at 20°C (Figure 3a V), the equatorial (110) scattering maximum confirmed that the PCL crystals appeared only after stretching at 20°C (highlighted by an arrow). This indicates that the strain-induced crystallization of PCL domains

occurred during the stretching and the newly generated PCL crystals aligned perpendicular to the deformation direction. Usually, crystals generated by strain-induced crystallization exhibit highly ordered structures compared to that formed by thermal-induced crystallization during cooling. This conclusion could be confirmed by the DSC results, where a broad PCL melting peak was obtained for the sample deformed at 50°C and a smaller pronounced melting peak when programmed at 20°C.

No difference in the nanostructure was observed when the samples were further cooled to 0°C (Figure 3a VI). The size of PIBMD crystals ($l_{c,PIBMD}$) after deformation was calculated and shown in Table 2. Compared to the non-deformed sample, the size of PIBMD crystals decreased from 16.4 to 15.8~15.9 nm after deformation at 50 or 20°C. These results suggested that the fragmentation of PIBMD crystals occurred during deformation and its level was similar when PCL-PIBMD was deformed to 200% at 50 or 20°C.

For quantification of the resulting degree of orientation of the crystalline structures, the corresponding azimuthal scans of the WAXS patterns were analyzed. Here, the intensity distribution of the ring (110) ($2\theta = 21.3°$) from the PCL crystal reflections were explored at each deformation stage as shown in Figure 3c and 3d, which was corresponding to the SMCP. The full width at half maximum (FWHM) of crystal structures were listed in Table 2. Before deformation, no peaks can be found in the profiles, indicating that no PCL crystals existed in the non-deformed samples. In the azimuthal profiles obtained after deformation at 50°C also no PCL crystals are present, while after cooling to 0°C a pronounced increase in orientation was obtained ($FWHM_{PCL}$ = 25.7°) caused by newly generated PCL crystals. In contrast, the azimuthal profiles of the sample

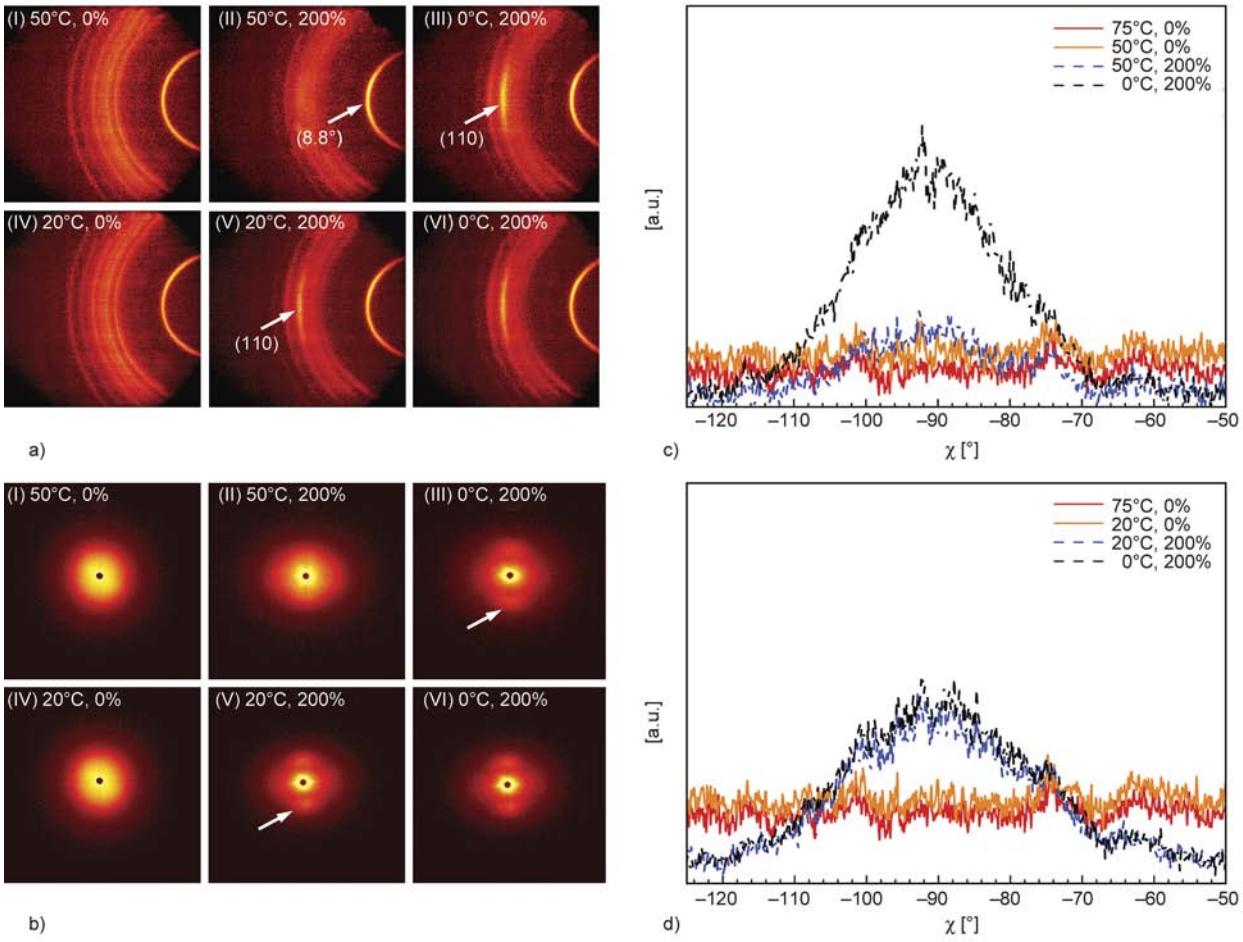

Figure 3. WAXS (a) and SAXS (b) patterns of PCL-PIBMD films (I, IV) before and (II, V) after deformation to 200% strain at (I, II) 50°C and (IV, V) 20°C and cooled to (III, VI) 0°C, respectively. Intensity distribution of (a) the ring (110) ($2\theta = 21.3°$) from PCL crystal reflections from WAXS patterns when samples were deformed at (c) 20°C and (d) 50°C. The deformation direction was vertical

deformed at 20°C ($FWHM_{PCL}$ = 33.3°) and fixed at 0°C ($FWHM_{PCL}$ = 32.3°), were found to be almost identical (see Figure 3c), indicating that a lower degree of orientation of PCL crystals is achieved by deformation at 20°C. In addition, the azimuthal analysis of the PIBMD crystal structure was performed (Figure 3d). Here a higher degree of orientation could be obtained when the samples were deformed at 50°C compared to the deformation at 20°C. This result is in good agreement with the interpretation of the AFM analysis.

During programming at 50°C the overall applied deformation can be solely fixed by the PIBMD crystals existing at 50°C, whereby the oriented amorphous PCL domains can crystallize in the subsequent cooling to 0°C. On the contrary, a difference is given when deforming the multiblock copolymer at 20°C. Here the PCL domains form strain-induced crystals during the deformation process. Thus, the deformability of the amorphous PCL domains would be additionally restricted by newly formed PCL crystals and glassy PIBMD domains. Therefore, a decrease in degree of orientation of PCL and PIBMD chains represented by lower FWHM values is caused. As the PCL domains exhibit a low glass transition temperature around –60°C, it can be assumed that the relaxation of the rubbery PCL chains at 20 or 50°C is almost similar, but that the chain deformability (which is higher at 50°C) is predominantly controlling the achievable degree of orientation after programming.

The changes in the lamellar structure during deformation can be extracted directly from the *in-situ* 2D SAXS patterns. As shown in Figures 3b (I and IV), before deformation, the SAXS patterns exhibited single isotropic scattering related to the stacks of randomly oriented chain-folded PIBMD lamellae at 50°C, suggesting that no preferred orientation existed in non-deformed samples. After deformation up to a strain of 200% at 50°C (Figure 3b II), the pattern became oblate, indicating the scattering maximum along the meridional direction (parallel to deformation direction) shifted to a lower angle, whereas the scattering maximum in equatorial direction (vertical to deformation direction) moved to a higher value. Followed by deforming at 50°C, samples were cooled to 0°C to fix the temporary shape (Figure 3b III). Two scattering maxima appeared in meridian, suggesting the generation of PCL crystalline lamellae during cooling, which were oriented perpendicular to the deformation direction. For the PCL-PIBMD sample stretched at 20°C to 200% (Figure 3b V), two strong scattering maxima were clearly visible along the meridional direction, which further prove that the strain-induced PCL crystals were vertical to the deformation direction during stretching. After fixing the temporary shape at 0°C (Figure 3b VI), no evident changes can be observed compared to the deformed sample at 20°C. The shift of the scattering maximum in SAXS patterns was related to the changes in the long period (L), which are summarized in Table 2. The long period in meridional direction (L_{mer}) increased from 13.3 to 13.5 nm while the long period in equator (L_{equ}) was reduced from 13.3 to 10.5 nm after deformation to 200% at 50°C. It can be considered that the deformation enlarged the average spacing between the lamellae aligned perpendicularly to the deformation direction leading to the increase in L_{mer}, while the space between the lamellae which are parallel to the deformation direction decreased. After cooling to 0°C, the reductions in both L_{mer} and L_{equ} were observed. The reason could be the generation of small PCL crystals among the PIBMD lamellae. When the sample was deformed at 20°C, the L_{equ} decreased to 9.9 nm, while L_{mer} turned to 11.1 nm. The reduction in both L_{mer} and L_{equ} at 20°C suggested that the crystal structures generated during stretching resulted from strain-induced crystallization of PCL domains. Only a slight difference can be observed when the sample was cooled

Table 2. Thermal properties and crystal structures obtained or calculated from DSC, WAXS and SAXS measurements

T_{deform} [°C]	T [°C]	L_{equ} [nm]	L_{mer} [nm]	$l_{c,PIBMD}$ [nm]	$FWHM_{PIBMD}$ [°]	$FWHM_{PCL}$ [°]
Non-programmed	20	13.0	13.0	16.4	–	–
Non-programmed	50	13.3	13.3	16.4	–	–
50	50	10.5	13.5	15.8	64.3	–
50	0	9.0	12.8	15.9	62.9	25.7
20	20	9.9	11.1	15.9	85.8	33.3
20	0	8.9	10.9	15.8	84.3	32.3

Note: L_{equ} and L_{mer} were calculated from SAXS results and $l_{c,PIBMD}$ was calculated from WAXS data. The estimated error for L and l_c are ±0.2 nm and for FWHM is 0.7°.

down to 0°C after deformation since T_{deform} was already lower than $T_{g,PIBMD}$ and $T_{m,PCL}$. The SAXS results fully agreed with the WAXS results.

3.4. Shape-memory properties

The shape-memory properties of solution cast PCL-PIBMD films performed at two T_{deform}s were measured by cyclic, thermomechnical tensile tests. The stress-temperature-strain curves of the first cycle are shown in Figure 4. In SMCP, the PCL-PIBMD specimens were stretched to a strain of ε_m of 200% at a deformation rate of 1 mm·min^{-1}. The T_{deform}s were chosen as 50 and 20°C, respectively, which was above or below both $T_{m,PCL}$ and $T_{g,PIBMD}$. The deformed shapes were fixed when the temperature was decreased to T_{low} of 0°C. Finally, by heating the samples to 75°C under stress-free or constant-strain conditions the recovery was initiated.

Table 3 lists the shape-memory properties determined for the PCL-PIBMD samples programmed at different T_{deform}s. Excellent values for R_f above 92% as well as R_r around 90% in the first cycle and $R_r \approx 99\%$ in the 2nd and 3rd cycle were reached for both samples. The T_{sw} decreased from 44 to around 39°C as well as the temperature where the maximum recovery force occurred ($T_{\sigma,max}$) was reduced from 56 to 30°C when T_{deform} was reduced from 50 to 20°C. This effect could be caused by the different structures of PCL crystals, as demonstrated by DSC curves, and different degree of orientation of PIBMD domains, as shown in AFM images. In addition, a higher stress $\sigma(\varepsilon_m)$ was required to achieve the same strain at 20°C since the PIBMD amorphous phase was in glassy state. In addition, the ratio of $\sigma_{max}/\sigma(\varepsilon_m)$ decreased largely from 60.0 to 38.2% when decreasing the T_{deform} from 50 to 20°C, suggesting that more energy was dissipated during stretching for the slippage and the fragmentation of PIBMD lamellae.

3.5. Toluene vapor treatment

As demonstrated before [7], in case of PCL-PIBMD, both PIBMD amorphous phase and PCL crystalline phase can act as switching domains since they present a similar T_{trans}. Therefore, the temporary shape of deformed samples can be fixed by the crystallization of PCL domains and the vitrification of amorphous PIBMD phase. Since toluene is a good solvent for PCL but a poor solvent for PIBMD, it can be used to trigger the partial recovery of deformed specimens by selectively eliminating PCL crystals by the solvatisation of PCL segments. In addition, since PIBMD amorphous phases still stayed in the glassy state at room temperature after the treatment with toluene vapor (determined by DMTA, not shown here), the temporary shape which is fixed by vitrification of PIBMD amorphous phase cannot recover

Table 3. Shape-memory properties for PCL-PIBMD films programmed to 200% at 50 and 20°C, respectively, with the strain rate of 1 mm·min^{-1}

T_{deform} [°C]	$R_{f(1)}$ [%]	$R_{r(1)}$ [%]	$R_{f(2,3)}$ [%]	$R_{r(2,3)}$ [%]	T_{sw} [°C]	$\sigma(\varepsilon_m)$ [MPa]	σ_{max} [MPa]	$\sigma_{max}/\sigma(\varepsilon_m)$ [%]	$T_{\sigma,max}$ [°C]
50	96	90	96	99	44	12.4	7.4	60.0	56
20	94	90	92	99	39	25.1	9.6	38.2	30

Note: The $R_{f(1)}$, $R_{r(1)}$, T_{sw}, were determined from the 1st cycle measurement under stress-free recovery; $R_{f(2,3)}$ and $R_{r(2,3)}$ were the average values of the 2nd and 3rd cycle measurement under stress-free recovery; $\sigma(\varepsilon_m)$, σ_{max}, $\sigma_{max}/\sigma(\varepsilon_m)$ and $T_{\sigma,max}$ were determined from the 1st cycle measurement under constant-strain recovery. $R_{r,toluene}$ was measured using a centimeter ruler. The estimated errors for R_f and R_r is ±2%, for T is ±2°C, for σ is ±0.5 MPa and for $R_{r,toluene}$ is ±4%.

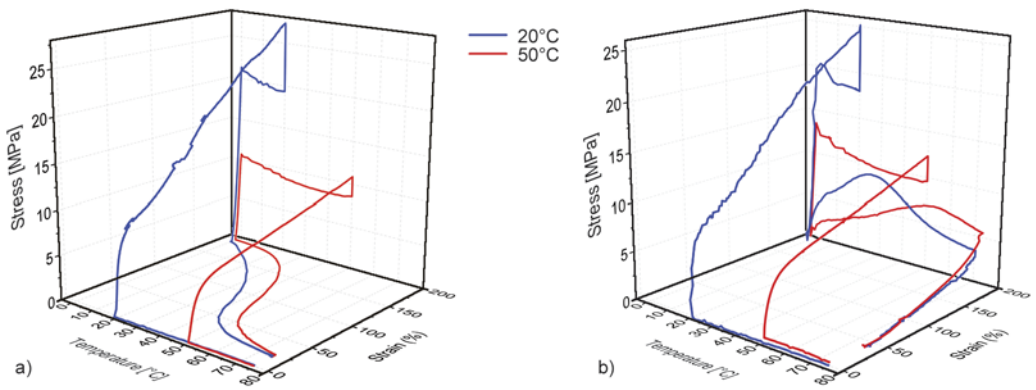

Figure 4. The first cycle curves of cyclic tests of PCL-PIBMD films programmed to 200% at 50 and 20°C, respectively, with the strain rate of 1 mm·min^{-1} and recovered under (a) stress-free and (b) constant-strain conditions

considerably. Thus, after placing the deformed specimens in toluene vapor for 45 min at room temperature, the contributions of $T_{g,PIBMD}$ and $T_{m,PCL}$ to the SME switching domains can be distinguished. Figure 5 presents the photographic pictures of deformed samples before and after toluene vapor treatment and after reheating to 75°C in comparison to a non-deformed sample. It can be observed that the lengths of deformed specimens decreased after 45 min, indicating a partial recovery. DSC measurements were performed to examine the thermal properties of treated samples (not shown here). After toluene vapor treatment, the melting peaks of PCL domains disappeared, suggesting that the PCL crystals were dissolved by vapor toluene. The orientated PCL chains which were fixed by PCL crystals, thus fully recovered driven by increasing the entropy. The PIBMD crystals, however, did not vary considerably during the treatment, demonstrating that (1) the netpoints, or the ability to keep the permanent shape of PCL-PIBMD samples, were not influenced by toluene, and more importantly, (2) the variation in PIBMD amorphous phase could be neglected. Then these samples after the treatment in toluene vapor were reheated to 75°C, where the orientated chains fixed by vitrification of PIBMD domains were allowed to recover. A second recovery process can be observed and the lengths of deformed samples further reduced. As declared in Table 4, the total recovery ratios after heating, $R_{r,heating}$, for samples deformed at 50 and 20°C were comparable with the recovery ratios measured from cyclic, thermomechanical tensile tests. Therefore, the recovery ratio after toluene vapor treatment ($R_{r,toluene}$) can be considered as the absolute recovery ratio resulting from PCL crystals as the switching domains, while the ratio of $R_{r,toluene}/R_{r,heating}$ can be defined as the relative contribution of PCL crystals to the total recovery of deformed PCL-PIBMD specimens. Table 4 shows that the $R_{r,toluene}$ value of samples deformed at 20°C was larger than that deformed at 50°C, while the $R_{r,toluene}/R_{r,heating}$ increased from 82.9 to 96.7% when T_{deform} changed from 50 to 20°C. These results indicated that the temporary shape of the samples deformed at 20°C was almost totally fixed by the strain-induced crystallization of PCL domains. Based on all the obtained data and results, the mechanisms of structural variations of PCL-PIBMD specimens programmed to 200% strain at 50 and 20°C are discussed in the following. In the semi-crystalline MBC of PCL-PIBMD, PCL amorphous domains, PIBMD amorphous domains, and PIBMD crystalline domains existed before deformation. The uniaxial deformation at 50°C first resulted in the orientation of PIBMD and PCL amorphous phases. With increasing the strain, the stress was transferred from orientated amorphous chains to PIBMD crystals, leading to their fragmentation.

Table 4. The recovery ratio after toluene vapor treatment and heating procedure for PCL-PIBMD films programmed to 200% at 50 and 20°C, respectively, with the strain rate of 1 mm·min^{-1}

T_{deform} [°C]	$R_{r,toluene}$ [%]	$R_{r,heating}$ [%]	$R_{r,toluene}/R_{r,heating}$ [%]
50	73	88	82.9
20	87	90	96.7

Note: $R_{r,toluene}$ and $R_{r,heating}$ were measured using a centimeter ruler after toluene vapor treatment and heating to 75°C, respectively. The estimated errors for $R_{r,toluene}$ and $R_{r,heating}$ are ±2%.

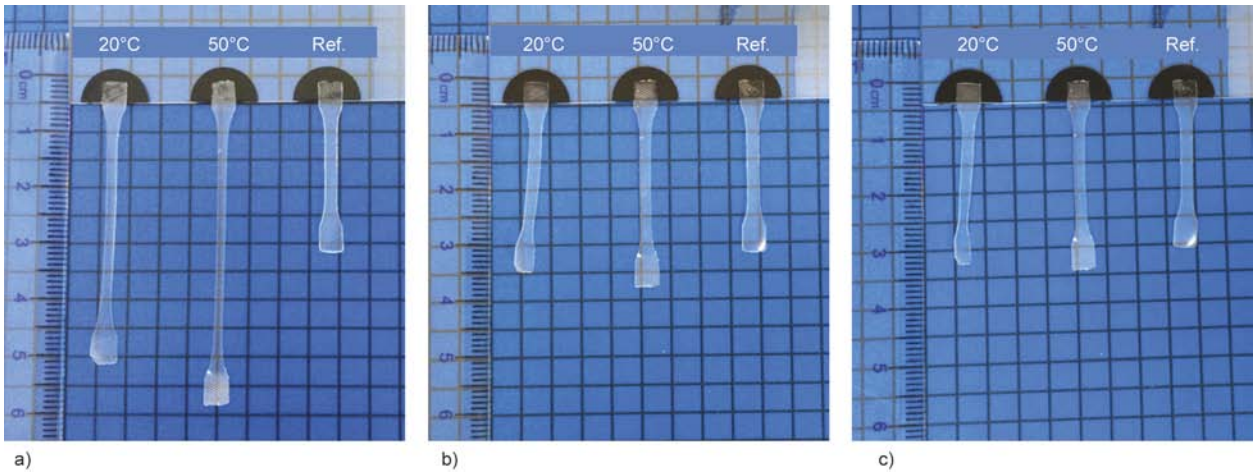

Figure 5. Photos of deformed PCL-PIBMD samples (a) after deformation, (b) after toluene vapor treatment and (c) after heating to 75°C in comparison to a non-deformed sample as a reference. For the deformed films, the strain was 200% with the strain rate of 1 mm·min^{-1} and the deformation temperatures were 50 and 20°C, respectively.

At 50°C, strain-induced crystallization of PCL domains was negligible, since the temperature was higher than $T_{m,PCL}$. Only thermally-induced crystallization of PCL domains occurred during the subsequent cooling process, in which the entangled polymer chains preferred to form crystals with chain-folded conformation. However, at 20°C uniform chain-extended crystal structures were generated because of strain-induced crystallization. A lower $T_{m,PCL}$ and its narrower range, thus, were achieved, correspondingly decreasing T_{sw} and $T_{\sigma,max}$. The amorphous PIBMD phase stayed in rubbery or glassy state at 50 or 20°C, respectively. When the sample was deformed at 50°C, both PCL and PIBMD amorphous phases can be oriented. After cooling down the temperature to 0°C, the oriented PIBMD amorphous phase was fixed by its vitrification. Therefore, both PCL crystals and PIBMD amorphous phase can contribute to the fixation of the temporary shape.

When the PCL-PIBMD samples were programmed at 20°C, however, the PIBMD amorphous phase was in the glassy state. Therefore, the chain orientation was mainly restricted to PCL amorphous phase and the temporary shape was fixed mainly by the crystallization of PCL domains. For the same reason, a higher stress was required for deforming the sample and more energy dissipation was observed during stretching, generating the larger $\sigma(\varepsilon_m)$ but smaller $\sigma_{max}/\sigma(\varepsilon_m)$ at 20°C.

5. Conclusions

In PCL-PIBMD MBCs, the amorphous PIBMD domains and crystallizable PCL domains can serve as switching domains, while the PIBMD crystals act as physical netpoints determining the permanent shape. The structural evolution of PCL-PIBMD samples during deformation depended on the deformation temperature and resulted in different contributions of PCL crystals and amorphous PIBMD domains to the switching domains. When the samples were deformed at 50°C, which was above $T_{m,PCL}$ and $T_{g,PIBMD}$, both PCL and PIBMD amorphous domains were oriented. The temporary shape of deformed PCL-PIBMD, thus, was fixed by the thermally-induced chain-folded PCL crystals and vitrification of PIBMD domains, leading to their joint contribution to switching domains. However, when the samples were deformed at 20°C, which is below $T_{m,PCL}$ and $T_{g,PIBMD}$, only PCL crystallizable domains acted as switching domains by strain-induced crystallization, since PIBMD amorphous phase was in the glassy state. In such a case a higher programming stress is required and more energy dissipation occurred during deformation when compared to T_{deform} = 50°C. Here we could demonstrate that the results achieved by a combination of structural and thermo-mechanical investigations are useful for understanding of complicated SME mechanisms in MBCs containing two crystallizable segments. More importantly, this work offers a new method to clarify and adjust the relative contribution of crystalline and amorphous switching domains with overlapping or almost identical transition temperature ranges in such MBC.

References

[1] Behl M., Razzaq M. Y., Lendlein A.: Multifunctional shape-memory polymers. Advanced Materials, **22**, 3388–3410 (2010).
DOI: 10.1002/adma.200904447

[2] Xie T.: Recent advances in polymer shape memory. Polymer, **52**, 4985–5000 (2011).
DOI: 10.1016/j.polymer.2011.08.003

[3] Karger-Kocsis J., Kéki S.: Biodegradable polyester-based shape memory polymers: Concepts of (supra) molecular architecturing. Express Polymer Letters, **8**, 397–412 (2014).
DOI: 10.3144/expresspolymlett.2014.44

[4] Kolesov I. S., Radusch H-J.: Multiple shape-memory behavior and thermal-mechanical properties of peroxide cross-linked blends of linear and short-chain branched polyethylenes. Express Polymer Letters, **2**, 461–473 (2008).
DOI: 10.3144/expresspolymlett.2008.56

[5] Kang S. M., Lee S. J., Kim B. K.: Shape memory polyurethane foams. Express Polymer Letters, **6**, 63–69 (2012).
DOI: 10.3144/expresspolymlett.2012.7

[6] Feng Y., Guo J.: Biodegradable polydepsipeptides. International Journal of Molecular Sciences, **10**, 589–615 (2009).
DOI: 10.3390/ijms10020589

[7] Feng Y., Behl M., Kelch S., Lendlein A.: Biodegradable multiblock copolymers based on oligodepsipeptides with shape-memory properties. Macromolecular Bioscience, **9**, 45–54 (2009).
DOI: 10.1002/mabi.200800199

[8] Feng Y., Lu J., Behl M., Lendlein A.: Degradable depsipeptide-based multiblock copolymers with polyester or polyetherester segments. The International Journal of Artificial Organs, **34**, 103–109 (2011).
DOI: 10.5301/IJAO.2011.6402

[9] Bao R., Ding Z., Zhong G., Yang W., Xie B., Yang M.: Deformation-induced morphology evolution during uniaxial stretching of isotactic polypropylene: Effect of temperature. Colloid and Polymer Science, **290**, 261–274 (2012).
DOI: 10.1007/s00396-011-2550-5

[10] Jiang Z., Tang Y., Men Y., Enderle H-F., Lilge D., Roth S. V., Gehrke R., Rieger J.: Structural evolution of tensile-deformed high-density polyethylene during annealing: Scanning synchrotron small-angle X-ray scattering study. Macromolecules, **40**, 7263–7269 (2007).
DOI: 10.1021/ma0627572

[11] Sarva S. S., Hsieh A. J.: The effect of microstructure on the rate-dependent stress–strain behavior of poly(urethane urea) elastomers. Polymer, **50**, 3007–3015 (2009).
DOI: 10.1016/j.polymer.2009.04.025

[12] Hu J. L., Ji F. L., Wong Y. W.: Dependency of the shape memory properties of a polyurethane upon thermomechanical cyclic conditions. Polymer International, **54**, 600–605 (2005).
DOI: 10.1002/pi.1745

[13] McClung A. J., Tandon G. P., Baur J. W.: Strain rate- and temperature-dependent tensile properties of an epoxy-based, thermosetting, shape memory polymer (Veriflex-E). Mechanics of Time-Dependent Materials, **16**, 205–221 (2012).
DOI: 10.1007/s11043-011-9148-7

[14] Azra C., Plummer C. J. G., Månson J-A. E.: Isothermal recovery rates in shape memory polyurethanes. Smart Materials and Structures, **20**, 082002/1–082002/10 (2011).
DOI: 10.1088/0964-1726/20/8/082002

[15] Scherrer P.: Bestimmung der inneren Struktur und der Größe von Kolloidteilchen mittels Röntgenstrahlen. in 'Kolloidchemie Ein Lehrbuch' (Ed.: Zsigmondy R.) Springer, Berlin, 387–409 (1912).
DOI: 10.1007/978-3-662-33915-2_7

[16] Stribeck N.: X-ray scattering of soft matter. Springer, Berlin (2007).

eXPRESS Polymer Letters Vol.9, No.7 (2015) 636–646
Available online at www.expresspolymlett.com
DOI: 10.3144/expresspolymlett.2015.59

Synthesis and thermotropic behavior of side chain polysiloxane bearing triphenylene moiety

T. Makowski[1*], *T. Ganicz*[1], *W. Zajaczkowski*[2], *W. Pisula*[2], *W. A. Stanczyk*[1], *A. Tracz*[1]

[1]Centre of Molecular and Macromolecular Studies, Polish Academy of Science, Sienkiewicza 112, 90-363 Lodz, Poland
[2]Max Planck Institute for Polymer Research, Ackermannweg 10, 55128 Mainz, Germany

Received 19 November 2014; accepted in revised form 31 January 2015

Abstract. Side chain discotic polysiloxane with 2,3,6,7-tetrakis(hexyloxy)-10-methoxytriphenylene-11-undecanoate moieties is synthesized by hydrosilylation reaction. The phase behavior and thermooptical properties of the polysiloxane and the side chain precursor 2,3,6,7-tetrakis(hexyloxy)-10-methoxytriphenylene-11-undecanoate are examined by polarizing optical microscopy, thermooptical analysis, differential scanning calorimetry and wide angle X-ray scattering studies. A columnar planar alignment of LC in the layers has been determined. The pronounced alignment makes this polymer a promising material for application in optoelectronic devices. The differences in phase transitions and morphology between the triphenylene precursor and the discotic polysiloxane are discussed.

Keywords: *thermal properties, discotic polysiloxane, atomic force microscope, polymer synthesis*

1. Introduction

There has been an increasing interest in columnar discotics which involve π-conjugated systems [1–3]. They have been extensively studied as a result of their electro-optical and semiconducting properties as well as expected applications in organic field effect transistor devices (OFET) and solar cells [4–6]. They can undergo an easy macroscopic alignment and can be processed in a simple way [7–9]. Moreover, structural defects can be self-healed because of molecular fluctuations [10]. Flat, conjugated or fused discotic molecules possess unique features, making them important, potential material for one-dimensional charge carrier systems [11]. They are able to self-assemble into long-range 1D columnar arrays that can display liquid crystalline properties [12, 13]. Discotic liquid crystals based on the triphenylene derivatives are particularly attractive as their chemistry is relatively accessible [14]. Semiconducting properties of low molecular triphenylenes have been already extensively studied and well proven [15–17].

On the other hand, liquid crystalline polymers, especially the ones incorporating calamitic moieties, belong to systems of wide interest. They combine the unique features of low molecular weight liquid crystals with increased thermal and mechanical stability of the mesophase and the possibility of macroscopic alignment, allowing to study the self-organization of the discotic mesogens, in order to investigate the oriented macroscopic structures [18]. Side chain polymers based on discotic mesogens have been much less explored and it concerns in particular systems based on flexible, linear polysiloxanes with triphenylene moieties. Only a limited number of star shaped oligomers [12, 19, 20] and side chain systems [21–23] has been explored so far, although these polymers may also have an increased tendency to form columnar mesophases which might help to obtain thin layers with high molecular order.

*Corresponding author, e-mail: tomekmak@cbmm.lodz.pl

In general, the attachment of a mesogenic structure to the flexible siloxane chain via a spacer maintains the liquid crystalline properties, but considerably reduces the transition temperatures with respect to the low molecular weight analogues [24]. Moreover, it was already proven that such polymers have a tendency to lower the crystal-mesophase temperature transition of discotic and calamitic mesophases [23]. In the past, preparation of side chain polysiloxanes with tripenylene mesogens involved complicated and low yield synthetic pathways. It refers in particular to synthesis of mono-substituted functionalized triphenylenes [22].

In this work, we present a simplified synthetic approach to an asymmetrically substituted triphenylene, functionalized with terminally unsaturated alkene moiety and the relevant side chain polysiloxane followed by phase transition studies of these novel systems.

2. Experimental section

2.1. Materials and methods

2.1.1. Reagents

Organometallic syntheses were carried out under argon with the exclusion of moisture. 1,2-dihexyloxybenzene, guiacol, anhydrous $FeCl_3$, dicyclohexylcarbodiimide (DCC), N-N-dimethylaminopirydyne (DMAP), undecenoic acid all Aldrich Poland, poly (methylhydrosiloxane), 30cSt (an average molecular weight of 2100 g·mol^{-1}. (ABCR Germany), H_2SO_4 conc. 98%, ethanol 98%, CH_2Cl_2, THF all POCh Poland, were used as supplied. Toluene (POCh Poland), used for hydrosilylation reaction, was dried by standard methods and stored over a sodium mirror [25]. Toluene, CH2Cl2, THF and hexane (Aldrich/Fluka Poland, HPLC grade) used for column chromatography were used as supplied.

2.1.2. Spectroscopy

The ^{1}H-, ^{13}C- and ^{29}Si-NMR spectra were recorded in $CDCl_3$ or toluene solutions with a Bruker AC 200 or a Bruker DRX 500 spectrometers. IR spectra were obtained with an ATI Mattson spectrometer for polymer solutions in sodium dried toluene.

2.1.3. Molecular weight measurement

Molecular weights were measured by gel-permeation chromatography (GPC) using a Waters system with Wyatt/Optilab 902 Interferometric Refractometer, analyses were performed on an LDC Analytical refracto Monitor IV instrument working with an RI detector and equipped with two SDV columns of the following parameters: 8×300 mm, 5 μm particle size, with 10^4 and 100 Å pore size. Toluene was used as an eluent at a flow rate of 0.7 mL/min. Molecular masses were calculated relative to polystyrene standards.

2.1.4. Thermooptical analysis (TOA)

Changes of the transmission of polarized light as a function of temperature were recorded and visualized using an author's software TOAPLOTS. Simultaneously the morphology of thin layers was observed under optical microscope. Morphology of samples was studied using Nikon Eclipse E400 Pol microscope equipped with polarizing filters and an analog SANYO VCC-3770P camera. The images were acquired using Leadtek TV Tuner WinFast PVR2. Heating and cooling of the samples at a controlled rate was accomplished using Mettler FP82 hot stage equipped with an FP90 controller and a photo detector.

2.1.5. Differential scanning calorimetry (DSC)

Differential scanning calorimetry (DSC) studies were performed using TA Instruments Q20 and DuPont DSC-910, calibrated with an indium standard at a rate of 5°C/min under nitrogen flow.

2.1.6. Atomic force microscopy (AFM)

Atomic force microscopy (AFM) images were recorded under ambient atmosphere, at room temperature using Nanoscope IIIa, MultiMode (Veeco, Santa Barbara, CA) microscope. The probes were commercially available rectangular silicon cantilevers (RTESP from Veeco) with nominal radius of curvature in the 10 nm range spring constant 20–80 N/m, a resonance frequency lying in the 264–369 kHz. The images were recorded with the highest available sampling resolution, that is, 512×512 data points.

2.1.7. 2D-WAXS

The 2D wide angle X-ray scattering (2D-WAXS) measurements were performed by means of a solid anode X-ray tube (Siemens Kristalloflex X-ray source, copper anode X-ray tube operated at 35 kV and 40 mA), Osmic confocal MaxFlux optics, X-ray beam with pinhole collimation and a MAR345 image plate detector. The samples were prepared as a thin

filament of 0.7 mm in diameter via filament extrusion in their LC phase. For the measurements, the samples were positioned perpendicular to the incident X-ray beam and scattering intensity was detected on a 2D image plate (MAR345) with a pixel size of 100 μm (3450×3450 pixels). Data analysis was performed using the Datasqueeze 3.0.0 software.

2.2. Synthesis

Synthesis of 2,3,6,7-tetra(hexyloxy)-10-methoxy-11-hydroxy triphenylene (3) (Figure 1)

Functionalized triphenylenes (3) and (4) were prepared similar to the reported method [26].

40 g (0.144 mol) of 1,2-dihexyloxybenzene (1) and 35.75 g (0.288 mol) of guiacol (2) were dissolved in 350 mL. of concentrated aqueous H_2SO_4 (70%) in a 3 neck 2 L flask, equipped with an ice bath and mechanical stirrer and the reaction mixture was cooled down to –13°C. 93.4 g (0.576 mol) of anhydrous $FeCl_3$ was slowly added at suitable rate, allowing to keep the temperature in the flask below –10°C (2.5 hrs.). After addition of $FeCl_3$ the reaction mixture was stirred at room temperature for additional 5 hrs. Then 500 g of crushed ice was added and the reaction was stirred until ice melted completely. The crude product – dark green precipitate was filtered, washed three times with 200 mL of water, twice with 100 mL of ethanol and dried. The product was dissolved in 100 mL of CH_2Cl_2, precipitated again in 100 mL of ethanol, filtered and dried. The violet product was purified by fractional column chromatography (1 m, silica gel 40 A, eluents: hexane/THF 1:1 v/v), dried in vacuum (60°C, 2 hrs), leaving 10.5 g of (3) (yield: 16%).

^{1}H NMR: (200 MHz, $CDCl_3$, δ) 0.85–0.95 (m, 12H, C**H**$_3$–$(CH_2)_5$O), 1.31–1.45 (m, 16H, $CH_3(CH_2)_2(CH_2)_3$O), 1.45–1.60 (m, 8H, $CH_3(CH_2)_2CH_2(CH_2)_2$ O), 1.80–1.98 (m, 8H, $CH_3(CH_2)_3CH_2CH_2$O), 3.92 (s, 3H, OCH_3), 4.19–4.31 (m, 8H, $CH_3(CH_2)_4CH_2$O, 5.79–5.93 (s, 1H, OH), 6.87 (d, 2H, aromatic protons in OH and OCH_3 substituted ring), 7.81–7.89 (m, 4H, aromatic in hexyloxy substituted rings), ^{13}C NMR: (200 MHz, standard proton decoupling, $CDCl_3$, δ) 14.1 (CH_3), 22.6 (CH_3CH_2), 26.1 ($CH_3CH_2CH_2$), 29.3 ($CH_3(CH_2)_2CH_2$), 31.4 ($CH_3(CH_2)_3CH_2$), 55.3 (OCH_3), 68.9 (OCH_2), 104.6, 104.8, 104.9, 105.1 (aromatic carbons from hexyloxy substituted rings), 112.1, 112.2 (aromatic carbons from methoxy/hydroxyl substituted rings), anal. calcd for $C_{43}H_{62}O_6$: C 76.22, H 9.26; found: C 75.93, H 9.16

Synthesis of 2,3,6,7-tetrakis(hexyloxy)-10-methoxytriphenylene-11-undecenoate (4) (Figure 1)

10 g (0.015 mol) of (3), 2.7 g (0.015 mol) of 10-undecenoic acid, 3 g (0.022 mol) of DCC (dicyclohexylcarbodiimide) and 0.18 g of N,N-dimethylaminopyridine (DMAP) were dissolved in 150 ml of CH_2Cl_2 and stirred at room temperature for 48 hrs. The reaction mixture was filtered and the precipitate was washed twice with 50 mL of CH_2Cl_2. The solvent was evaporated leaving white, crystalline product, which was purified by fractional column chromatography (1 m, silica gel 40 A, eluents: CH_2Cl_2/toluene 1:2 v/v) (yield: 3.7 g, 30%). ^{1}H NMR: (200 MHz, C_6D_6, δ) 0.75–0.97 (m, 12H, C**H**$_3$–$(CH_2)_5$O), 1.20–1.32 (m, 26H, $CH_3(CH_2)_2(CH_2)_3$O + CH=CH($CH_2)_5(CH_2)_3$COO), 1.35–1.58 (m, 8H, $CH_3(CH_2)_2CH_2(CH_2)_2$ O), 1.72–2.14 (m, 8H, $CH_3(CH_2)_3CH_2CH_2$O), 2.32–2.46 (m, 2H, CH=CH$(CH_2)_6CH_2CH_2$COO), 2.51–2.74 (m, 2H, CH=CH$(CH_2)_7CH_2$COO), 3.93 (s, 3H, OCH_3), 4.13–4.30 (m, 8H, $CH_3(CH_2)_4CH_2$O, 4.81–5.06 (m, 2H, C**H**$_2$=CH–), 5.71–5.99 (m, 1H, CH_2=C**H**–), 7.31 (s, 1H, aromatic from undecenoic ester substituted ring), 7.77–7.88 (m, 4H, aromatic from hexyloxy substituted rings), 8.09 (s, 1H, aromatic from methoxy substituted ring), ^{13}C NMR: (200 MHz, standard proton decoupling, C_6D_6, δ) 14.3 (CH_3), 23.1 (CH_3CH_2), 26.3 ($CH_3CH_2CH_2$), 29.0 (CH_2=CHCH_2CH_2), 29.1 (CH_2=CH$(CH_2)_2CH_2$), 29.6 (CH_2=CH$(CH_2)_3CH_2$), 29.8 (CH_2=CH$(CH_2)_4CH_2$), 30.8 ($CH_3(CH_2)_2CH_2$), 30.9 ($CH_3(CH_2)_3CH_2$), 31.1 (CH_2=CH$(CH_2)_5CH_2$), 32.6 (CH_2=CH$(CH_2)_6CH_2$), 33.7 (CH_2=CHCH_2), 33.8 (O(O)CCH_2), 55.9 (OCH_3), 69.1 (OCH_2), 103.8, 103.9, 104.1, 104.11 (aromatic carbons from hexyloxy substituted rings), 111.1, 111.2 (aromatic carbons from methoxy/undecenoic ester substituted ring), 114.6 (CH_2=CH), 139.8 (CH_2=CH), anal. calcd for $C_{52}H_{82}O_7$ 77.10, H 9.59; found: C 77.20, H 9.40

Synthesis of side chain discotic polysiloxane via hydrosilylation of (4) with poly(methylhydrosiloxane) (5) (Figure 1)

2 g (2.38 mmol) of (**4**) and 128 mg of poly(methylhydrosiloxane) (2.14 mmol of –[CH_3Si(H)O–]– monomeric units were dissolved in 20 ml of dry

toluene and stirred under argon. Platinum tetramethyldivinyldisiloxane (PTDD) complex in xylenes (10^{-4} mol Pt/mol SiH) was added and the reaction mixture was stirred at 60°C. Reaction progress was followed by FTIR (disappearance of Si–H absorption band at 2150 cm^{-1}). After 24 hrs the amount of unreacted Si–H bonds was ~11% and after 48 hrs 6% was left. The reaction was continued until the total disappearance of the absorption at 2150 cm^{-1} (72 hrs). The solvent was removed in vacuum, leaving white solid. The product was purified by multiple precipitations from dichloromethane/methanol, filtration using PTFE 0.45 μm microfilter and was dried in vacuum (75°C, 1 mmHg) (yield 1.23 g, 58%). ^{1}H NMR: (200 MHz, toluene-D, δ) 0.04 (s, 3H, $SiCH_3$), 0.40–0.65 (m, 2H, $Si–CH_2$), 0.76–0.98 (m, 12H, $CH_3–(CH_2)_5O$), 1.22–1.38 (m, 30H, $CH_3(CH_2)_2(CH_2)_3O$ + $Si–CH_2(CH_2)_7(CH_2)_2COO$), 1.40–1.65 (m, 8H, $CH_3(CH_2)_2CH_2(CH_2)_2O$), 1.80–2.21 (m, 8H, $CH_3(CH_2)_3CH_2CH_2O$), 2.64–2.70 (m, 2H, $Si–(CH_2)_8CH_2CH_2COO$), 3.25–3.57 (m, 2H, $Si–(CH_2)_9CH_2COO$), 3.97 (s, 3H, OCH_3), 4.18–4.35 (m, 8H, $CH_3(CH_2)_4CH_2O$), 6.82 (s, 2H, aromatic protons from undecanoate/OCH_3 substituted ring), 7.73–7.95 (m, 4H, aromatic from hexyloxy substituted rings), (Figure 1), ^{13}C NMR: (500 MHz, standard proton decoupling, C_6D_6, δ) 0.38 (CH_3Si), 14.2 (CH_3), 17.4 ($SiCH_2$), 20.6 ($SiCH_2CH_2$), 20.8 ($Si(CH_2)_2CH_2$), 22.9 (CH_3CH_2), 25.1 ($Si(CH_2)_3CH_2$), 25.9 ($CH_3CH_2CH_2$), 29.4 ($Si(CH_2)_4CH_2$), 30.8 ($CH_3(CH_2)_2CH_2$), 30.9 ($Si(CH_2)_5CH_2$), 31.0 ($Si(CH_2)_6CH_2$), 31.1 ($Si(CH_2)_7CH_2$), 32.6 ($CH_3(CH_2)_3CH_2$), 32.9 ($Si(CH_2)_8CH_2$), 33.8 ($O(O)CCH_2$), 55.7 (OCH_3), 68.9 (OCH_2), 103.3, 103.4, 103.6, 103.9 (aromatic carbons from hexyloxy substituted rings), 111.0, 111.1 (aromatic carbons from undecanoate/OCH_3 substituted ring), ^{29}Si NMR: (500 Mhz, INEPT, C_6D_3 δ): –5 (MeSiO), GPC: M_n = 36 800, M_w = 56 200.

3. Results and discussion

3.1. Synthesis

The easiest and most frequently used method in polymer chemistry to attach side chains to polysiloxanes is hydrosilylation reaction, in which terminal alkenes are silylated with polymers bearing Si–H moieties [27, 28]. However, the synthetic bottleneck was the preparation of unsymmetrically substituted conjugated aromatic structures (3) possessing one single substituent with terminal alkene moiety (4), which can be later attached to polysiloxanes as a side chain via hydrosilylation reaction. We have applied a modified methodology, described for synthesis of similar triphenylenes, bearing one reactive group, which served as monomers for the preparation of side chain discotic polyacetylenes (Figure 1).

It involved cyclotrimerization of a mixture of 1,2-dihexyloxybenzene and guiacol leading to 'one-pot' formation of the triphenylene moiety (3) (Figure 1). The reaction was straightforward, however, required careful purification using several cycles of column chromatography in order to separate undesired side products such as perhexyloxy triphenylenes. This procedure led to a lower reaction yield.

In the second step (Figure 1) the esterification of (3) with undecenoic acid was carried out, catalyzed by DMAP in the presence of DCC. Again, the most

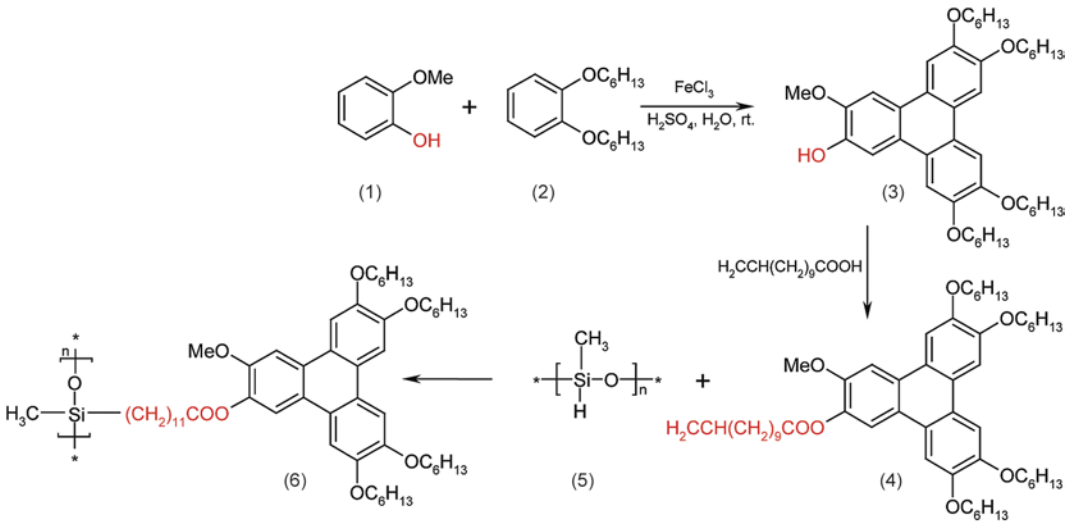

Figure 1. Synthesis of unsymmetric triphenylene and the relevant discotic side chain polysiloxane

difficult part of the process was purification of the ester (4). The attachment of the side triphenylene groups to the polysiloxane was performed in typical hydrosilylation conditions (Figure 1) in toluene using Karstedt's catalyst at 60–80°C.

The conversion of 90% after 24 hrs (as proved by disappearance of Si–H signal at 2100 cm^{-1} in FTIR) was rather typical for hydrosilylation of alkenes, bearing bulky substituents, by polysiloxanes [26, 27]. The reaction continued for further 48 hrs led to final anchoring of 94% of unsaturated triphenylene ester. Although the final product (**6**) contained 6% of the unreacted Si–H moieties, they were hydrolytically stable and we did not observe the effect of cross-linking by Si–H hydrolysis and condensation even if the samples were heated up to 150°C and washed with water.

3.2. Phase behavior studies

Phase transition studies were carried out for triphenylene (**4**) and the discotic polymer (**6**) (Figure 1). All measurements were made by heating and cooling at the same rate of 5°C/min. The DSC heating scan (Figure 2a) reveals a phase transition temperature from the crystalline (Cr) to the liquid crystalline (LC) phase at 68°C for (**4**) and 67°C for (**6**). The temperature difference, which accompanies this transition for (**4**) and (**6**) is ΔT = 1°C and a corresponding small change in enthalpy is observed (ΔH = 0.6 J/g). Transition to the isotropic phase (Iso) occurs at the temperature of 99°C and is identical for both monomer (**4**) and polymer (**6**).

Upon cooling at the rate of 5°C/min, phase transitions from Iso to LC for both monomer (**4**) and polymer (**6**) occurs at 96°C (lack of a supercooling) and is accompanied by a enthalpy change ΔH = 6.9 J/g (Figure 2b). On the other hand, a small temperature difference of ΔT = 1°C between (**4**) and (**6**) is observed (Figure 2b) for the transition from the LC to Cr phase with 52°C for (**4**) and 51°C for (**6**).

In addition to measurements obtained from differential scanning calorimetry (DSC) analysis, the phase transitions of (**4**) and (**6**) were independently studied by means of thermooptical analysis (TOA). The TOA experiments rely on the registration of intensity of polarized light and change of texture with temperature [23, 29]. Changes of the transmission of polarized light as function of temperature were recorded. Simultaneously, the morphology of layers was observed under optical microscope. TOA measurements were done for drop-cast films on a glass substrate. During measurements the layers were exposed to air without using a cover. The changes of the light intensity transmitted through the layers of (**4**) upon heating at a rate of 5°C/min are shown in Figure 3. Upon heating of (**4**) the intensity of the transmitted light increases sharply at 67°C and accompanies the Cr–LC transition, which can be attributed to the formation of mesomorphic state (LC) [30, 31] (Figure 3, image 1, 2). A fast decrease in intensity is observed at 98°C, when the clearing temperature is reached (Figure 3, image 4)

The observed phase transitions were accompanied by the respective changes in the intensity of polarized light passing through the layer (Figure 3b). In order to measure precisely the temperatures, at which the phase transition occurred, the plot of dI/dT is

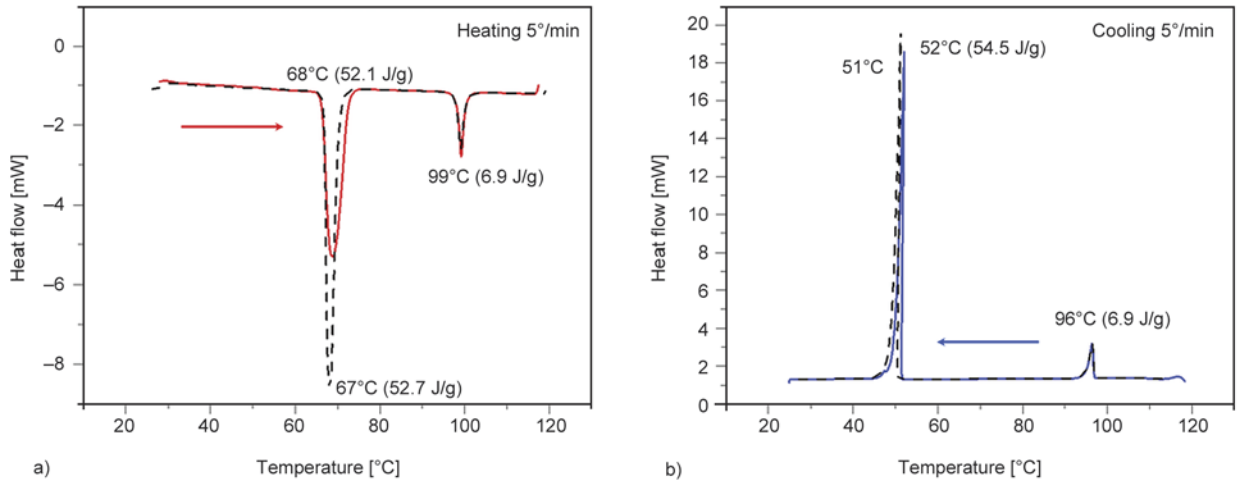

Figure 2. DSC thermogram: a) heating: red, continuous curve (**4**); black, dashed curve (**6**), b) cooling: blue, continuous curve (**4**); black, dashed curve (**6**)

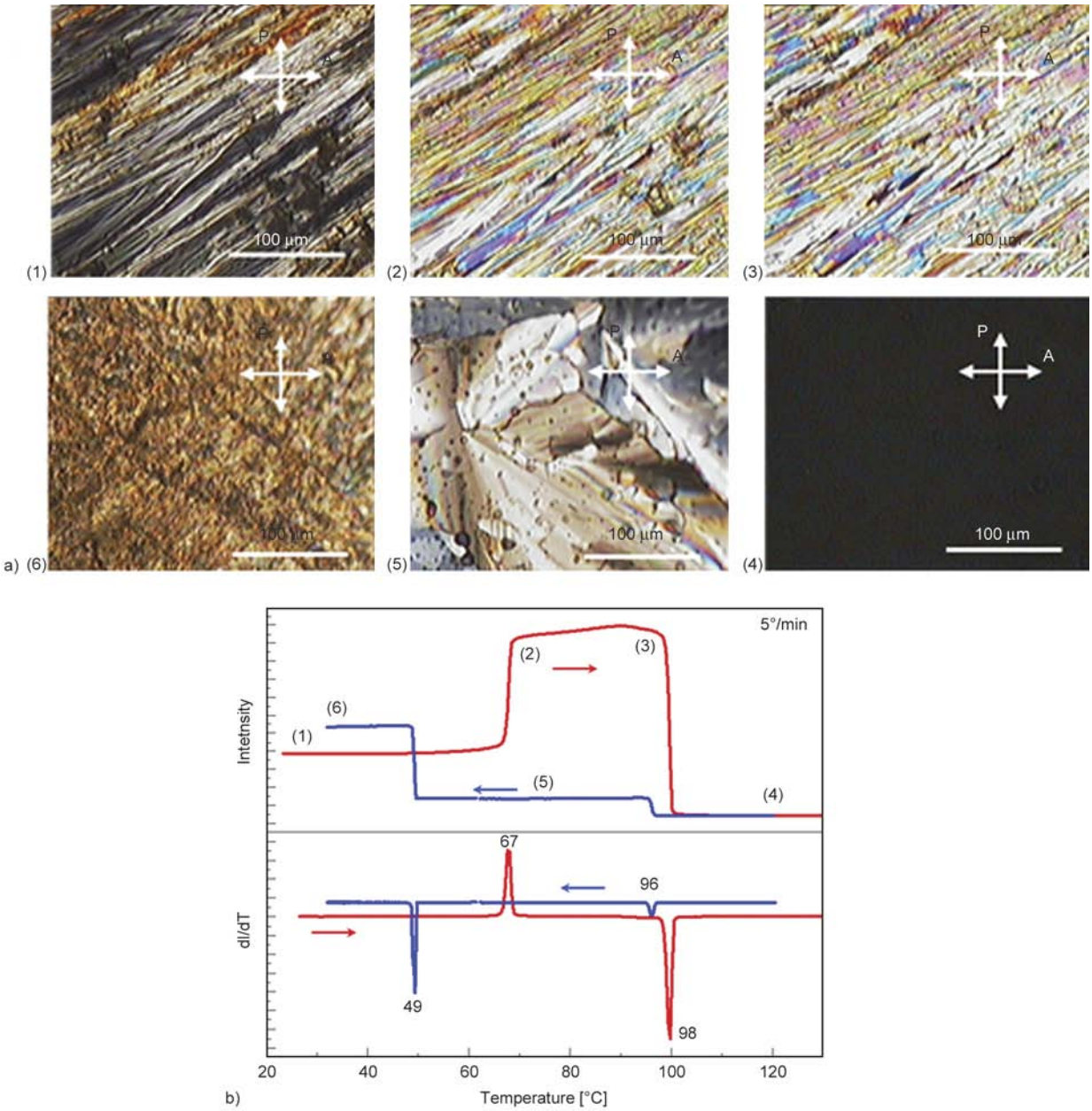

Figure 3. a) Images of textures of (**4**) from POM, b) TOA of (**4**): red curve corresponds to heating and blue curve to cooling process

presented. On cooling, the intensity increased at the temperature of 96°C (see Figure 3, blue curve d*I*/d*T*, image 4) due to formation of a fan structure by (**4**), which is characteristic for discotic liquid crystals [32]. In image 6 of Figure 3a the transition to the crystalline phase occurring at 49°C is evident. The results from TOA for the triphenylene (**4**) correlate very well with the data obtained from the differential scanning calorimetry (DSC).

TOA analysis of polymer (**6**) points that on heating of the layer the Cr–LC transition is observed changing the orientation of molecules [33]. This results in an increase in light intensity passing through the layer (red curve Figure 4a, image 1 and 2) at 58°C. Further heating causes a complete reorientation of the molecules in the layer and the transition to the mesophase (LC) (image 3) at 67°C. Rapid decline in light intensity occurs at a temperature of 98°C and the transition to the isotropic liquid is observed (image 4). On the other hand, on cooling from the isotropic liquid, the intensity change of light passing through the layer of (**6**) occurs only at the temperature of 48°C, corresponding very well with results from DSC, indicating crystallization (image 6). The results obtained from TOA and DSC apparently differ from each other. As one can see from the texture

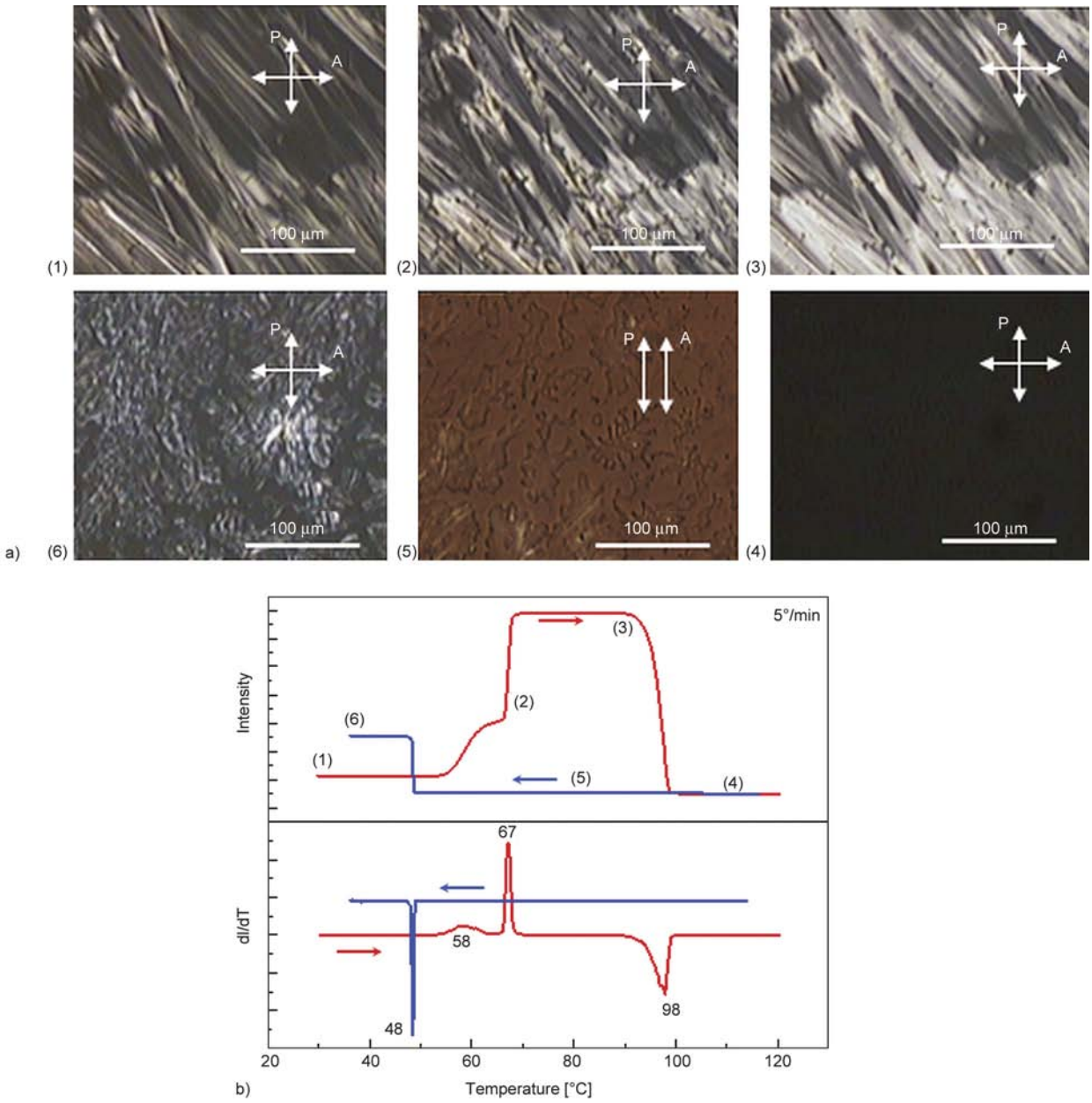

Figure 4. a) Images of textures of polymer (**6**) from POM, b) TOA of (**6**): red curve corresponds heating and blue curve to cooling process. Heating and cooling rates are 5°C/min.

recorded at 82°C (image 5) the LC transition is missing. On cooling from the isotropic phase (at 96°C – DSC) no change in the light intensity occurs in TOA (Figure 4b). The reason is most probably the formation of a homeotropic arrangement of the triphenylene molecules on the surface. In this organization, the molecules are face-on arranged on the surface with their columnar axis perpendicular to the substrate. This leads to the lack of birefringence in polarized light for typically a dendritic morphology of the LC phase [34–36]. We observed in TOA characteristic textures for this type arrangement [21] (Figure 4 – image 5) indicating a strong interaction with the substrate (Figure 4b).

For each layer (**4** and **6**) the morphology surface was analyzed using atomic force microscopy (AFM) (Figure 5). Thickness of each mono-layer (Figure 5b) of ca. 1.8 nm (corresponding to the thickness of a single sheet of columns) is in a reasonable agreement with earlier measurements performed on layers of similar triphenylenes [22] forming columnar structures. Additionally, this value is in accordance with the intercolumnar distance found for the bulk organization by X-ray scattering (Figure 7). All surface morphology studies were performed at 25°C for as-cast samples. Analysis of the surface of polymer (**6**) was performed after the first heating cycle to a temperature of 120°C. Observed morphologies of poly-

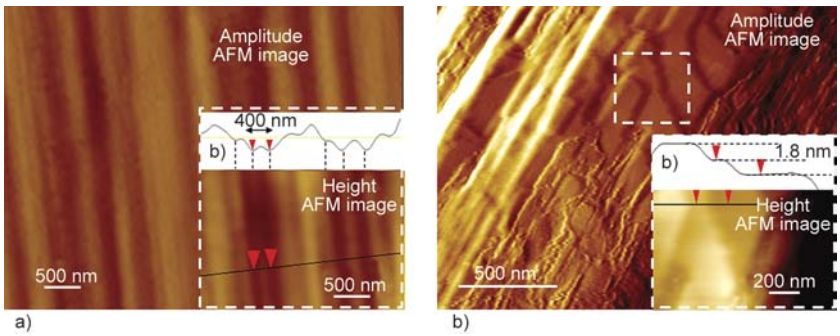

Figure 5. AFM images: a) (**4**) amplitude image showing periodic structure, b) (**6**) amplitude image with a thickness of a single monolayer

mer liquid crystal (**6**), from AFM, shows the formation of regular patterns where the distances between interdigitated multilayer polymer chains are 15 nm. (Figure 6) [37, 38].

The thermotropic behavior of (**4**) and (**6**) in bulk was studied by two-dimensional X-ray wide-angle scattering (2D-WAXS). The samples were prepared by fiber extrusion to induce macroscopic alignment in the specimen and were placed for the measurement vertically towards the 2D detector. In the LC phase both compounds self-assemble in identical characteristic structures (Figure 7b, 7d) [39]. The columnar stacks are oriented along the fiber direction as evident from the small-angle equatorial reflections. From the position of these scattering intensities the intercolumnar arrangement is determined of a slightly oblique with dissimilar unit cell parameters a = 2.29 nm and b = 2.08 nm for (**4**) and a = 2.31 nm and b = 2.10 nm for (**6**). The disc-shaped triphenylenes pack in an orthogonal fashion in these stacks with a π-stacking distance of 0.36 nm in both cases as derived from the meridional wide-angle reflections (Figure 7f). Cooling back the samples to their crystalline phase, the organization changes into a herringbone structure with tilted molecules within the columnar structures (Figure 7a, 7c). The location of the off-meridional reflections with the maximum intensity indicates a similar tilting angle of ca 35° for both compounds (Figure 7e). Due to the high number of reflections, the intercolumnar distance cannot be determined precisely from the data set. However, the comparison of the equatorial reflection suggests also a similar unit cell for (**4**) and (**6**) in the crystalline phase. In conclusion of the structural analysis, the introduction of the triphenylene as a side chain moiety of a polysiloxane does not affect the supramolecular bulk organization of the polycyclic aromatic hydrocarbon disc. The driving force for the self-assembly are π-stacking interactions, while the polysiloxane chain plays a minor role for the bulk structure. It can be assumed that the polysiloxane is arranged in the periphery of the stacks connecting molecules packed in the same column.

4. Conclusions

The synthetic pathway involved the known hydrosilylation process [22] for preparation of a novel system with hexyloxy modified triphenylene anchored

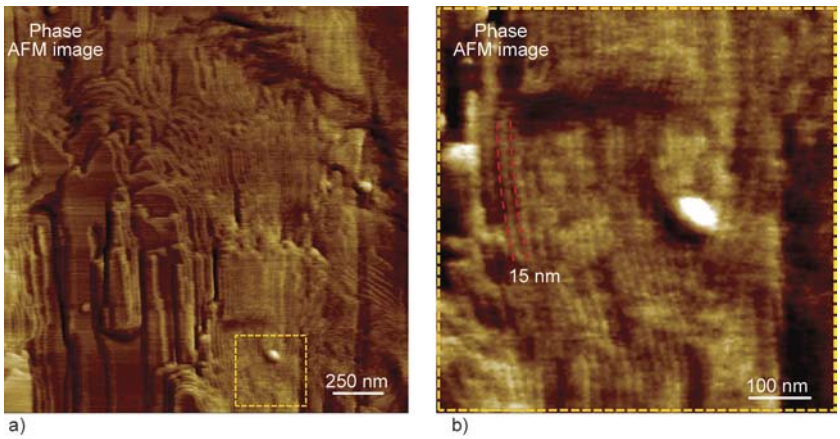

Figure 6. AFM phase images of polymer (**6**); a) phase image for a 1×1 μm^2 area, b) zoom of yellow square from a) showing 15 nm regular patterns

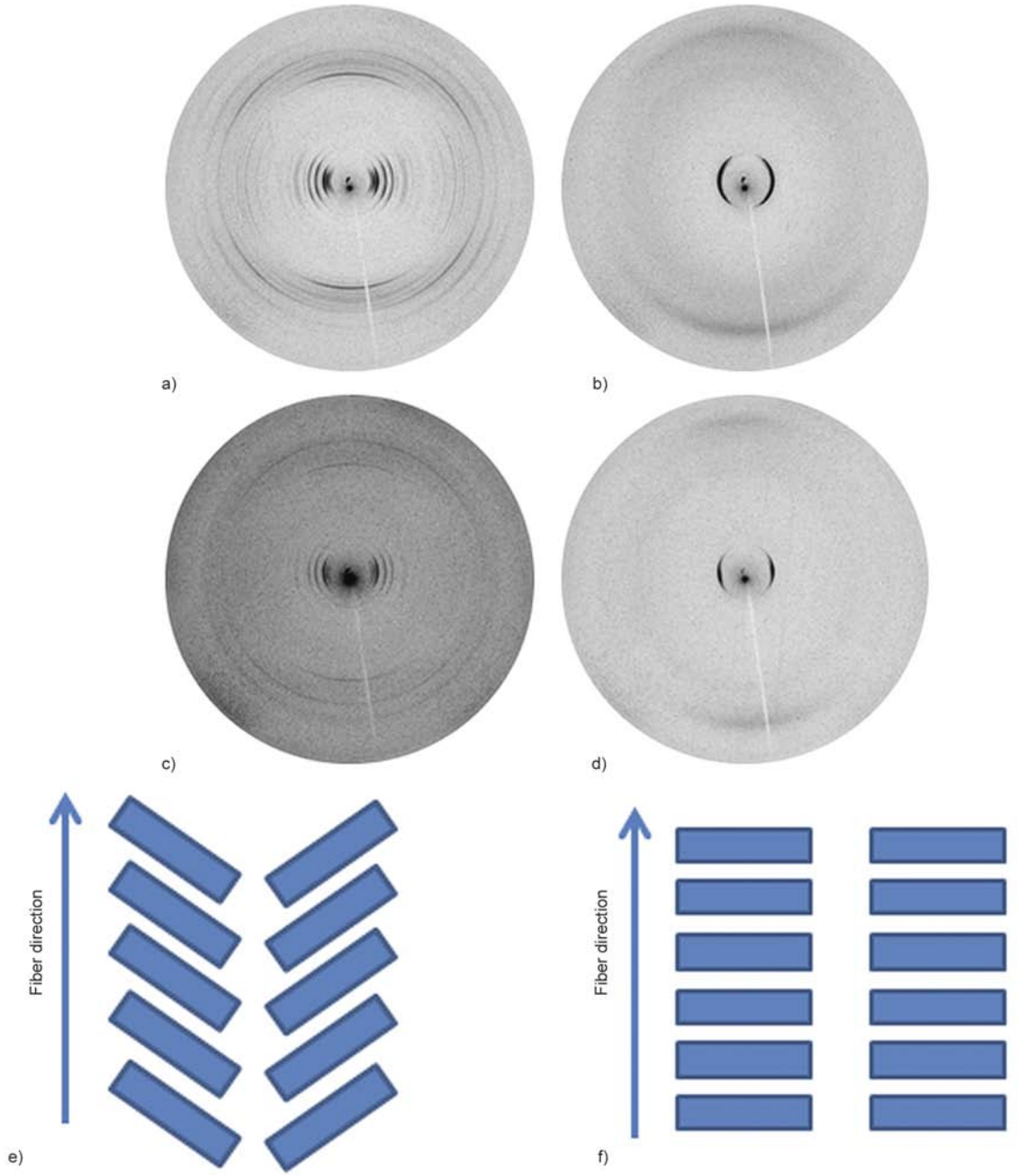

Figure 7. 2D-WAXS recorded at 30 and 80°C of a) and b) (**4**), c) and d) (**6**). Schematic illustration for the organization in e) crystalline and f) liquid crystalline phase.

on low molecular weight polysiloxane (2100 g·mol^{-1}) via undecanoate flexible spacer. Transition temperatures determined by TOA correspond to those from DSC. Therefore, TOA can be considered as a very efficient and complementary tool for studies of phase transitions of some discotic systems. Moreover, smaller amount of materials (thickness layers smaller than 1 μm can be analysed) is required for TOA experiments. Attachment of modified triphenylene moieties to polysiloxane via flexible spacer allows for self-organization of both side chain discotics and polymer skeleton. The spacer effectively decouples the motions of triphenylene side groups from the main polymer chain. Thus, the columnar ordering of side groups is still present. The attachment of triphenylene derivatives does not affect significantly the kinetics of self-organization (crystallization) in comparison to the plain discotic precursor, but provides higher thermal stability, characteristic of polymers. The onset temperature increases from 352.24°C (**4**) to 395.04°C for polymer system (**6**) and the respective decomposition rate decreases from

9.16%·min/°C (**4**) to 6.59%·min/°C (**6**). A good solubility in non-polar solvents is also assured by the presence of siloxane chain.

Acknowledgements

T.G., T.M and W.A.S. wish to thank Centre of Molecular and Macromolecular Studies for financial support within the statutory research program. W.Z. gratefully acknowledges the ERC Advanced Grant NANOGRAPH (AdG-2010-267160).

References

[1] Laschat S., Baro A., Steinke N., Giesselmann F., Hägele C., Scalia G., Judele R., Kapatsina E., Sauer S., Schreivogel A., Tosoni M.: Discotic liquid crystals: From tailor-made synthesis to plastic electronics. Angewandte Chemie International Edition, **46**, 4832–4887 (2007).
DOI: 10.1002/anie.200604203

[2] Pisula W., Zorn M., Chang J. Y., Müllen K., Zentel R.: Liquid crystalline ordering and charge transport in semiconducting materials. Macromolecular Rapid Communications, **30**, 1179–1202 (2009).
DOI: 10.1002/marc.200900251

[3] Sergeyev S., Pisula W., Geerts Y. H.: Discotic liquid crystals: A new generation of organic semiconductors. Chemical Society Reviews, **36**, 1902–1929 (2007).
DOI: 10.1039/B417320C

[4] Wong W. W. H., Singh T. B., Vak D., Pisula W., Yan C., Feng X., Williams E. L., Chan K. L., Mao Q., Jones D. J., Ma C-Q., Müllen K., Bäuerle P., Holmes A. B.: Solution processable fluorenyl hexa-peri-hexabenzocoronenes in organic field-effect transistors and solar cells. Advanced Functional Materials, **20**, 927–938 (2010).
DOI: 10.1002/adfm.200901827

[5] Wong W. W. H., Ma C-Q., Pisula W., Yan C., Feng X., Jones D. J., Müllen K., Janssen R. A. J., Bäuerle P., Holmes A. B.: Self-assembling thiophene dendrimers with a hexa-peri-hexabenzocoronene core–synthesis, characterization and performance in bulk heterojunction solar cells. Chemistry of Materials, **22**, 457–466 (2009).
DOI: 10.1021/cm903272y

[6] Tsao H. N., Pisula W., Liu Z., Osikowicz W., Salaneck W. R., Müllen K.: From ambi- to unipolar behavior in discotic dye field-effect transistors. Advanced Materials, **20**, 2715–2719 (2008).
DOI: 10.1002/adma.200702992

[7] Tracz A., Makowski T., Masirek S., Pisula W., Geerts Y. H.: Macroscopically aligned films of discotic phthalocyanine by zone casting. Nanotechnology, **18**, 485303/1–485303/5 (2007).
DOI: 10.1088/0957-4484/18/48/485303

[8] Kastler M., Pisula W., Laquai F., Kumar A., Davies R. J., Baluschev S., Garcia–Gutiérrez M. C., Wasserfallen D., Butt H. J., Riekel C., Wegner G., Müllen K.: Organization of charge-carrier pathways for organic electronics. Advanced Materials, **18**, 2255–2259 (2006).
DOI: 10.1002/adma.200601177

[9] Miskiewicz P., Rybak A., Jung J. Y., Glowacki I., Maniukiewicz W., Tracz A., Pfleger J., Ulanski J., Müllen K.: One-step method of producing uniaxially oriented layers of organic discotic molecules for field-effect transistors. Nonlinear Optics, Quantum Optics, **37**, 207–218 (2007).

[10] Pisula W., Tomović Ž., Watson M. D., Müllen K., Kussmann J., Ochsenfeld C., Metzroth T., Gauss J.: Helical packing of discotic hexaphenyl hexa-peri-hexabenzocoronenes: Theory and experiment. The Journal of Physical Chemistry B, **111**, 7481–7487 (2007).
DOI: 10.1021/jp071167i

[11] Warman J. M., Piris J., Pisula W., Kastler M., Wasserfallen D., Müllen K.: Charge recombination via intercolumnar electron tunneling through the lipid-like mantle of discotic hexa-alkyl-hexa-*peri*-hexabenzocoronenes. Journal of the American Chemical Society, **127**, 14257–14262 (2005).
DOI: 10.1021/ja053225o

[12] Hoang M. H., Nguyen D. N., Choi D. H.: π-extended conjugated semiconducting molecules based on triphenylene. Advances in Natural Sciences: Nanoscience and Nanotechnology, **2**, 035002/1–035002/8 (2011).
DOI: 10.1088/2043-6262/2/3/035002

[13] van de Craats A. M., Warman J. M., de Haas M. P., Adam D., Simmerer J., Haarer D., Schuhmacher P.: The mobility of charge carriers in all four phases of the columnar discotic material hexakis(hexylthio)triphenylene: Combined TOF and PR-TRMC results. Advanced Materials, **8**, 823–826 (1996).
DOI: 10.1002/adma.19960081012

[14] Cammidge A. N., Bushby R. J.: Synthesis and structural features of discotic liquid crystals. Wiley, Weinheim (1998).

[15] Adam D., Closs F., Frey T., Funhoff D., Haarer D., Ringsdorf H., Schuhmacher P., Siemensmeyer K.: Transient photoconductivity in a discotic liquid crystal. Physical Review Letters, **70**, 457–461 (1993).
DOI: 10.1103/PhysRevLett.70.457

[16] Cammidge A. N., Gopee H.: Structural factors controlling the transition between columnar-hexagonal and helical mesophase in triphenylene liquid crystals. Journal of Materials Chemistry, **11**, 2773–2783 (2001).
DOI: 10.1039/B103450M

[17] Xiao B., Liu Z-J., Wang B-Q., Hu P., Redshaw C., Zhao K-Q.: Synthesis of triphenylene discotic liquid crystals possessing nine alkyl chains: Influence of molecular symmetry and chain length on mesomorphism. Molecular Crystals and Liquid Crystals, **577**, 25–35 (2013).
DOI: 10.1080/15421406.2013.781489

[18] Dubois J-C., Barny P. L., Mouzac M., Noel C.: Behaviour and properties of side group thermotropic liquid crystal polymers. in 'Handbook of liquid crystals' (eds.: Demus D., Goodby J., Gray G. W., Spiess H. W., Vill V.) Wiley-VCH, Weinheim, Vol 3, 207–228 (1998).
[19] Zelcer A., Donnio B., Bourgogne C., Cukiernik F. D., Guillon D.: Mesomorphism of hybrid siloxane-triphenylene star-shaped oligomers. Chemistry of Materials, **19**, 1992–2006 (2007).
DOI: 10.1021/cm062949b
[20] Han B., Hu P., Wang B-Q., Redshaw C., Zhao K-Q.: Triphenylene discotic liquid crystal trimers synthesized by $Co_2(CO)_8$-catalyzed terminal alkyne [2 + 2 + 2] cycloaddition. Beilstein Journal of Organic Chemistry, **9**, 2852–2861 (2013).
DOI: 10.3762/bjoc.9.321
[21] Hüser B., Pakula T., Spiess H W.: Macroscopic ordering of liquid-crystalline polymers with discotic mesogens. Macromolecules, **22**, 1960–1963 (1989).
DOI: 10.1021/ma00194a073
[22] Kumar S.: Triphenylene-based discotic liquid crystal dimers, oligomers and polymers. Liquid Crystals, **32**, 1089–1113 (2005).
DOI: 10.1080/02678290500117415
[23] Ganicz T., Makowski T., Stanczyk W. A., Tracz A.: Side chain polysiloxanes with phthalocyanine moieties. Express Polymer Letters, **6**, 373–382 (2012).
DOI: 10.3144/expresspolymlett.2012.40
[24] Ganicz T., Stańczyk W.: Side-chain liquid crystal polymers (SCLCP): Methods and materials. An overview. Materials, **2**, 95–128 (2009).
DOI: 10.3390/Ma2010095
[25] Armarego W. L. F., Chai C.: Purification of laboratory chemicals. Butterworth-Heinemann, Oxford (2012).
[26] Xing C., Lam J. W. Y., Zhao K., Tang B. Z.: Synthesis and liquid crystalline properties of poly(1-alkyne)s carrying triphenylene discogens. Journal of Polymer Science Part A: Polymer Chemistry, **46**, 2960–2974 (2008).
DOI: 10.1002/pola.22631
[27] Marciniec B., Gulinski J., Urbaniak W., Kornetka Z. W.: Comprehensive handbook on hydrosilylation. Pergamon Press, Oxford (1992).
[28] Marciniec B.: Hydrosilylation. Springer, Heidelberg (2009).
[29] Trzaska J., Galewski Z.: Liquid-crystalline properties of 4-alkyl-, 4-alkyloxy and 4-halogene-4′-hydroxyazobenzene alkyloates. Opto-Electronics Review, **17**, 129–139 (2009).
DOI: 10.2478/s11772-008-0071-7
[30] Praefcke K., Kohne B., Singer D.: Hexaalkynyltriphenylene: A new type of nematic-discotic hydrocarbon. Angewandte Chemie International Edition, **29**, 177–179 (1990).
DOI: 10.1002/anie.199001771
[31] Zamir S., Spielberg N., Zimmermann H., Poupko R., Luz Z.: On the solid polymorphs of the discotic mesogen hexa-octanoyloxytriphenylene. Liquid Crystals, **18**, 781–786 (1995).
DOI: 10.1080/02678299508036690
[32] Hird M.: Textures of liquid crystals. Angewandte Chemie, **115**, 5969–5970 (2003).
DOI: 10.1002/ange.200385054
[33] Cheda J. A. R., García M. V., Redondo M. I., Gargani S., Ferloni P.: Short chain copper(II) *n*-alkanoate liquid crystals. Liquid Crystals, **31**, 1–14 (2004).
DOI: 10.1080/02678290310001628500
[34] Pisula W., Kastler M., El Hamaoui B., García-Gutiérrez M-C., Davies R. J., Riekel C., Müllen K.: Dendritic morphology in homeotropically aligned discotic films. ChemPhysChem, **8**, 1025–1028 (2007).
DOI: 10.1002/cphc.200600787
[35] Schweicher G., Gbabode G., Quist F., Debever O., Dumont N., Sergeyev S., Geerts Y. H.: Homeotropic and planar alignment of discotic liquid crystals: The role of the columnar mesophase. Chemistry of Materials, **21**, 5867–5874 (2009).
DOI: 10.1021/cm902634r
[36] Thiebaut O., Bock H., Grelet E.: Face-on oriented bilayer of two discotic columnar liquid crystals for organic donor–acceptor heterojunction. Journal of the American Chemical Society, **132**, 6886–6887 (2010).
DOI: 10.1021/ja1012596
[37] Verploegen E., Zhang T., Murlo N., Hammond P. T.: Influence of variations in liquid-crystalline content upon the self-assembly behavior of siloxane-based block copolymers. Soft Matter, **4**, 1279–1287 (2008).
DOI: 10.1039/B800212F
[38] Thünemann A. F., Ruppelt D., Burger C., Müllen K.: Long-range ordered columns of a hexabenzo[*bc*,*ef*,*hi*,*kl*,*no*,*qr*]coronene–polysiloxane complex: Towards molecular nanowires. Journal of Materials Chemistry, **10**, 1325–1329 (2000).
DOI: 10.1039/A909010J
[39] Pisula W., Feng X., Müllen K.: Tuning the columnar organization of discotic polycyclic aromatic hydrocarbons. Advanced Materials, **22**, 3634–3649 (2010).
DOI: 10.1002/adma.201000585

eXPRESS Polymer Letters Vol.9, No.7 (2015) 647–657
Available online at www.expresspolymlett.com
DOI: 10.3144/expresspolymlett.2015.60

Curing of bisphenol A-aniline based benzoxazine using phenolic, amino and mercapto accelerators

*A. Ručigaj, B. Alič, M. Krajnc, U. Šebenik**

University of Ljubljana, Faculty of Chemistry and Chemical Technology, Večna pot 113, 1000 Ljubljana, Slovenia

Received 15 December 2014; accepted in revised form 8 February 2015

Abstract. The curing of bisphenol A-aniline based benzoxazine was studied applying different accelerators (4,4′-thiodiphenol, *o*-dianisidine, 2-mercaptobenzimidazole and 4-mercaptophenol) to initiate the catalytic ring-opening of benzoxazine. Possible pathways of benzoxazine ring-opening, polymerization and cross-linking without and with the addition of different accelerators are presented. The curing kinetics was investigated by model-free kinetic analysis of experimental data obtained by differential scanning calorimetry (DSC). The addition of different accelerators significantly reduced the onset temperature of curing in dynamic experiments. The effects of accelerators on the results of isothermal conversion prediction were studied and discussed in detail. Among the used accelerators, thiodiphenol showed the best accelerating efficiency and was consequently used in further studies, where its amount was varied. By low heating rate DSC analysis the catalytic ring-opening, thermally accelerated ring-opening and the diffusion-controlled steps were identified. The amount of added accelerator affected particularly the ring-opening and diffusion-controlled steps.

Keywords: *thermosetting resins, benzoxazine, accelerators, curing mechanisms, deconvolution*

1. Introduction

Recently, much attention has been given to the development of benzoxazine-based family of phenolic resins due to their adaptable mechanical and physical properties, which are often considerably better than those of traditional phenolic resins [1]. Benzoxazines are a class of heterocyclic compounds with typically one or two oxazine rings in their molecules. They are synthesized from a phenolic derivative, a primary amine and formaldehyde. Polybenzoxazines are formed by ring-opening polymerization of benzoxazine molecules. Properties of polybenzoxazines can be easily adjusted due to a high design flexibility of their molecular architecture, which opens great opportunities in further enhancement of benzoxazine resins properties. They have demonstrated various attractive properties such as good thermal, mechanical, chemical, electrical and physical properties, high char yields, high glass transition temperature (T_g), low water absorption, near-zero shrinkage, and low flammability. The important factor, which has great influence on their adoption, both in the academic and industrial communities, is also their relative cheapness. However, the disadvantages associated with polybenzoxazines, which need to be addressed, are their high curing temperature (i.e. polymerization and cross-linking temperature), brittleness and outgassing during the curing process [2–10].

The classical method for production of polybenzoxazines is polymerization of benzoxazine monomers at high temperature (usually at $T > 180$°C) without the addition of an accelerator [1], which may be a catalyst, initiator, or co-monomer. However, the high temperature, which is required for the curing process, may in some cases lead to thermal degradation of

*Corresponding author, e-mail: urska.sebenik@fkkt.uni-lj.si

the corresponding resin [11]. Lower curing temperature would therefore lead to a significant process and resulting material improvement. In order to respond to this issue, a considerable amount of different catalysts have been applied to promote ring-opening polymerization, including nucleophilic catalysts and Lewis acids [12–14]. Also the use of carboxylic acid groups as accelerators have been extensively studied and a significant decrease in the polymerization temperature has been observed [15–17]. Even though, the studied catalysts showed good catalytic activities, there is still much effort needed for further lowering of the polymerization temperature [18]. The important question, when using benzoxazines of different chemical structures in combination with different catalysts, is the effect of functional groups present in benzoxazine and catalyst molecules not only on the ring-opening but also on the polymerization and cross-linking reactions. Therefore, it is of great importance to understand the nature of the cured material and the effect certain functional group has on the curing process, i.e. on the ring-opening, polymerization and cross-linking mechanisms [1, 2, 12, 14, 19–29].

The terminology used for accelerators is varied and may sometimes cause confusion since the terms accelerator, catalyst, promoter, initiator, etc., are sometimes used loosely even though they can apply to very specific types of materials having distinctly different characteristics and functions. This study focuses on benzoxazine resin systems and the term accelerator is used to describe a variety of compounds used to increase the reaction rate, whatever the reaction mechanism. The term accelerator is applied instead of terms catalyst, initiator, and/or co-monomer, since the applied accelerators initiate ring-opening polymerization and co-react with benzoxazine to form polybenzoxazine. In the literature of curing reactions the term catalyst is often used, but by definition a catalyst lowers the activation energy of a chemical process without being a reactant.

In the present study, we have examined the accelerating efficiency of a number of different accelerators in the curing process of bisphenol A-aniline based benzoxazine (BOX). Possible pathways of benzoxazine ring-opening, polymerization and cross-linking without and with the addition of different accelerators are presented. The curing kinetics was investigated by model-free kinetic analysis of experimental data obtained by differential scanning calorimetry (DSC). The basic assumption for the application of DSC technique for curing process following is that the rate of kinetics process is proportional to the measured heat flow [30–32]. Among tested accelerators, thiodiphenol showed the best effect on the curing process of benzoxazine in terms of conversion predictions obtained by isoconversional model-free approach. For that reason the effects of different amounts of thiodiphenol on the curing process of benzoxazine were studied in detail.

2. Experimental

2.1. Materials

For the kinetic studies, benzoxazine based on bisphenol A and aniline (BOX, 98%) was employed along with different polymerization accelerators. As accelerators 4,4′-thiodiphenol (TDP, 99%), *o*-dianisidine (DA, 97%), 2-mercaptobenzimidazole (MBI, 98%) and 4-mercaptophenol (MP, 90%) were used as received from Sigma-Aldrich Chemie GmbH, (Steinheim, Germany). Bisphenol A-aniline based benzoxazine (commercial name Araldite MT 35600) was kindly provided by Huntsman Advanced Materials (BVBA, Everberg, Belgium).

2.2. Sample preparation

Homogeneous mixtures of benzoxazine monomer and accelerators were prepared by dissolving them in 10 mL of dichloromethane by mixing with magnetic stirrer for 15 minutes. The solvent was then removed from samples by evaporation at room temperature for 12 hours and subsequent drying for 4 hours in vacuum oven at 60°C. For DSC experiments benzoxazine mixtures with 20 mol of accelerator (TDP, DA, MBI and MP) per 100 mol of benzoxazine (16.7 mol%) were prepared. The amounts of different accelerators in benzoxazine mixtures are given in mol% in order to provide comparable quantity between the mixtures. When the amount of accelerator on benzoxazine/thiodiphenol mixture curing was investigated, the prepared benzoxazine/thiodiphenol contained 1, 2, 5, 10, 20, 35 and 50 wt% to the weight of benzoxazine.

2.3. Differential scanning calorimetry (DSC)

The DSC measurements were performed on Mettler Toledo DSC1 instrument with intra-cooler using STAR software. In and Zn standards were used for the temperature calibration and for the determina-

tion of the instrument time constant. Samples of around 10 mg were weighed in standard 40 μL aluminum pans. DSC measurements were performed in nitrogen atmosphere with 30 mL/min nitrogen flow rate. For investigation of the effect of accelerator type on curing kinetics the samples were subjected to four different heating rates (5, 10, 15 and 20°C/min) in the temperature range from 20 to 350°C. To study the effect of different amounts of thiodiphenol on the curing process also a lower heating rate of 1°C/min was used.

3. Results and discussion

3.1. Curing reaction

Curing (polymerization and cross-linking) of benzoxazine is thermally accelerated cationic ring-opening polymerization, which may be carried out with or without using accelerators (Figure 1). Different accelerators, which lower benzoxazine curing temperature, may bear different functional groups capable of initiating or catalyzing the oxazine ring opening. This is why several mechanisms were proposed for benzoxazine curing [13, 14, 26, 33–35]. Regardless to the type of the accelerator used, the mechanism of the curing process involves several steps, which complicate the kinetics. The curing is always autocatalyzed as the newly produced hydroxyl groups in phenolic structure (compound III in Figure 1a) act as an additional initiator. Moreover, in the early stage of curing, the reaction medium is a liquid composed of benzoxazine, accelerator and just formed oligomers. As the reaction progresses, the average molecular weight, the viscosity and the glass transition temperature (T_g) of the resin increase. Therefore the molecular mobility, in turn, decreases, which affects the curing kinetics. The latter becomes diffusion rather than kinetically controlled [1, 36].

Figure 2 shows DSC thermograms of benzoxazine and its mixtures with 16.7 mol% of accelerators in the temperature range from 20 to 350°C using heating rate of 20°C/min. The addition of accelerator significantly reduced the onset temperature of curing process, which was detected as an exothermic signal. This exothermic peak for the accelerated benzoxazine was broader than that for the unaccelerated benzoxazine, implying presence of multiple reactions during the curing process with accelerators. The presumed reaction pathways occurring in the presence of accelerators are drawn in Figure 1b–1e. Phenols, such as 4,4′-thiodiphenol and 4-mercaptophenol, can initiate oxazine ring opening and accelerate benzoxazine polymerization by the formation of an intermolecular hydrogen bond and subsequent reaction at the ortho position of the phenol or other benzoxazine molecule (Figure 1c). The other possible ring-opening mechanism is the initial protonation of benzoxazine, where protons behave as an actual catalyst. The protonation is followed by condensation reaction of the iminium species and the phenolate or other benzoxazine molecule to a phenolic structure (Figure 1b) [33]. The initiation by protonation or by intermolecular bond formation (hydrogen bond) can take place at either the nitrogen atom or the oxygen atom, but it was found, that in the case of protonation, the oxygen protonated species are reactive, whereas the nitrogen protonated species are stable [26] (Figure 1b).

On the other hand, imidazoles, such as 2-mercaptobenzimidazole, and aromatic amines, such as dianisidine, accelerate benzoxazine polymerization through the formation of an arylether structure (N,O-acetal-type linkage) [14, 34] (compound VI in Figure 1d). Formation of N,O acetal intermediate is present especially in the case of N-aryl-1,3-benzoxazines, before it rearranges to Mannich-type structure at higher temperatures. The arylether structure is thermally unstable and undergoes structural transformation to the phenolic-type with Mannich bridge ($–CH_2–NR–CH_2–$) at elevated temperature [1, 2].

Curing of benzoxazine with accelerators bearing thiol group is proposed to proceed according to Colbert reaction mechanism (Figure 1e) [37]. Initially the thiol proton protonates the nitrogen in oxazine ring. Then the sulfide attacks the adjacent methylene group located between the nitrogen and the oxygen. The thioether bond is created, which causes benzoxazine ring opening and phenolic hydroxyl group formation. The newly formed phenolic hydroxyl group of compound VII in Figure 1e is available for further reactions with benzoxazine.

3.2. Kinetic analysis

Kinetic analysis of non-isothermal resin-cured system is based on the rate equation and can be performed by the multiple heating rates [38, 39]. This method is attractive since the kinetic data can be obtained in short period of time. The rate of the curing process is considered to be a function of two variables, T and α (Equation (1)):

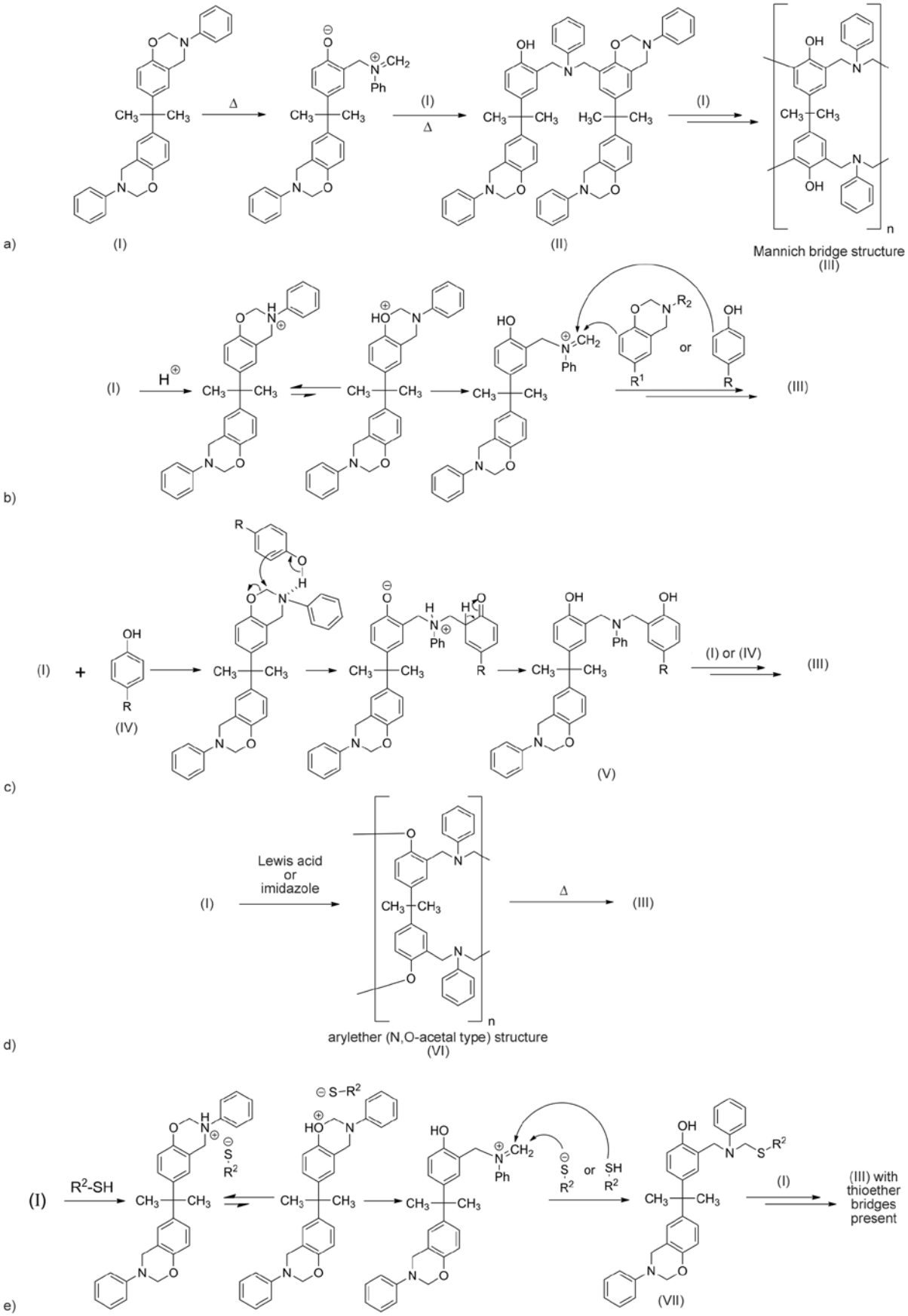

Figure 1. Possible pathways of benzoxazine polymerization and cross-linking, a) thermally accelerated ring-opening, b) ring-opening by protonation, c) ring-opening by hydrogen bond formation, d) polymerization through formation of an arylether structure (N,O-acetal-type linkage), e) Colbert reaction mechanism via two-step acid catalyzed nucleophilic addition

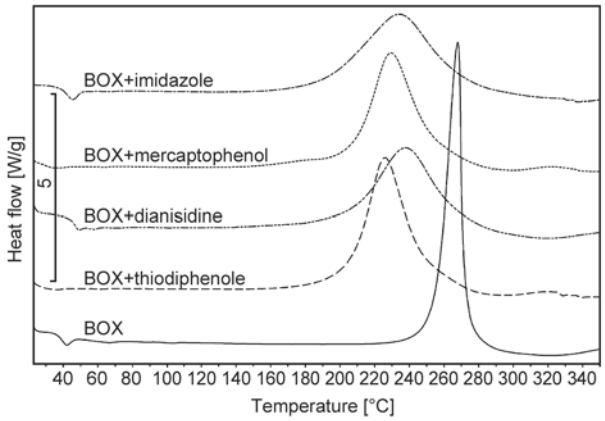

Figure 2. DSC thermograms of pure benzoxazine (BOX) and its mixtures with 16.7 mol% of selected accelerators in the temperature range from 20 to 350°C at a heating rate of 20°C/min

$$\frac{\mathrm{d}\alpha}{\mathrm{d}t} \equiv \beta\frac{\mathrm{d}\alpha}{\mathrm{d}T} = k(T)f(\alpha) \tag{1}$$

where $k(T)$ is a temperature-dependent reaction rate constant, $f(\alpha)$ is the reaction model, β is the heating rate in °C/min and $\mathrm{d}\alpha/\mathrm{d}t$ is the conversion rate in s^{-1}. Temperature dependence on rate constant is represented through the Arrhenius equation (Equation (2)):

$$k(T) = A\exp\left(-\frac{E_\mathrm{a}}{RT}\right) \tag{2}$$

where A is the pre-exponential factor in s^{-1}, E_a is the apparent activation energy in J/mol, R is the ideal gas constant in $J\cdot mol^{-1}\cdot K^{-1}$, and T is the absolute temperature in K. Four kinetic methods widely used in order to study dynamic kinetics of thermosetting polymers are Kissinger (Equation (3)), Ozawa (Equation (4)), Friedman (Equation (5)), and Flynn-Wall-Ozawa (Equation (6)) methods [40–43]:

$$\ln\left(\frac{\beta}{T_\mathrm{p}^2}\right) = \ln\left(\frac{Q_\mathrm{p}AR}{E_\mathrm{a}}\right) - \frac{E_\mathrm{a}}{RT_\mathrm{p}} \tag{3}$$

$$\ln\beta = \ln\left(\frac{AE_\alpha}{R}\right) - \ln F(\alpha) - 5.331 - 1.052\left(\frac{E_\alpha}{RT_p}\right) \tag{4}$$

$$\ln\frac{\mathrm{d}\alpha}{\mathrm{d}t} = \ln[Af(\alpha)] - \frac{E_\mathrm{a}}{RT} \tag{5}$$

$$\ln\beta = \ln\left(\frac{AE_\alpha}{R}\right) - \ln g(\alpha) - 5.331 - 1.052\left(\frac{E_\alpha}{RT}\right) \tag{6}$$

where $F(\alpha)$ is a constant function, $g(\alpha)$ is the integral conversion function, T_p is the peak temperature and $Q_p = [\mathrm{d}f(\alpha)/d\alpha]_{\alpha=\alpha p}$.

The results of calculated apparent activation energies by using the Kissinger and Ozawa methods (Table 1) showed that TDP was a superior accelerator in the studied system, since the activation energy was the lowest among the used accelerators. However, it has to be mentioned that calculated activation energies were only apparent, which is why pure BOX has lower activation energy than BOX/DA and BOX/MBI even though DA and MBI were labeled as accelerators. Such differences between the values with and without the accelerator can be expected, since the calculated value of E_a depends on how T_p value changes with heating rates for each of the studied systems. Therefore it is possible to obtain a higher E_a value for a system with lower T_p values. The peak temperatures of BOX/DA and BOX/MBI were lower than that of BOX, which may indicate that curing started at lower temperatures and DA and MBI really accelerate the curing process. Slightly higher activation energies may be observed by using Ozawa method in comparison to Kissinger method, though. Further on, the curing kinetic study was extended to isothermal conversion prediction using the method by Vyazovkin in order to complement the picture of kinetic studies.

3.3. Isothermal conversion prediction

In thermoset industry practice, it is of great importance to be able to predict the conversion of a material during the curing process. To predict the curing kinetics of a complex reaction system, such as benzoxazine/accelerator reaction systems, the use model-

Table 1. Apparent activation energies obtained from DSC experiments at various heating rates (β) for the BOX and BOX/accelerator formulations using Kissinger and Ozawa method

Accelerator	T_p [°C]				E_a [kJ/mol]	
	5°C/min	10°C/min	15°C/min	20°C/min	Kissinger	Ozawa
BOX	233	248	257	264	91,5	95,2
BOX/DA	218	227	232	238	137,9	139,0
BOX/MBI	210	223	231	238	92,7	96,0
BOX/MP	197	212	222	229	78,0	81,9
BOX/TDP	192	208	218	225	72,8	76,8

free isoconversional method developed by Vyazovkin [30–32] has been proposed. The isoconversional method enables simulation of the extent of reaction as a function of time in isothermal conditions using data obtained by dynamic experiments, without knowing the exact mechanism and individual reaction rate constants. Due to its proven great accuracy and wide applicability to any temperature program this approach has been widely used. In the applied isoconversional method the E_α value is determined as the value that minimizes the function (Equations (7) and (8)):

$$\Phi(E_\alpha) = \sum_{i=1}^{n} \sum_{j\neq 1}^{n} \frac{J[E_\alpha, T_i(t_\alpha)]}{J[E_\alpha, T_j(t_\alpha)]} = \min \tag{7}$$

$$J[E_\alpha, T_i(t_\alpha)] = \int_{t_{\alpha-\Delta\alpha}}^{t_\alpha} \exp\left[\frac{-E_\alpha}{RT_i(t)}\right] dt \tag{8}$$

where i and j denote different dynamic experiments, T is temperature in K, R is the ideal gas constant in J/(mol·K), E_α is apparent activation energy for a specific conversion α in J/mol, $\Delta\alpha$ is the small increment in α (usually around 0.02), $t\alpha$ and $t_{\alpha+\Delta\alpha}$ are reaction times up to α or $\Delta\alpha$, respectively. In this study, the integral J given in the Equation (2) was evaluated numerically from the experimental data by using trapezoidal rule. Repetition of minimization procedure in Equation (1) for each α resulted in the E_α-dependence. After knowing the E_α vs. α relationship, the isoconversional method can be used to predict isothermal kinetic conversion as a function of reaction time for different temperature programs with the use of Equation (9):

$$t_\alpha = \frac{\int_0^{t_\alpha} \exp\left(-\frac{E_\alpha}{RT(t_\alpha)}\right) dt}{\exp\left(-\frac{E_\alpha}{RT_0}\right)} \tag{9}$$

where t_α is the reaction time to a specific conversion α and T_0 is a fixed isothermal reaction temperature. t_α can be estimated by Equation (10) using results of dynamic experiment with a constant heating rate (β):

$$t_\alpha = \frac{\int_0^{T_\alpha} \exp\left(-\frac{E_\alpha}{RT}\right) dT}{\beta \exp\left(-\frac{E_\alpha}{RT_0}\right)} \tag{10}$$

Figure 3 compares conversion predictions for benzoxazine/accelerator mixtures with that of benzoxazine without accelerator at 140, 160, 180 and 200°C. As expected, at 140°C (Figure 3a) significantly higher conversions were predicted for curing with accelerators, which promote the ring-opening reaction. According to predictions (Figure 3a), the conversion without accelerator would be just little over 5% after 180 minutes at 140°C. By increasing the temperature the predicted conversion after 180 min was significantly increased. The result is straightforward, since higher temperature increases ring-opening reaction rate and the rate of hydroxyl group formation. Newly formed hydroxyl groups further accelerate the curing of benzoxazine through initiation by protonation and/or intermolecular bond formation as depicted in Figures 1b and 1c, respectively. Due to the fact that the ring-opening reaction is exclusively thermally initiated in the absence of an accelerator, the most evident difference in the progress of the conversion with increasing temperature is noticeable in this case (Figure 3).

With increasing curing temperature also the predicted conversions increased for all benzoxazine/accelerator mixtures as expected (Figure 3). The higher the temperature, the smaller the differences between benzoxazine/accelerator mixtures. Thiodiphenol (TDP) showed the best performance among the tested accelerators at 140°C. Thus at higher temperatures both accelerators of phenol type showed similar efficiency. Interestingly, at higher curing times, the MP efficiency became even higher than that of TDP. Moreover, by a detailed inspection of conversion curves in Figures 3a and 3b it may be noticed that the MP efficiency was higher also at the very beginning of the curing process. The observations may be explained by the fact that MP contains two different functional groups, which accelerate benzoxazine curing, i.e. a phenol and a thiol group, while TDP contains only phenol groups. Thus, curing with TDP follows the mechanisms depicted in Figures 1b and 1c, while curing with MP follows the mechanism depicted Figure 1e as well. At lower curing times, the better MP accelerating efficiency may be attributed to the relatively fast reaction of thiol group with oxazine ring. Since –SH groups are consumed during the reaction their accelerating effect diminishes with time. At the same time, the newly formed –OH group (compound VII in Figure 1e) is sterically hindered, but still possesses an acceleration capability. As the concentration of phenol –OH groups was higher when TDP, instead of MP, was used, the curing with TDP (through mechanisms

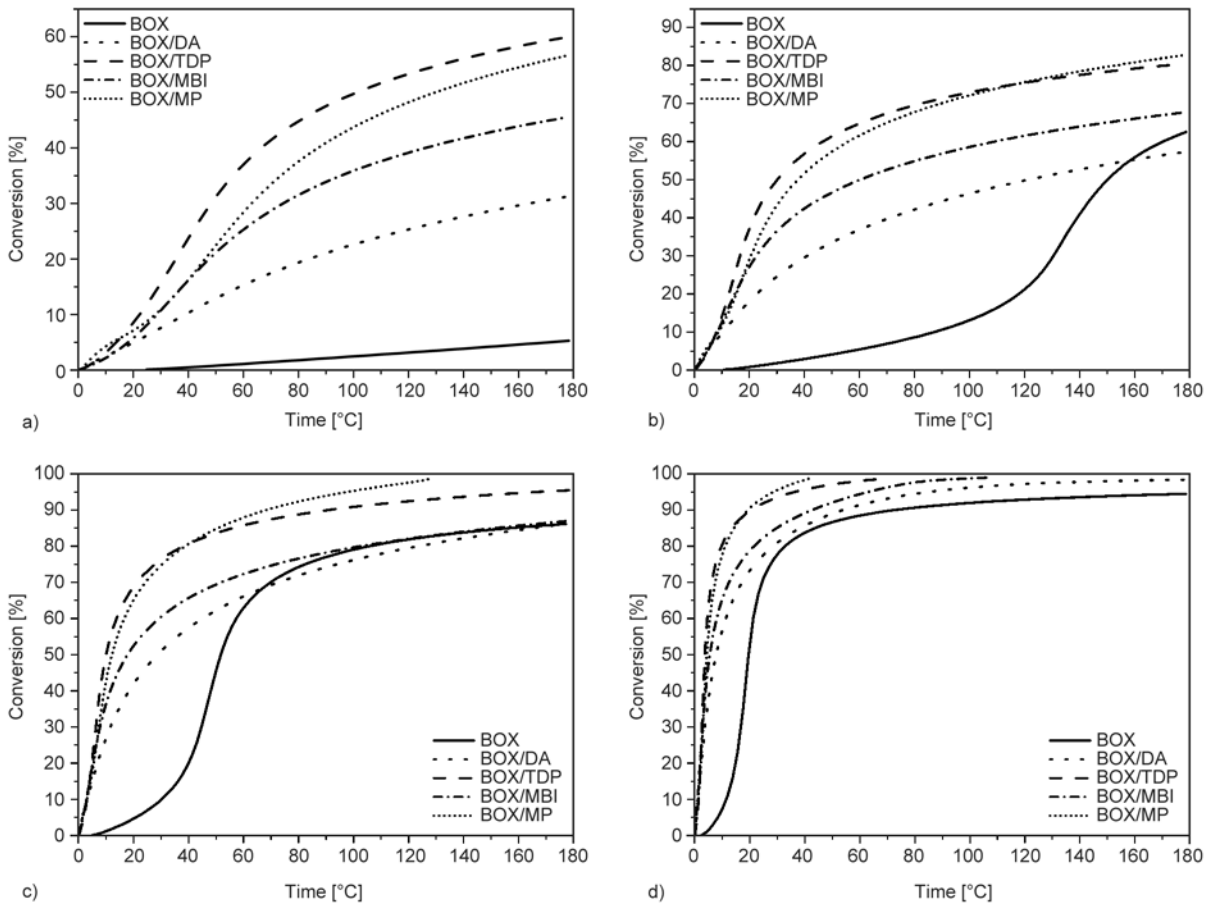

Figure 3. Conversion versus time at 140 (a), 160 (b), 180 (c) and 200°C (d) for benzoxazine (BOX) and its mixtures with different accelerators based on model-free isoconversional method

depicted in Figures 1b and 1c) proceeded faster after –SH groups of MP were consumed. However, at higher curing times, the conversion of curing with MP became higher again, which may be attributed to the higher cross-linking density of molecules V formed in reaction with TDP (due to larger number of reactive ortho sites on phenol). As mentioned before, a higher cross-linking density leads to lower molecular mobility and the process becomes diffusion-controlled.

By comparing conversion evolutions of benzoxazine (BOX) with those of its mixtures, where curing through the formation of an arylether structure (DA and MBI) was accelerated, an interesting phenomenon may be observed, which may be explained by already discussed reaction mechanisms again. When the acceleration proceeds through the mechanism shown in Figure 1d, N,O-acetal type structure is formed, which is without any hydroxyl groups. Consequently, the concentration of hydroxyl groups may be higher if no DA or MBI are added. The higher the concentration of –OH groups, the higher the rate of autocatalyzed curing reaction. Thus, it is possible that the thermally initiated benzoxazine curing becomes faster than curing through the formation of an arylether structure. Of course, this is unlikely at lower temperatures and reaction times. To our opinion, this effect is observable in Figures 3b and 3c, where BOX curves overcome BOX/DA curves and reach BOX/MBI curves. However, for simulations at 200°C, the conversion of BOX/DA and BOX/MBI is once again higher than that of BOX, presumably due to the fast transformation of molecule VI to the Mannich bridge structure III. The N,O-acetal structure is thermally unstable and after the breakdown of the molecule VI, hydroxyl groups are formed, which leads to the final molecule III and higher simulated conversions of BOX/DA and BOX/MBI than BOX (Figure 3d).

3.4. Curing behavior of benzoxazine using thiodiphenol as accelerator

The model-free kinetics analysis showed that thiodiphenol is the best choice among the tested accelerators. Acceleration with thiodiphenol is efficient and gives polybenzoxazine with enhanced cross-linked

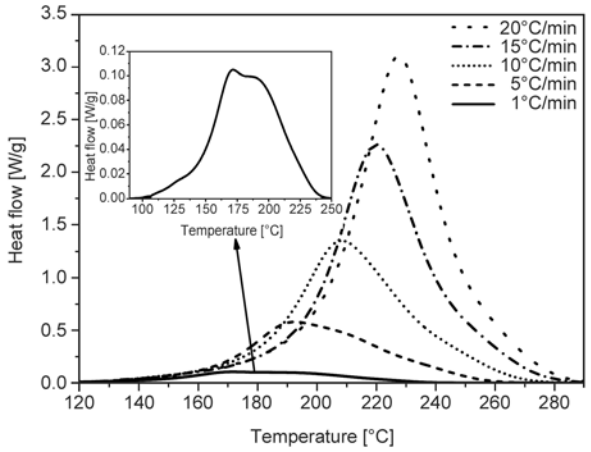

Figure 4. DSC thermograms of benzoxazine with 16.7 mol% of thiodiphenol at different heating rates

structure. DSC thermograms of mixtures containing 16.7 mol% of thiodiphenol obtained at different heating rates are shown in Figure 4. The exothermal signal of curing comprised of several overlapped peaks (Figure 4). The overlapping was more evident when lower heating rates were applied. This clearly indicated that the reaction of benzoxazine with thiodiphenol had at least two curing stages, which is in accordance with the known mechanisms of benzoxazine curing with phenolic accelerators [12, 13, 33, 34]. The lower the heating rate, the more noticeable the boundary between the reactions stages. Nevertheless, the heating rate showed no effect on the total exothermic reaction heat estimated from the area under the overlapped peaks. The average total exothermic reaction heat was 370 J/g.

To investigate the curing stages further on, the effect of thiodiphenol amount on the curing was studied. Additional DSC experiments at fixed heating rate of 1°C/min were performed. At such a slow heating rate the effect of the accelerator on the progress of the curing was clearly observable. As it can be seen in Figure 5 the amount of thiodiphenol had the greatest impact on the initial stage of the reaction, which was the oxazine ring opening (formation of compound II in Figure 1a). The next process, related to the polymerization and cross-linking (formation of final cured compound III in Figure 1a), was not affected to the same degree.

DSC peaks fitting and deconvolution (Figure 5) was performed by the OriginPro program using the Pearson VII distribution, which gave best DSC peaks fitting and deconvolution results. In the case of benzoxazine without accelerator (Figure 5a) the two deconvoluted peaks may be associated with the thermally accelerated ring-opening accompanied by autocatalytic reaction (Δ in Figure 5) and the diffusion-controlled step in curing reaction (□ in Figure 5), respectively. The reaction of thermally accelerated ring-opening is shown in Figure 1a and results in formation of compound II. The autocatalytic reaction, which mechanism is the same as depicted in Figure 1c, involves the catalysis of ring-opening reaction by hydrogen bond formation between hydroxyl group of the compound II and other benzoxazine molecule. The diffusion-controlled step comprises same reactions but the mobility of molecules is hindered. Most likely, the sterical hindrance prevents the autocatalytic ring-opening reaction through hydrogen bond formation at this stage.

On the other hand, for mixtures with thiodiphenol, another peak (○ in Figure 5) emerged during the fitting process. Since the new peak emerged at the beginning of the curing process it was assigned to the accelerated oxazine ring opening (mechanisms presented in Figures 1b and 1c). With increasing the amount of the accelerator the peak shifted to lower temperatures and became even more noticeable. Note, the deconvoluted peak (marked as Δ), assigned to the autocatalytic reaction, associated to the benzoxazine hydroxyl groups, is still present in Figures 5b, 5c, and 5d. In the case of the highest amount of the accelerator (Figure 5d) the peak of the diffusion-controlled step disappeared, which may be explained by involvement of smaller accelerators molecules in the curing reactions. Based on this observation it may be deducted that the formation of compounds V (Figure 1c) is more favorable than the formation of compounds II and/or III. Furthermore, it is possible to conclude that the reaction of benzoxazine with thiodiphenol leads to products of lower cross-linking density.

4. Conclusions

The influence of phenolic, mercapto, amino and imidazole accelerators on the benzoxazine curing process was studied and discussed in detail. The model-free kinetics analysis of DSC data showed that thiodiphenol is the best choice among the tested accelerators. In order to investigate the curing of benzoxazine/thiodiphenol mixture in detail the accelerator amount was varied. By low heating rate DSC analysis exothermic signals of curing, composed of several overlapped peaks, were obtained. The peaks were sensibly associated to catalytic ring-opening,

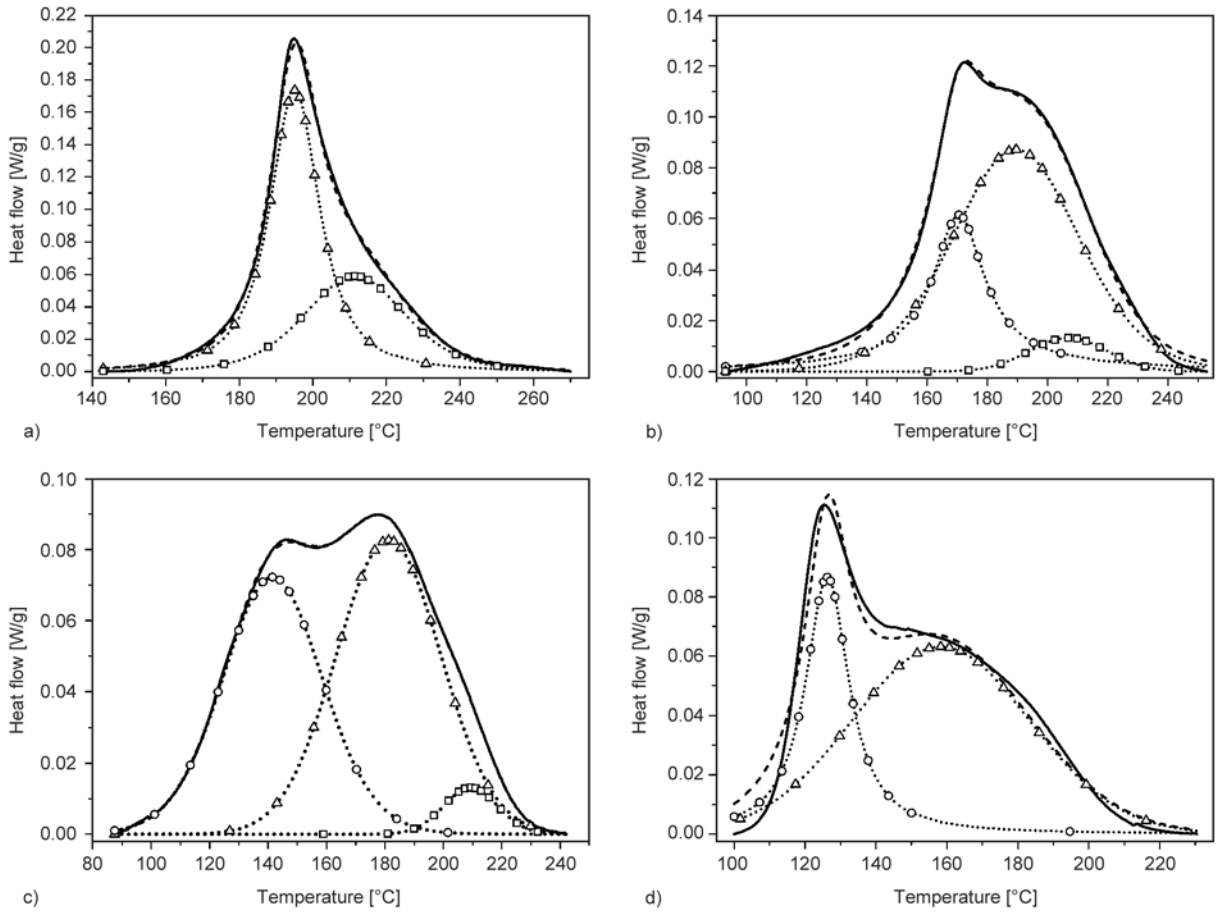

Figure 5. DSC curing peaks (solid line) and peaks obtained by deconvolution (dashed lines) for benzoxazine (BOX) with different amount of thiodiphenol ((a) 0, (b) 5, (c) 20, (d) 50 wt%. Peak assignment: thermally accelerated ring-opening and autocatalytic reaction (Δ), diffusion-controlled step (□), catalytic ring-opening (○).

thermally accelerated ring-opening and to the diffusion-controlled step. The amount of added accelerator affected particularly the ring-opening and diffusion-controlled steps. The kinetic regime in the diffusion-controlled step was dominated by cross-linking density of benzoxazine resin, which is also dependent on the accelerator amount and functionality.

Acknowledgements

The financial support of this work by the Slovenian Ministry of Higher Education, Science and Technology (Grant P2-0191) is gratefully acknowledged.

References

[1] Ishida H., Rodriguez Y.: Catalyzing the curing reaction of a new benzoxazine-based phenolic resin. Journal of Applied Polymer Science, **58**, 1751–1760 (1995). DOI: 10.1002/app.1995.070581013

[2] Ning X., Ishida H.: Phenolic materials via ring-opening polymerization of benzoxazines: Effect of molecular structure on mechanical and dynamic mechanical properties. Journal of Polymer Science Part B: Polymer Physics, **32**, 921–927 (1994). DOI: 10.1002/polb.1994.090320515

[3] Ishida H., Allen D. J.: Mechanical characterization of copolymers based on benzoxazine and epoxy. Polymer, **37**, 4487–4495 (1996). DOI: 10.1016/0032-3861(96)00303-5

[4] Ishida H., Allen D. J.: Physical and mechanical characterization of near-zero shrinkage polybenzoxazines. Journal of Polymer Science Part B: Polymer Physics, **34**, 1019–1030 (1996). DOI: 10.1002/(sici)1099-0488(19960430)34:6<1019::aid-polb1>3.0.co;2-t

[5] Ishida H., Low H. Y.: A study on the volumetric expansion of benzoxazine-based phenolic resin. Macromolecules, **30**, 1099–1106 (1997). DOI: 10.1021/ma960539a

[6] Grishchuk S., Mbhele Z., Schmitt S., Karger-Kocsis J.: Structure, thermal and fracture mechanical properties of benzoxazine-modified amine-cured DGEBA epoxy resins. Express Polymer Letters, **5**, 273–282 (2011). DOI: 10.3144/expresspolymlett.2011.27

[7] Grishchuk S., Schmitt S., Vorster O. C., Karger-Kocsis J.: Structure and properties of amine-hardened epoxy/benzoxazine hybrids: Effect of epoxy resin functionality. Journal of Applied Polymer Science, **124**, 2824–2837 (2012).
DOI: 10.1002/app.35302

[8] Grishchuk S., Sorochynska L., Vorster O. C., Karger-Kocsis J.: Structure, thermal, and mechanical properties of DDM-hardened epoxy/benzoxazine hybrids: Effects of epoxy resin functionality and ETBN toughening. Journal of Applied Polymer Science, **127**, 5082–5093 (2013).
DOI: 10.1002/app.38123

[9] Jin L., Agag T., Ishida H.: Bis(benzoxazine-maleimide)s as a novel class of high performance resin: Synthesis and properties. European Polymer Journal, **46**, 354–363 (2010).
DOI: 10.1016/j.eurpolymj.2009.09.013

[10] Wang J., Fang X., Wu M-Q., He X-Y., Liu W-B., Shen X-D.: Synthesis, curing kinetics and thermal properties of bisphenol-AP-based benzoxazine. European Polymer Journal, **47**, 2158–2168 (2011).
DOI: 10.1016/j.eurpolymj.2011.08.005

[11] Low H. Y., Ishida H.: An investigation of the thermal and thermo-oxidative degradation of polybenzoxazines with a reactive functional group. Journal of Polymer Science Part B: Polymer Physics, **37**, 647–659 (1999).
DOI: 10.1002/(sici)1099-0488(19990401)37:7<647::aid-polb16>3.0.co;2-1

[12] Wang Y-X., Ishida H.: Cationic ring-opening polymerization of benzoxazines. Polymer, **40**, 4563–4570 (1999).
DOI: 10.1016/S0032-3861(99)00074-9

[13] Dunkers J., Ishida H.: Reaction of benzoxazine-based phenolic resins with strong and weak carboxylic acids and phenols as catalysts. Journal of Polymer Science Part A: Polymer Chemistry, **37**, 1913–1921 (1999).
DOI: 10.1002/(sici)1099-0518(19990701)37:13<1913::aid-pola4>3.0.co;2-e

[14] Sudo A., Kudoh R., Nakayama H., Arima K., Endo T.: Selective formation of poly(*N*,*O*-acetal) by polymerization of 1,3-benzoxazine and its main chain rearrangement. Macromolecules, **41**, 9030–9034 (2008).
DOI: 10.1021/ma8013178

[15] Andreu R., Reina J. A., Ronda J. C.: Carboxylic acid-containing benzoxazines as efficient catalysts in the thermal polymerization of benzoxazines. Journal of Polymer Science Part A: Polymer Chemistry, **46**, 6091–6101 (2008).
DOI: 10.1002/pola.22921

[16] Andreu R., Espinosa M. A., Galià M., Cádiz V., Ronda J. C., Reina J. A.: Synthesis of novel benzoxazines containing glycidyl groups: A study of the crosslinking behavior. Journal of Polymer Science Part A: Polymer Chemistry, **44**, 1529–1540 (2006).
DOI: 10.1002/pola.21255

[17] Kim H-D., Ishida H.: Study on the chemical stability of benzoxazine-based phenolic resins in carboxylic acids. Journal of Applied Polymer Science, **79**, 1207–1219 (2001).
DOI: 10.1002/1097-4628(20010214)79:7<1207::aid-app80>3.0.co;2-3

[18] Chow W. S., Grishchuk S., Burkhart T., Karger-Kocsis J.: Gelling and curing behaviors of benzoxazine/epoxy formulations containing 4,4′-thiodiphenol accelerator. Thermochimica Acta, **543**, 172–177 (2012).
DOI: 10.1016/j.tca.2012.05.015

[19] Jang J., Shin S.: Cure studies of a benzoxazine-based phenolic resin by isothermal experiment. Polymer Journal, **27**, 601–606 (1995).
DOI: 10.1295/polymj.27.601

[20] Shi Z., Yu D., Wang Y., Xu R.: Nonisothermal cure kinetics in the synthesis of polybenzoxazine–clay nanocomposites. Journal of Applied Polymer Science, **88**, 194–200 (2003).
DOI: 10.1002/app.11640

[21] Su Y-C., Yei D-R., Chang F-C.: The kinetics of B-a and P-a type copolybenzoxazine via the ring opening process. Journal of Applied Polymer Science, **95**, 730–737 (2005).
DOI: 10.1002/app.21244

[22] Yei D-R., Fu H-K., Chen W-Y., Chang F-C.: Synthesis of a novel benzoxazine monomer-intercalated montmorillonite and the curing kinetics of polybenzoxazine/clay hybrid nanocomposites. Journal of Polymer Science Part B: Polymer Physics, **44**, 347–358 (2006).
DOI: 10.1002/polb.20693

[23] Santhosh Kumar K. S., Reghunadhan Nair C. P., Ninan K. N.: Rheokinetic investigations on the thermal polymerization of benzoxazine monomer. Thermochimica Acta, **441**, 150–155 (2006).
DOI: 10.1016/j.tca.2005.12.007

[24] Jubsilp C., Punson K., Takeichi T., Rimdusit S.: Curing kinetics of benzoxazine–epoxy copolymer investigated by non-isothermal differential scanning calorimetry. Polymer Degradation and Stability, **95**, 918–924 (2010).
DOI: 10.1016/j.polymdegradstab.2010.03.029

[25] Jubsilp C., Damrongsakkul S., Takeichi T., Rimdusit S.: Curing kinetics of arylamine-based polyfunctional benzoxazine resins by dynamic differential scanning calorimetry. Thermochimica Acta, **447**, 131–140 (2006).
DOI: 10.1016/j.tca.2006.05.008

[26] Chutayothin P., Ishida H.: Cationic ring-opening polymerization of 1,3-benzoxazines: Mechanistic study using model compounds. Macromolecules, **43**, 4562–4572 (2010).
DOI: 10.1021/ma901743h

[27] Santhosh Kumar K. S., Reghunadhan Nair C. P., Ninan K. N.: Investigations on the cure chemistry and polymer properties of benzoxazine–cyanate ester blends. European Polymer Journal, **45**, 494–502 (2009).
DOI: 10.1016/j.eurpolymj.2008.11.001

[28] Santhosh Kumar K. S., Reghunadhan Nair C. P., Sadhana R., Ninan K. N.: Benzoxazine–bismaleimide blends: Curing and thermal properties. European Polymer Journal, **43**, 5084–5096 (2007).
DOI: 10.1016/j.eurpolymj.2007.09.012

[29] Jayamohan Das D. L., Rayeev R., Rajeev R. S., Santhosh Kumar K. S.: Synthesis, characterization, curing and thermal decomposition kinetics of bisphenol-A based polybenzoxazine. International Journal of Scientific and Technology Research, **2**, 146–155 (2013).

[30] Vyazovkin S., Dollimore D.: Linear and nonlinear procedures in isoconversional computations of the activation energy of nonisothermal reactions in solids. Journal of Chemical Information and Computer Sciences, **36**, 42–45 (1996).
DOI: 10.1021/ci950062m

[31] Vyazovkin S.: Evaluation of activation energy of thermally stimulated solid-state reactions under arbitrary variation of temperature. Journal of Computational Chemistry, **18**, 393–402 (1997).
DOI: 10.1002/(SICI)1096-987X(199702)18:3<393::AID-JCC9>3.0.CO;2-P

[32] Vyazovkin S.: Modification of the integral isoconversional method to account for variation in the activation energy. Journal of Computational Chemistry, **22**, 178–183 (2001).
DOI: 10.1002/1096-987X(20010130)22:2<178::AID-JCC5>3.0.CO;2-#

[33] Riess G., Schwob J. M., Guth G., Roche M., Laude B.: Ring opening polymerization of benzoxazines – A new route to phenolic resins. in 'Advances in polymer synthesis' (eds.: Culbertson B., McGrath J.) Springer, New York, Vol 31, 27–49 (1985).
DOI: 10.1007/978-1-4613-2121-7_2

[34] Wang Y-X., Ishida H.: Synthesis and properties of new thermoplastic polymers from substituted 3,4-dihydro-2*H*-1,3-benzoxazines. Macromolecules, **33**, 2839–2847 (2000).
DOI: 10.1021/ma9909096

[35] Liu C., Shen D., Sebastián R. M., Marquet J., Schönfeld R.: Catalyst effects on the ring-opening polymerization of 1,3-benzoxazine and on the polymer structure. Polymer, **54**, 2873–2878 (2013).
DOI: 10.1016/j.polymer.2013.03.063

[36] Vyazovkin S., Sbirrazzuoli N.: Isoconversional kinetic analysis of thermally stimulated processes in polymers. Macromolecular Rapid Communications, **27**, 1515–1532 (2006).
DOI: 10.1002/marc.200600404

[37] Musa A., Kiskan B., Yagci Y.: Thiol-benzoxazine chemistry as a novel Thiol-X reaction for the synthesis of block copolymers. Polymer, **55**, 5550–5556 (2014).
DOI: 10.1016/j.polymer.2014.06.076

[38] Málek J.: The kinetic analysis of non-isothermal data. Thermochimica Acta, **200**, 257–269 (1992).
DOI: 10.1016/0040-6031(92)85118-F

[39] Vyazovkin S., Burnham A. K., Criado J. M., Pérez-Maqueda L. A., Popescu C., Sbirrazzuoli N.: ICTAC Kinetics Committee recommendations for performing kinetic computations on thermal analysis data. Thermochimica Acta, **520**, 1–19 (2011).
DOI: 10.1016/j.tca.2011.03.034

[40] Kissinger H. E.: Reaction kinetics in differential thermal analysis. Analytical Chemistry, **29**, 1702–1706 (1957).
DOI: 10.1021/ac60131a045

[41] Friedman H. L.: Kinetics of thermal degradation of char-forming plastics from thermogravimetry. Application to a phenolic plastic. Journal of Polymer Science Part C: Polymer Symposia, **6**, 183–195 (1964).
DOI: 10.1002/polc.5070060121

[42] Ozawa T.: A new method of analyzing thermogravimetric data. Bulletin of the Chemical Society of Japan, **38**, 1881–1886 (1965).
DOI: 10.1246/bcsj.38.1881

[43] Sbirrazzuoli N., Girault Y., Elégant L.: Simulations for evaluation of kinetic methods in differential scanning calorimetry. Part 3 – Peak maximum evolution methods and isoconversional methods. Thermochimica Acta, **293**, 25–37 (1997).
DOI: 10.1016/S0040-6031(97)00023-3

eXPRESS Polymer Letters Vol.9, No.7 (2015) 658–670
Available online at www.expresspolymlett.com
DOI: 10.3144/expresspolymlett.2015.61

Anisotropy and compression/tension asymmetry of PP containing soft and hard particles and short glass fibers

A. M. Hartl[1], *M. Jerabek*[2*], *R. W. Lang*[1]

[1]Institute of Polymeric Materials and Testing, Johannes Kepler University Linz, Altenberger Strasse 69, 4040 Linz, Austria
[2]Borealis Polyolefine GmbH, St.-Peter Str. 25, 4021 Linz, Austria

Received 17 November 2014; accepted in revised form 19 February 2015

Abstract. Polypropylene (PP) composites are used in a wide range of structural applications. Except for fiber reinforced PP, most PP particle composites are commonly considered to be isotropic or at least quasi-isotropic. In this paper, however, the anisotropy of several PP composites containing soft (rubber) and hard (talc) particles and glass fibers is characterized in detail in terms of the material microstructure as well as the resulting mechanical properties in monotonic tensile and compressive experiments. The microstructural investigations showed that all composites displayed a certain surface-core layer structure of distinctly different orientation patterns and with a higher degree of orientation in the surface layer. Also in mechanical testing an anisotropic behavior was observed with the degree of anisotropy being more pronounced in tension than compression. Moreover, the compression/tension asymmetry also strongly depends on filler type and orientation.

Keywords: *polymer composites, mechanical properties, anisotropy, polypropylene*

1. Introduction

The property profile of polypropylene homo and hetero (multi-phase) systems can be tailored to meet a wide range of demands with regard to processing (e.g. dimensional stability), thermal and mechanical properties (impact vs. stiffness). Combined with cost advantages over other polymers, polypropylenes (along with polyethylenes) therefore hold the highest market share among all plastics. By addition of fillers and reinforcements, typically engineering and specialty plastics markets, such as for example in the automotive industry, increasingly opt for tailor-made polypropylene (PP) solutions. In terms of mechanical property optimization, the resistance against impact and deformation (i.e. stiffness) are of prime importance in many structural components [1]. The impact behavior is commonly modified by copolymerization with ethylene units or by rubber toughening via compounding [2]. The stiffness in turn can be increased by the addition of stiff, mineral particles like talc (most widely used), mica and calcium carbonate, which also reduce the cost of the composite [1]. In the higher price segment, short and long glass fibers offer the possibility of simultaneously increasing the toughness and stiffness of brittle PP. In the context of this paper the term 'filler' is used to encompass all of these different constituents. More recently, also so called ternary or hybrid composites have gained increasing attention in the scientific community, opting for a synergistic effect of the three component materials (e.g. PP with fibers and rubber particles or PP with hard particles and rubber particles) on properties and/or cost reduction [3–12].

During compounding and especially during final part shaping in injection molding and extrusion pro-

*Corresponding author, e-mail: michael.jerabek@borealisgroup.com

cessing, the spatial arrangement of the fillers is controlled by the local conditions of the melt flow. Differences in viscosity and/or high aspect ratios of the filler can lead to a preferential orientation in melt flow direction. More precisely, the resulting shape and/or spatial distribution and the orientation of the filler is a function of the conditions during processing (e.g. temperature and shear rate), the composition of the composite, the interface interaction and – in the case of rubber additions – the ratio of rubber and matrix viscosity [13–16]. Especially for discontinuous fiber reinforced polymers numerous efforts have been undertaken to analytically and numerically investigate and describe the orientation distribution by means of melt flow analysis [17–20]. In most shell like parts, a pronounced layer structure in terms of preferred orientations develops during melt injection. In this context it is well known, that typically particles and fibers in tool wall vicinity are oriented mainly in or at small angles to the flow direction due to shear gradient effects and mostly perpendicular (again with angle variations) to the flow direction in the core layer due to extensional flow effects [14, 17, 18, 21, 22]. The orientation of the filler in turn has an effect on the preferred crystallization direction due to trans-crystallization effects on the filler surface, displaying higher values for higher degrees of particle orientation [21, 23, 24]. Yet, for talc and calcium carbonate filled PP, Pukánszky *et al.* [25] showed that the anisotropy introduced by the particle and not that of the polymer crystals governs the mechanical behavior.

While the orientation dependent properties of fiber reinforced polymers has been the topic of numerous investigations [18, 26–28], rather little data has been published for other types of particle reinforced composites typically with smaller aspect ratios. Exemplary for rubber, Wang *et al.* [14] found a strong dependence of the impact properties on the orientation of the rubber. For talc, Díez-Gutiérrez *et al.* [29] reported a pronounced anisotropic behavior in dynamic mechanical analysis of PP talc composites. Furthermore, Kunkel *et al.* [30] characterized the anisotropy in tensile tests and considered this in the material model for FEM analysis.

Thus, the focus of the research reported in this paper was to characterize the anisotropy in tension and compression experiments along with the resulting compression/tension asymmetry of a variety of PP composites. Various types of soft and hard particle and short glass fiber composites were injection molded with equivalent processing parameters (similar thermal history) into a specially designed tool, which has proven to introduce a high and uniform fiber orientation distribution (FOD) in short glass fiber (sgf) reinforced PP. Consequently, the tensile and compressive stress-strain behavior of these composites with filler orientation in and perpendicular to the loading direction were characterized. Emphasis was placed on the anisotropic and asymmetric tension/compression behavior in terms of initial deformation behavior (*E*-modulus and Poisson's ratio), volumetric deformation evolution (Poisson's ratio trends) and ultimate failure properties (strength values).

2. Experimental

2.1. Materials and specimens

In addition to the neat PP matrix, a total 5 composites with this PP matrix were studied in the present paper. These include (1) composite filled with 32 m% soft particle (rubber, PP-R32), (2) and (3) composites filled with soft and hard particle with two different ratios of filler content (rubber and talc platelets, PP-R(m%)-T(m%)) and (4) and (5) short glass fiber reinforced composites with 32 m% glass fibers with different fiber length distributions (PP-sgf32-1 and sgf32-2). In Table 1, details on the material designation of the PP/filler compounds along with information on the composition and the filler shape and fiber aspect ratio after injection molding are provided. The two sgf materials differ in their aspect ratio by about 30%. The PP-sgf32-1 material was the commercial Fibremod™ GD301FE grade, whereas all

Table 1. Material designation of the PP based materials along with information on the composition and the filler shape and fiber aspect ratio

Composite types: PP filled with		**Rubber**	**Rubber and talc**		**Short glass fiber**	
Material designation and filler characteristics		PP-R32	PP-R27-T10	PP-R12-T32	PP-sgf32-1	PP-sgf32-2
Rubber	content shape	32 w%	27 w%	12 w%		
		elliptic shape				
Talc	content shape		10 w% platelet	32 w% platelet		
Glass fibers	content aspect ratio				32 w% 23	32 w% 32

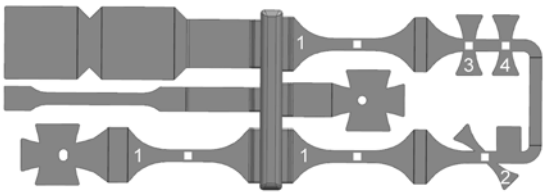

Figure 1. Tool used for injection molding of composites with differing particle orientation (thickness of all specimen sections 2 mm)

other composites are experimental grades (all supplied by Borealis Polyolefine GmbH; Linz, Austria).
A novel quasi-unidirectional (UD) tool, originally developed to obtain specimens with a wide range of glass fiber orientations (for further details see [31]) was used for injection molding (see Figure 1). To enhance and maximize the degree of shear-flow induced orientation, the thickness of the tool cavity is 2 mm. The tool thus allows to directly mill out the specimens for 0 and 90° testing used in this investigation.

2.2. Characterization of morphology and microstructure

For the characterization of the microstructure, scanning electron microscopy (SEM) investigations, wide angle X-ray scattering (WAXS) experiments and μ-CT measurements were conducted. In terms of sample preparation for SEM, the melt flow direction (MFD) - specimen thickness (*x*–*z*) plane of the 0° specimens filled with rubber and talc were first cut by a cryo-microtome, consequently etched by n-heptane and $KMnO_4$, respectively, and analyzed. While the rubber particles displayed sufficient contrast in the standard imaging mode based on secondary electrons to both the matrix and also the talc particles, backscattered electrons were detected in order to assess the orientation of the talc particles. The aspect ratio (major/minor length) in melt flow direction (MFD, for the 0° specimens this corresponds to the testing direction) of the rubber particles and the orientation angle in MFD with respect to the tool wall of the talc particles were automatically evaluated by an image processing Matlab based software script based. As quantitative measure for the talc particle orientation, the Herman's orientation factor f_H was calculated based on the measured orientation angle ϕ according to Equation (1) [32, 33]:

$$f_H = \frac{3\cdot(\cos^2\phi) - 1}{2} \tag{1}$$

with an f_H value of 1 and –0.5 indicating perfect orientation in and perpendicular to the MFD (and correspondingly the testing direction), respectively.
Furthermore, WAXS was used to assess the crystalline orientation and the corresponding Herman's orientation factors (for details see [34]). The orientation of the glass fibers in the sgf reinforced PP material was assessed in a Nanotom (GE Phoenix|X-ray, Wunstorf, Germany) μ-CT device at a resolution of 2 μm voxel edge length. Scan parameters were set such that contrast and data quality was optimized. The 3D data was analyzed by an automatic software pipeline (for further details see [31, 35]).

2.3. Mechanical testing and data reduction

All mechanical tests were conducted at a strain rate of 0.001 s^{-1} and at 23°C. The tensile testing was performed on a universal screw-driven test machine of the type Zwick Z020 (Zwick GmbH & Co. KG; Ulm, Germany). In compression testing of plastics according ISO 604, the load should be introduced by compression plates and specimen thickness should be 4 mm. As discussed above, a high degree of crystalline, particle and fiber orientation is only achievable for specimen with smaller specimen thickness (due to increased shear flow contribution). Thus in this investigation compressive loads were introduced by highly aligned clamping jaws on an Instron ElectroPuls E10000 (Instron, Norwood, USA). The clamping length was set to 9 mm in order to avoid failure by buckling. Indeed, no out of plane displacement was observed and all specimens failed in a shear mode (as also cross-checked via digital image correlation (DIC); see below).
For all tension and compression tests, the longitudinal force, the full-field strain on the front surface (*x* and *y* direction) and also on the side surface of the specimen (*x* and *z* direction) were measured by means of DIC with two cameras (ARAMIS 12M by GOM, Gesellschaft für optische Messtechnik mbH; Braunschweig, Germany). Both cameras were triggered at exactly the same time instances. This additional test effort was undertaken as for transversely anisotropic materials the strains in *y* and *z* direction differ. Further details as to the DIC test method and data reduction including the evaluation of true stresses and strains [36] are given elsewhere.

3. Results and discussion

An overview of the effect of the different fillers on the deformation and failure behavior in terms of tensile elastic modulus versus tensile strength along with a first indication of the variation of mechanical properties due to particle orientation is depicted in Figure 2. For comparison the neat PP matrix properties are also illustrated in the diagram. As discussed above, by addition of glass fibers the modulus and strength of PP can be significantly increased. In the following subsections, first the crystalline and filler orientation is assessed and described as basis for further discussions. Subsequently, the anisotropy (as defined by the ratio of the 0° specimen to 90° specimen properties) in terms of modulus and strength in tension and compression and the anisotropy in the compression/tension asymmetry (as represented by the ratio of compressive to tensile strength) is discussed. The differences in the deformation behavior on a micro-scale are then analyzed in terms of Poisson's ratio trends in the final subsection.

3.1. Morphology and microstructure

On a nanoscopic fine scale, even the neat matrix itself may be considered as a composite of rigid crystalline lamellar and soft amorphous interlamellar regions. The orientation of the crystals was characterized by WAXS for selected specimens, and the Herman's orientation factors of the lamellas were deduced and are provided in Table 2. Since the orientation of the fillers has a more pronounced effect on the mechanical properties (as mentioned above), further focus is on the orientation of (1) the rubber, (2) the talc particles and (3) the short glass fibers. Regarding the first, the aspect ratio of the rubber with the major axis in melt flow direction and the minor axis in specimen thickness direction was taken as a parameter for the orientation, with a value of 1 (spherical) characterizing the unoriented state and values >1 (elliptical) an orientated state with a primary orientation in MFD. In good agreement with literature observations (e.g. [16] for rubber, [17, 18] for sgf polymers), a five layer structure consisting of two outer skin layers at the specimen surface, two surface layers positioned beneath the outer skin and a central core layer was detected across the specimen thickness direction (see Figure 3). The filler orientation reflects the local conditions of shear flow in surface near regions (higher degree of orientation) versus elongational flow in the core region (lower degree of orientation). By adding talc, the overall viscosity is increased. On a local scale, however, the shear rate in the inter-particle region is increased and due to the non-Newtonian behavior of the matrix the viscosity decreases [37]. These two effects could possibly be the cause for the higher degree of orientation of the rubber particles observed in the talc filled PP matrix compared to the neat PP matrix.

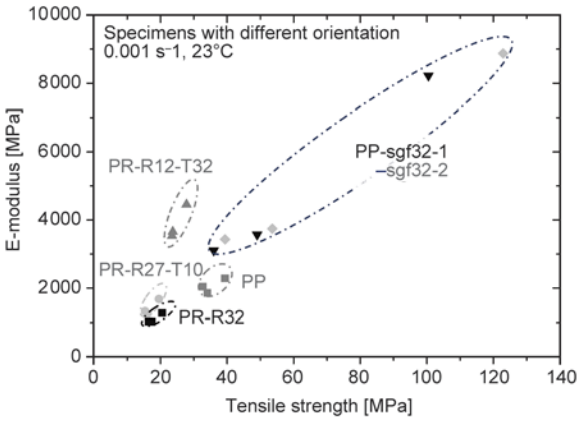

Figure 2. Overall illustration of mechanical anisotropy of all materials investigated in terms of tensile *E*-modulus versus tensile strength; the elliptical envelopes for the various materials indicate the property range covered by orientation effects as measured with 0° (highest values), 45° and 90° (lowest values) specimens

In an analogous manner, the talc particles also display a decreasing degree of orientation towards the specimen center, as represented by the Herman's orientation factor. This trend is more pronounced for the material with the higher talc content (see Figure 4). These findings are in good agreement with results presented by Pukánszky *et al.* [25], who also reported a decreasing talc orientation with increasing filler content for PP talc composites.

Turning now to the short glass fiber reinforced materials PP-sgf32-1 and -2, the first entry of the orientation tensor A_{11} is shown in Figure 5a again as a function of the specimen thickness. In this context, values for A_{11} of 1 and 0, respectively, indicate perfect fiber orientation in and perpendicular to the MFD. Apart from the skin layer (first 200 μm), only a slightly higher degree of orientation is observed in the surface layer than in the core layer. It should be noted, however, that the injection molding tool used was explicitly designed to reduce the layer structure and to achieve a high average fiber orientation across the entire specimen thickness (for further details see [31]). For the same reason, the local degree of fiber orientation (and hence the average degree of fiber

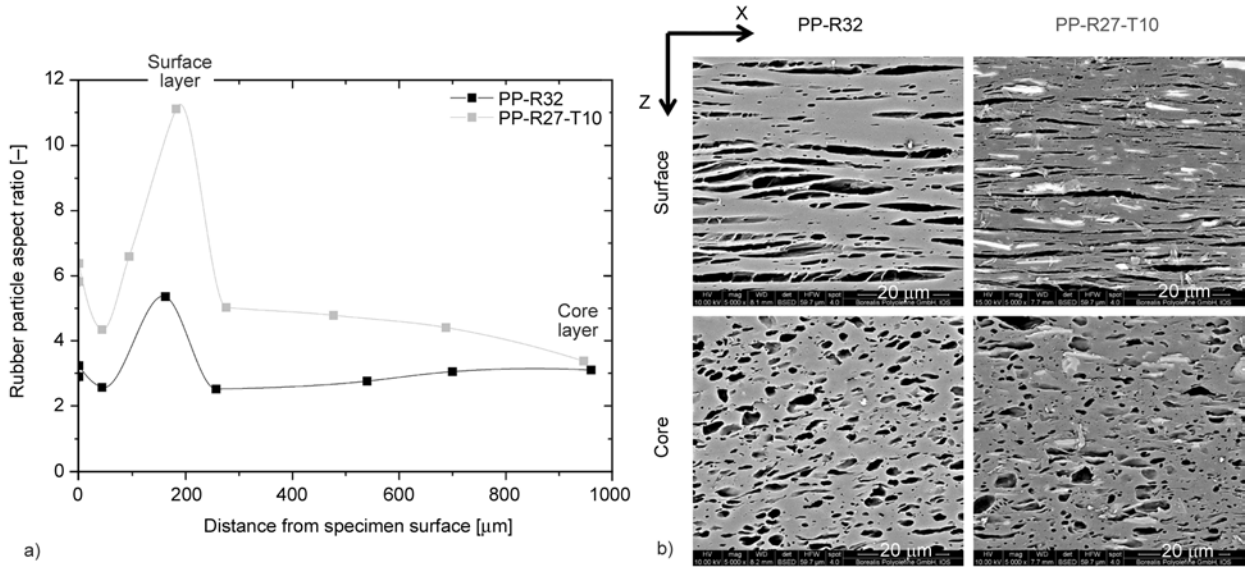

Figure 3. Rubber particle aspect ratio (indicative of orientation effects) as a function of the distance from the specimen surface (covering half of the specimen thickness) comparing PP-R32 and PP-R27-T10 (a), and corresponding SEM pictures taken from the surface and core layer, respectively, with dark regions representing the rubber particles (b)

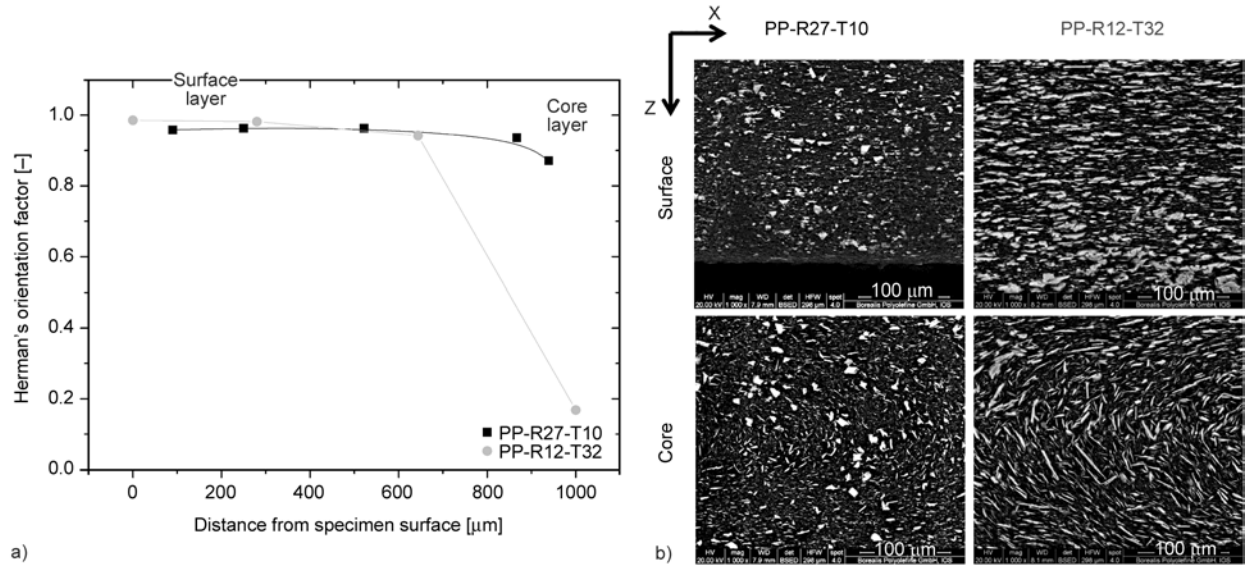

Figure 4. Herman's orientation factor of the talc particles as a function of the distance from the specimen surface (covering half of the specimen thickness) comparing PP-R27-T10 and PP-R12-T32 (a) and corresponding SEM pictures taken from the surface and core layer, respectively (b); bright platelets represent talc particles

orientation; compare Table 2) also hardly depends on the fiber aspect ratio. Moreover, in Figure 5b, a schematic illustration of the individual fiber arrangements in a given measurement volume is provided along with the average orientation tensor and the graphical representation of the orientation ellipses (for further details see [38, 39]).

Table 2. Herman's orientation factors of the different material constituents

Composite types		PP	Soft particle	Soft and hard particle		Short glass fiber	
Material designation and Herman's factors			PP-R32	PP-R27-T10	PP-R12-T32	PP-sgf32-1	PP-sgf32-2
WAXS (crystals)	f_a	0.014	0,007	0.001	–0.019		
	f_b	–0.295	–0.188	–0.158	–0.156		
	f_c	0.309	0.181	0.157	0.175		
SEM (talc)	f			0.91	0.8		
μ-CT	f					0.79	0.82

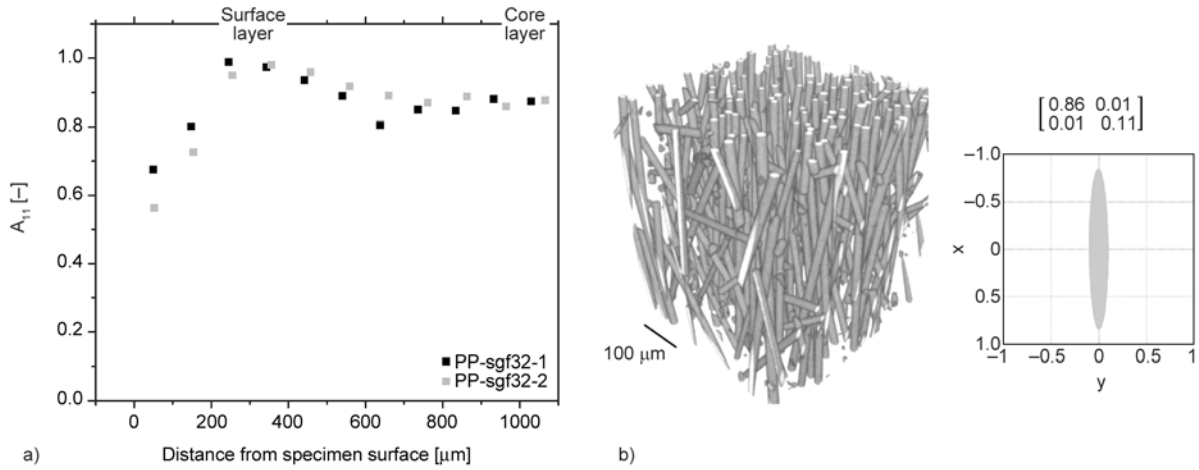

Figure 5. First entry of the orientation tensor (A_{11}) of the sgf reinforced PP as a function of the distance from the specimen surface (covering half of the specimen thickness) comparing PP-sgf32-1 and PP-sgf32-2 (a) and a schematic illustration of all fibers in a segment of the measurement volume and the orientation tensor and ellipses of PP-sgf32-1 (b)

Overall anisotropy in the stress-strain behavior in tension and compression

The tensile and compressive stress-strain behavior of PP-R32, PP-R12-T32 and PP-sgf32-2 in and perpendicular to the main melt flow direction (MFD), which reflects the main particle orientation, is depicted in Figure 6. Strain softening behavior is observed for PP-R32 for the 0° compressive and the 90° tensile specimens and more pronounced for all PP-R12-T32 specimens. In both material cases, strain softening can possibly be attributed to debonding of the particles [40, 41]. In tension, the PP-sgf32-2 specimens break in a brittle manner without major ductile deformation. In compression, the 0° specimens fail in a shear mode without major ductile deformation, whereas the 90° specimens display a highly ductile behavior. For all materials an anisotropic behavior displaying higher values in direction of particle orientation was found, both in tension and compression. In a very general sense and as expected, the

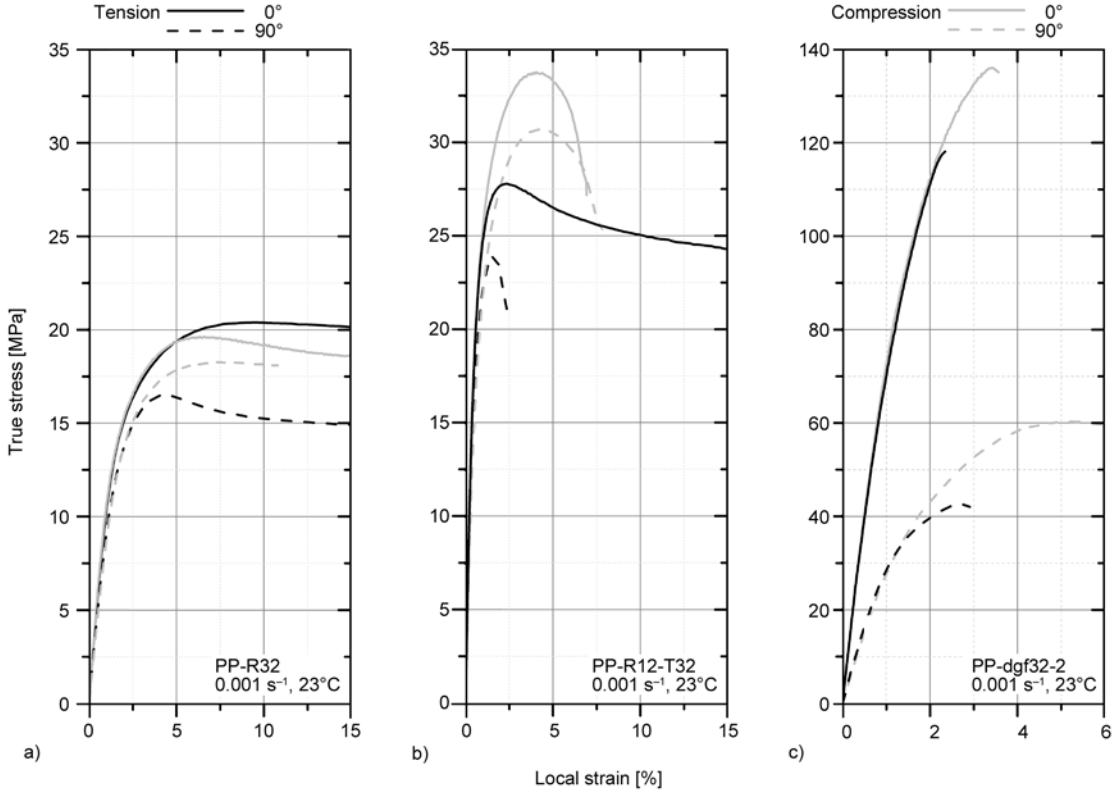

Figure 6. Stress-strain trends in compression and tension of PP-R32 (a); PP-R12-T10 (b) and PP-sgf32-2 (c)

degree of anisotropy is seen to increase with increasing filler stiffness and filler aspect ratio. When comparing the stress-strain behavior in compression and tension for the various materials and their orientation states, the following is observed. Apart from the 0° PP-32R specimens, for which the tensile and compressive behavior is rather similar, the ultimate properties (i.e. yield or failure stress) in compression are significantly higher than in tension. Furthermore, for all materials, the difference between compressive and tensile strength is apparently larger for the 90° specimens than for the 0° specimens.

3.2. Anisotropy in the deformation behavior: *E*-modulus

The anisotropy in terms of the ratio of the tensile E-modulus of the 0° specimens and the 90° specimens is depicted in Figure 7, a value of 1 corresponding to isotropic behavior. Even the neat matrix, which is typically considered to be at least quasi-isotropic, reveals higher modulus values in MFD by about 10% due to some molecular orientation. As expected, the degree of anisotropy is higher for the PP composites. For soft and hard particle systems the 0° specimens exhibit a higher modulus by approximately 25% (anisotropy ratio of 1.25). Interestingly, among the two PP-R-T composites, the specimen with higher talc content shows a slightly lower anisotropy (22%, anisotropy ratio of 1.22), which may be attributed to the lower degree of talc particle orientation, as evidenced by the SEM investigations described above. Significantly higher values for the modulus anisotropy ratio of about 2.5 were found for the PP-sgf materials, with slightly higher values for the fibers with higher aspect ratio, as expected. For comparison Figure 7 also contains corresponding data for the anisotropy ratio of a perfectly oriented, continuous fiber reinforced PP with a fiber content of 58 m% (designated as PP-cgf58) from the literature [42]. Due to the perfect alignment, the higher fiber content and the continuous fibers (corresponding to a quasi-infinite aspect ratio), a value of 7.5 was deduced for the anisotropy ratio.

To analyze the effects of the two parameters degree of fiber orientation and fiber length more quantitatively, the experimental tensile modulus values of the PP-sgf materials are plotted in Figure 8 (top) as a function of the length of the vector of the orientation ellipses in testing direction p^0 (designated as and corresponding to an averaged fiber orientation probability in testing direction). The latter parameter was used in earlier studies, in which a linear correlation was found for the modulus (and strength) as a function of p^0, thus allowing for the extrapolation of properties to a perfect fiber orientation in the testing direction ($p^0 = 1$) and perpendicular to the testing direction ($p^0 = 0$). The anisotropy ratio of these extrapolated modulus values in Figure 8 (top) correspond to the ideal, maximum modulus anisotropy ratio. In a next step these ratios were plotted in Figure 8 (bottom) as a function of the weight average fiber length and compared to theoretical modulus calculations according to the model proposed by Cox-Krenchel assuming a fiber content of 32 w% (for details on this model see [43]). Two observations may be made. First, there is rather good agreement between our experimental based values and the Cox-Krenchel prediction. Second, looking at the Cox-Krenchel prediction, a value of about 6 may be reached for the modulus anisotropy ratio with increasing fiber length for fiber lengths approaching continuous fibers. This actually is rather close to the experimental value of 7.5 for PP-cgf58 depicted in Figure 7, the difference being explicable due to the higher fiber content in the latter case.

It should be mentioned, that in terms of the modulus anisotropy ratio very similar results to those described for tensile loading conditions were found for compressive loading. This is not surprising, as it is known that in the small strain regime, in which modulus determination takes place (i.e. 0.05–0.25%), tensile and compressive moduli are essentially equal.

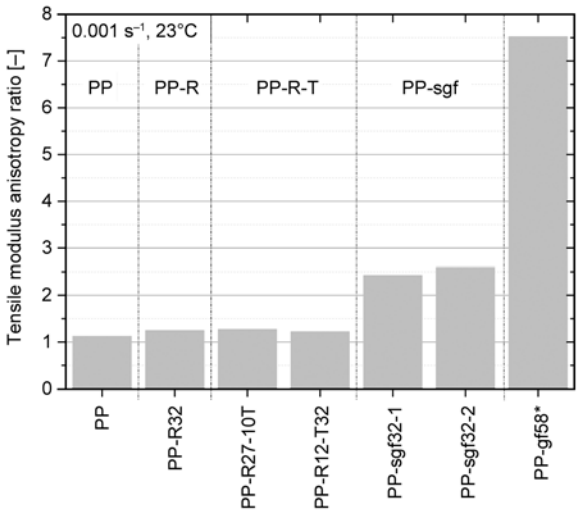

Figure 7. Anisotropy ratios (i.e. ratio of the 0° and 90° modulus) of tensile modulus values for the different PP based materials (data * from [42])

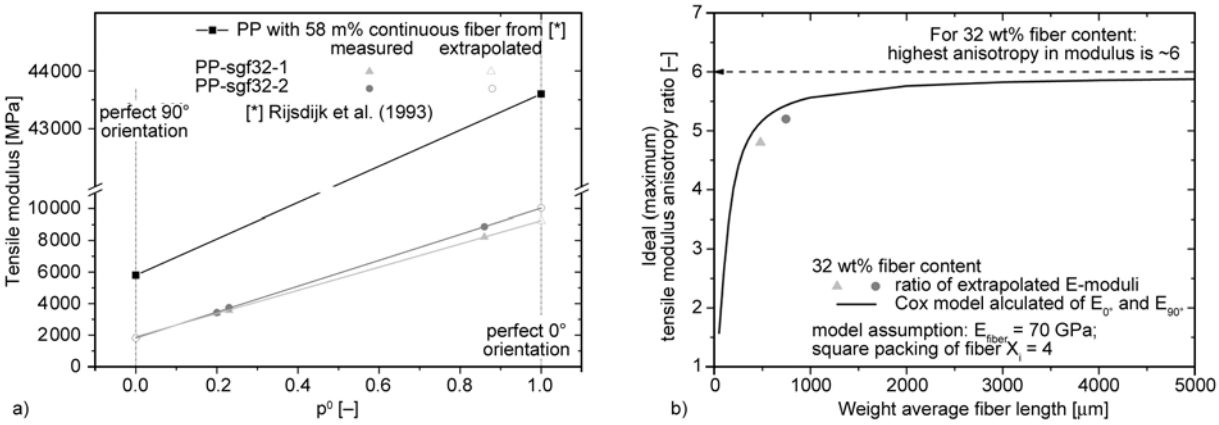

Figure 8. Fiber orientation and fiber length dependent *E*-modulus (a) and fiber length dependence of anisotropy in PP with 32 m% glass fibers (b)

3.3. Anisotropy in the deformation behavior: Poisson's ratio

In isotropic materials, the volumetric deformation (volume strain, ε_v) is directly related to the true longitudinal strain ($\varepsilon_{t,x}$) and a single Poisson's ratio value υ_{xy}. In contrast, in anisotropic materials an effective Poisson's ratio υ_{eff} characterizing volume strain effects can be defined which must account for two directional Poisson's ratios (υ_{xy} and υ_{xz}, see Equations (2)–(4) [44]:

$$\varepsilon_v = \upsilon_{eff} \cdot \varepsilon_{t,x} \tag{2}$$

$$\upsilon_{eff} = 1 - \upsilon_{xy} - \upsilon_{xz} \tag{3}$$

$$\upsilon_{xy,xz} = \left| \frac{\varepsilon_{yz2} - \varepsilon_{yz1}}{\varepsilon_{x,2} - \varepsilon_{x.1}} \right| \tag{4}$$

Therefore, increasing values for the directional Poisson's ratio result in a decreasing effective Poisson's ratio, which in turn implies a decrease in volume strain. Values for the directional Poisson's ratio, υ_{xy} and υ_{xz}, and the effective Poisson's ratio in the linear-viscoelastic regime (i.e. 0.05-0.25 %) are shown for all materials investigated in Figure 9 and Figure 10.

Starting first with the 0° specimens in Figure 9a, the deformation behavior was found to be transversely isotropic for all cases investigated with equivalent values for υ_{xy} and υ_{xz}. The directional Poisson's ratios decrease with increasing filler content for the PP-R and PP-R-T materials resulting in increasing values of effective Poisson's ratio and hence (dilatational) volume strain (see Figure 10). This observed decrease in the Poisson's ratio of the PP-R material in the linear-viscoelastic region is remarkable (Figure 9a), as based on a rule-of-mixture assumption the values should increase (Poisson's ratio of ~0.4 and ~0.5 for the pure matrix and the rubbery phase, respectively). In rubber materials the bulk modulus is much larger than the *E*-modulus and shear modulus due to the high Poisson's ratio. When a specimen

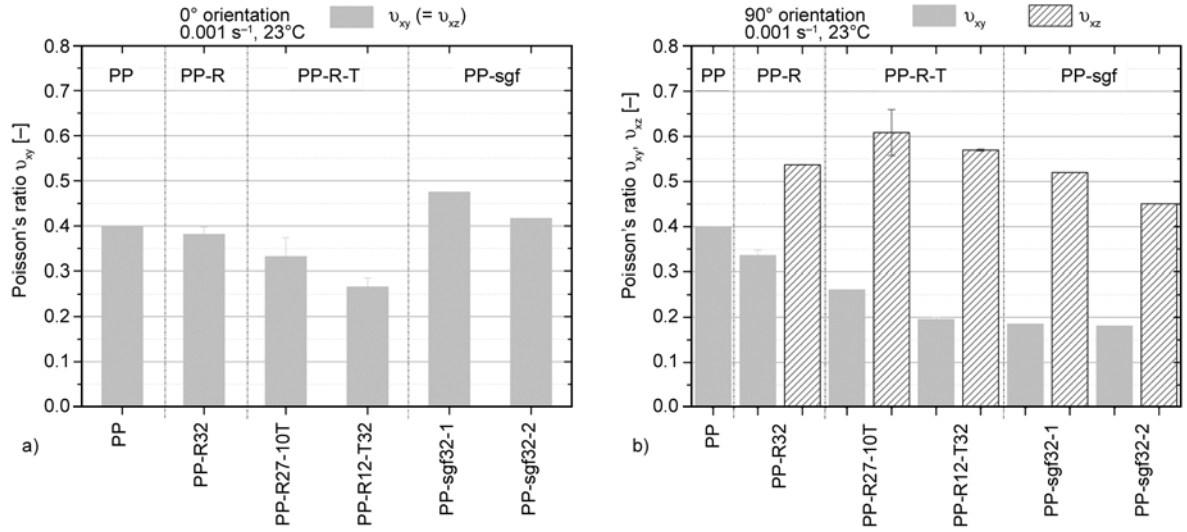

Figure 9. Tensile, directional Poisson's ratios for 0° (a) and 90° (b) specimens of the different PP based materials

is loaded in tension, the embedded elongated rubber particles and/or the matrix/rubber interphase are subjected to tri-axial stress and thus behavior is governed by the bulk modulus. The high bulk modulus of the rubbery phase may thus be the reason for the inhibited contraction in *y*-direction. By an increased addition of talc, the directional Poisson's ratio is further decreased. This can be attributed to the low Poisson's ratio of talc (~0.27 according [45]). The highest directional Poisson's ratio values were measured for the PP-sgf materials. This in turn corresponds to the lowest effective Poisson's ratio and volume strain values (see Figure 10), which may be caused by the high constraint of the matrix phase imposed by the fibers.

Regarding the 90° specimens (see Figure 9b), the two directional Poisson's ratio values υ_{xy} and υ_{xz} differ significantly. For this case, the contraction in the direction of particle orientation (*y*-direction) is increasingly inhibited with increasing particle stiffness and particle aspect ratio. Therefore, the directional Poisson's ratio υ_{xy} is lowest for PP-sgf32-2. The inhibited deformation in *y*-direction is compensated by an increased deformation in *z*-direction (specimen thickness), with values for the Poisson's ratio υ_{xz} ranging from about 0.45 to 0.6 for all materials. When combining these two directional Poisson's ratio values to the effective Poisson's ratio (see Figure 10), increasing values are observed for specimens containing fillers with increasing particle stiffness and particle aspect ratio. Interestingly, for the soft and hard particle filled PP, the effective Poisson's ratio and hence the (dilatational) volume strain is larger for the 0° than for the 90° specimens, while the opposite trend is observed for PP-sgf materials.

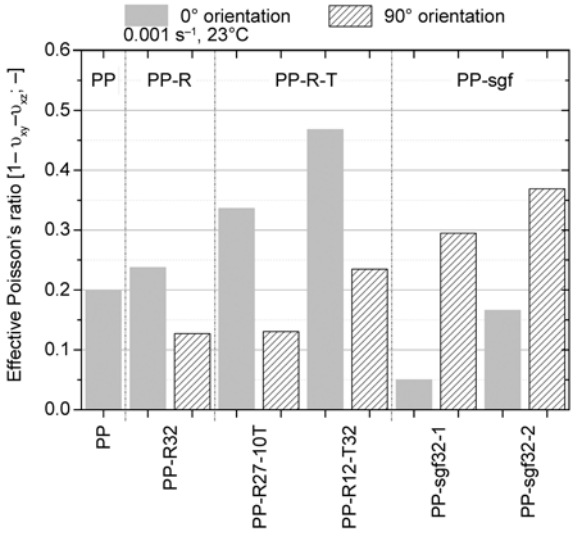

Figure 10. Effective tensile Poisson's ratio for 0° and 90° specimens of the different PP based materials

In Figure 11, the two Poisson's ratio values υ_{xy} and υ_{xz} are plotted as a function of the longitudinal strain

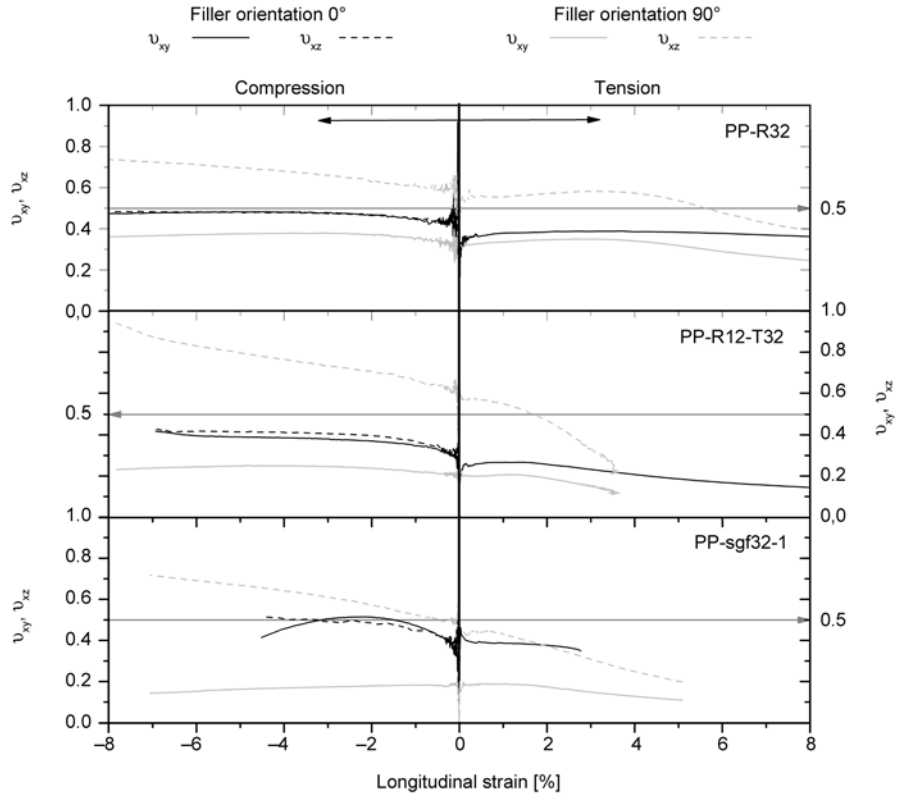

Figure 11. Tensile and compressive Poisson's ratio as a function of longitudinal strain for PP-R32, PP-R12-R32 and PP-sgf32-1

for the tensile and compressive loading, and for the 0° and 90°specimen, respectively. As expected, the two Poisson's ratio trends of the 0° specimens are equivalent, due to the transverse isotropy. For the 90° specimens, however, $v_{xz}(\varepsilon_x)$ is significantly larger than $v_{xy}(\varepsilon_x)$ as the transverse strain in *y*-direction is hindered by the filler orientation in this direction. Similar to observations for *E*-moduli (see above), in the linear visco-elastic regime, the Poisson's ratio in tension and compression are essentially equivalent (within measurement inaccuracy). At higher values of tensile deformation, the Poisson's ratio values decrease with increasing longitudinal strain. This trend is more pronounced for $v_{xz}(\varepsilon_x)$ and 90° specimens. As discussed above, this in turn corresponds to an increase in volume strain values which can be correlated to the onset of void formation [44]. In contrast, in compression the Poisson's ratio values increase and the volume strain decreases with increasing longitudinal strain, corresponding to shear governed local deformation. In terms of absolute values, it should be noted, that $v_{xz}(\varepsilon_x)$ in tension displays values above 0.5 for some 90° specimens, with even higher values obtained in compression.

3.4. Anisotropy and compression/tension asymmetry in the failure behavior

In terms of the anisotropy of ultimate properties (i.e. tensile and compressive strength), similar trends, as discussed above for the small strain regime (i.e. *E*-modulus), can be observed (see Figure 12). Interestingly, when comparing tension and compression, the anisotropy ratio is always lower in compression with larger differences for short and continuous glass fiber reinforced materials. This phenomenon can be related to differences in the damage evolution, especially associated with the significant formation of voids in tension vs. shear yielding governed deformation in compression of the 90° specimens. Similar differences in the microscopic deformation modes under tension and compression also occur in the other PP based materials (compare also Poisson's ratio trends discussed above).

Turning to the compression/tension asymmetry, values for the compressive/tensile strength ratio are plotted for the various materials in Figure 13. Clearly, the asymmetry of the 90° specimens is always notably higher than of the corresponding 0° specimens. For neat PP, the difference in the compressive/tensile strength ratio of the 0° and 90° specimen is a consequence of the isotropic behavior in compression testing (equivalent yield stress values of 0° and 90° specimens). Apparently, differences in the molecular and crystalline orientation of 0° and 90° specimens play only a minor role in governing the compressive behavior of PP. Compared to the neat matrix, the soft and hard particle filled PP composites exhibit lower values of compression/tension asymmetry. As discussed above for the Poisson's ratio effects, this may again possibly be a consequence of the incompressibility and the corresponding high bulk modulus of the rubber filler. Following this argument, the decreasing rubber content may be the cause for the

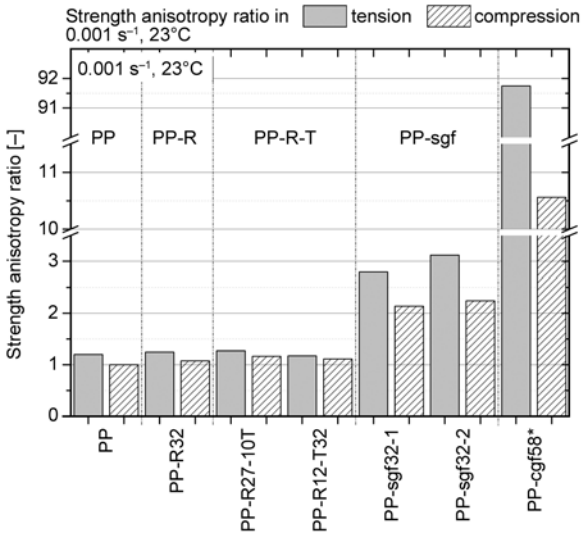

Figure 12. Anisotropy ratios (i.e. ratio of the 0° and 90° strength) of tensile and compressive strength values for the different PP based materials (data * from [42])

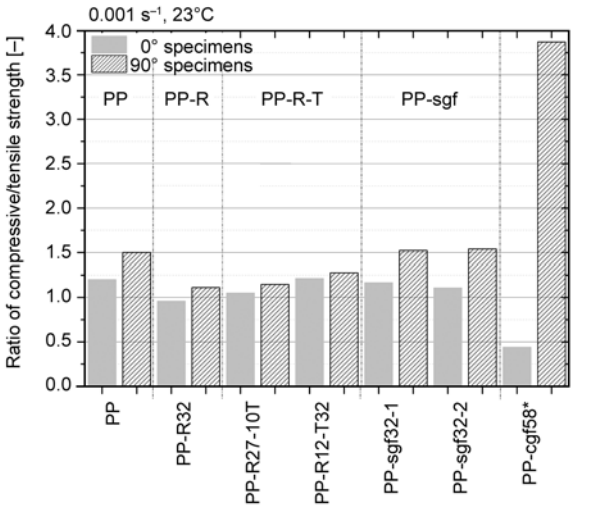

Figure 13. Asymmetry as represented by the ratio of the compressive to the tensile strength for the 0° and 90° specimens of the different composites (data * from [42])

observed increasing compression/tension asymmetry of the PP-R-T materials.

Finally, for glass fiber reinforced materials, the compression/tension asymmetry of the 0° specimen decreases and of the 90° specimen increases with increasing fiber length. With respect to the 0° specimens, longer fibers are more prone to buckling at equivalent matrix stiffness values which results in lower compressive strength values. Regarding the 90° specimens, and as already stated above, the significantly higher compression/tension asymmetry may be attributed to changes in deformation mechanisms from tensile to compressive testing. In the tensile loading mode, major void formation is likely for particles/fiber with perpendicular orientation and especially with increasing aspect ratio. In sharp contrast, shear deformation and shear failure dominates the compressive loading mode.

4. Conclusions

An overall objective of the present paper was to comprehensively analyze the deformation modes of various PP based materials (including neat PP, rubber toughened PP-R, rubber and talc filled PP-R-T, and short glass fiber reinforced PP-sgf) as affected by the orientation and the loading mode (tension vs. compression). Using a specially designed multi-tool for injection molding of specimens with high soft and/or hard particle or fiber orientation, a special focus was on investigating mechanical anisotropy effects and compression/tension asymmetry effects in the small strain (visco-elastic) and ultimate failure regime. The following results were obtained:

- Via the novel UD tool for producing injection molded specimens, a high degree of orientation could be achieved in all of the materials investigated.
- Testing of 0° and 90° specimens revealed significant but various degrees of anisotropic behavior for all materials in terms of *E*-modulus, Poisson's ratio (incl. Poisson's ratio evolution) and strength.
- Anisotropic behavior was found to be more pronounced in tension than in compression.
- The compression/tension asymmetry strongly depends on the filler type and orientation, exhibiting higher values for 90° specimens.
- An analysis of the evolution of Poisson's ratio values with increasing longitudinal strain allows for conclusions on the volumetric deformation behavior. The higher compression/tension asymmetry of the 90° specimens is considered to be a result of the larger scale voiding in tension, a phenomenon which is essentially suppressed in compression.

Of paramount practical importance, these results may serve as basis for the development of more accurate material models which not only account for the anisotropic behavior, but also for the orientation dependent compression/tension asymmetry.

Acknowledgements

This research was undertaken within the bilateral project 1.02 'Heterogeneous Polymer Compounds – PP Compounds and Magneto-Elastomers' of the COMET K-Project 'Advanced Polymeric Materials and Process Technologies (APMT)' (http://apmt/jku.at). The project is funded as part of the COMET program of the Austrian Research Promotion Agency (FFG) and is supported by the Federal Ministry for Transport, Innovation and Technology (BMVIT), Federal Ministry of Economy, Family and Youth (BMWFJ) and the Upper Austrian Government (Research Department). The authors thank Borealis AG (Linz, Austria) for fruitful discussions, providing the specimens as well as conducting the WAXS and SEM analysis, and the University of Applied Sciences Upper Austria, Wels Campus (Wels, Austria) for conducting the μ-CT experiments. Also the support of Paul Freudenthaler (JKU, Linz, Austria) in conducting the mechanical tests is gratefully acknowledged.

References

[1] Kissel W. J., Han H., Meyer J. A.: Polypropylene: Structure, properties, manufacturing processes and applications. in 'Handbook of polypropylene and polypropylene composites' (ed.: Harutun K. G.) Marcel Dekker, Hoboken, 10–27 (2003).

[2] Liang J. Z., Li R. K.: Rubber toughening in polypropylene: A review. Journal of Applied Polymer Science, **77**, 409–417 (2000). DOI: 10.1002/(SICI)1097-4628(20000711)77:2<409::AID-APP18>3.0.CO;2-N

[3] Denac M., Musil V., Šmit I.: Polypropylene/talc/SEBS (SEBS-g-MA) composites. Part 2. Mechanical properties. Composites Part A: Applied Science and Manufacturing, **36**, 1282–1290 (2005). DOI: 10.1016/j.compositesa.2005.01.011

[4] Fu S-Y., Lauke B.: Fracture resistance of unfilled and calcite-particle-filled ABS composites reinforced by short glass fibers (SGF) under impact load. Composites Part A: Applied Science and Manufacturing, **29**, 631–641 (1998). DOI: 10.1016/S1359-835X(97)00111-5

[5] Fu S-Y., Xu G., Mai Y-W.: On the elastic modulus of hybrid particle/short-fiber/polymer composites. Composites Part B: Engineering, **33**, 291–299 (2002). DOI: 10.1016/S1359-8368(02)00013-6

[6] Hartikainen J., Hine P., Szabó J. S., Lindner M., Harmia T., Duckett R. A., Friedrich K.: Polypropylene hybrid composites reinforced with long glass fibres and particulate filler. Composites Science and Technology, **65**, 257–267 (2005).
DOI: 10.1016/j.compscitech.2004.07.010

[7] Huang C., Li R. K., Wu C., Duan Z.: Stiffness behaviour of injection moulded short glass fibre/impact modifier/polypropylene hybrid composites. Journal of Materials Processing Technology, **96**, 48–52 (1999).
DOI: 10.1016/S0924-0136(99)00251-4

[8] Laura D., Keskkula H., Barlow J. W., Paul D. R.: Effect of rubber particle size and rubber type on the mechanical properties of glass fiber reinforced, rubber-toughened nylon 6. Polymer, **44**, 3347–3361 (2003).
DOI: 10.1016/S0032-3861(03)00221-0

[9] Tjong S. C., Xu S. A., Mai Y. W.: Impact fracture toughness of short glass fiber-reinforced polyamide 6,6 hybrid composites containing elastomer particles using essential work of fracture concept. Materials Science and Engineering: A, **347**, 338–345 (2003).
DOI: 10.1016/S0921-5093(02)00609-3

[10] Tjong S. C., Xu S-A., Li R. K-Y., Mai Y-W.: Mechanical behavior and fracture toughness evaluation of maleic anhydride compatibilized short glass fiber/SEBS/polypropylene hybrid composites. Composites Science and Technology, **62**, 831–840 (2002).
DOI: 10.1016/S0266-3538(02)00037-4

[11] Wang W., Tang L., Qu B.: Mechanical properties and morphological structures of short glass fiber reinforced PP/EPDM composite. European Polymer Journal, **39**, 2129–2134 (2003).
DOI: 10.1016/S0014-3057(03)00157-5

[12] Zhang L., Li C., Huang R.: Toughness mechanism of polypropylene/elastomer/filler composites. Journal of Polymer Science Part B: Polymer Physics, **43**, 1113–1123 (2005).
DOI: 10.1002/polb.20395

[13] Wang C., Su J. X., Li J., Yang H., Zhang Q., Du R. N., Fu Q.: Phase morphology and toughening mechanism of polyamide 6/EPDM-*g*-MA blends obtained via dynamic packing injection molding. Polymer, **47**, 3197–3206 (2006).
DOI: 10.1016/j.polymer.2006.03.012

[14] Wang Y., Zhang Q., Na B., Du R., Fu Q., Shen K.: Dependence of impact strength on the fracture propagation direction in dynamic packing injection molded PP/EPDM blends. Polymer, **44**, 4261–4271 (2003).
DOI: 10.1016/S0032-3861(03)00366-5

[15] Fellahi S., Favis B. D., Fisa B.: Morphological stability in injection-moulded high-density polyethylene/polyamide-6 blends. Polymer, **37**, 2615–2626 (1996).
DOI: 10.1016/0032-3861(96)87620-8

[16] Karger-Kocsis J., Csikai I.: Skin-core morphology and failure of injection-molded specimens of impact-modified polypropylene blends. Polymer Engineering and Science, **27**, 241–253 (1987).
DOI: 10.1002/pen.760270403

[17] Bay R. S., Tucker C. L.: Fiber orientation in simple injection moldings. Part I: Theory and numerical methods. Polymer Composites, **13**, 317–331 (1992).
DOI: 10.1002/pc.750130409

[18] Gupta M., Wang K. K.: Fiber orientation and mechanical properties of short-fiber-reinforced injection-molded composites: Simulated and experimental results. Polymer Composites, **14**, 367–382 (1993).
DOI: 10.1002/pc.750140503

[19] Cintra J. S., Tucker C. L.: Orthotropic closure approximations for flow-induced fiber orientation. Journal of Rheology, **39**, 1095–1122 (1995).
DOI: 10.1122/1.550630

[20] Greene J. P., Wilkes J. O.: Numerical analysis of injection molding of glass fiber reinforced thermoplastics. Part 2: Fiber orientation. Polymer Engineering and Science, **37**, 1019–1035 (1997).
DOI: 10.1002/pen.11747

[21] Choi W. J., Kim S. C.: Effects of talc orientation and non-isothermal crystallization rate on crystal orientation of polypropylene in injection-molded polypropylene/ethylene–propylene rubber/talc blends. Polymer, **45**, 2393–2401 (2004).
DOI: 10.1016/j.polymer.2004.01.058

[22] Papathanasiou T. D.: Flow-induced alignement in injection molding of fiber-reinforced polymer composites. in 'Flow-induced alignment in composite materials' (eds.: Guell D. C., Papathanasiou T. D.) Woodhead, Cambridge, 112–165 (1997).

[23] Obata Y., Sumitomo T., Ijitsu T., Matsuda M., Nomura T.: The effect of talc on the crystal orientation in polypropylene/ethylene-propylene rubber/talc polymer blends in injection molding. Polymer Engineering and Science, **41**, 408–416 (2001).
DOI: 10.1002/pen.10738

[24] Zhang M., Xu J., Zhang Z., Zeng H., Xiong X.: Effect of transcrystallinity on tensile behaviour of discontinuous carbon fibre reinforced semicrystalline thermoplastic composites. Polymer, **37**, 5151–5158 (1996).
DOI: 10.1016/0032-3861(96)00341-2

[25] Pukánszky B., Belina K., Rockenbauer A., Maurer F. H. J.: Effect of nucleation, filler anisotropy and orientation on the properties of PP composites. Composites, **25**, 205–214 (1994).
DOI: 10.1016/0010-4361(94)90018-3

[26] Norman D. A., Robertson R. E.: The effect of fiber orientation on the toughening of short fiber-reinforced polymers. Journal of Applied Polymer Science, **90**, 2740–2751 (2003).
DOI: 10.1002/app.12913

[27] Bernasconi A., Davoli P., Basile A., Filippi A.: Effect of fibre orientation on the fatigue behaviour of a short glass fibre reinforced polyamide-6. International Journal of Fatigue, **29**, 199–208 (2007).
DOI: 10.1016/j.ijfatigue.2006.04.001

[28] Fu S-F., Lauke B.: Effects of fiber length and fiber orientation distributions on the tensile strength of short-fiber-reinforced polymers. Composites Science and Technology, **56**, 1179–1190 (1996).
DOI: 10.1016/S0266-3538(96)00072-3

[29] Díez-Gutiérrez S., Rodríguez-Pérez A., De Saja J. A., Velasco J. I.: Heterogeneity and anisotropy of injection-molded discs of polypropylene and polypropylene composites. Journal of Applied Polymer Science, **77**, 1275–1283 (2000).
DOI: 10.1002/1097-4628(20000808)77:6<1275::AID-APP12>3.0.CO;2-P

[30] Kunkel F., Becker F., Kolling S.: Mechanical characterization of talc particle filled thermoplastics. in '8. Europäische LS-DYNA Anwenderkonferenz. Strassburg, Frankreich', p14 (2011).

[31] Hartl A. M., Balasooriya W., Reiter M., Lang R. W., Schossig M., Jerabek M.: Comparison of methods to characterize damage onset in short glass fiber filled polypropylene. in 'Proceedings of the ICCM19, Montreal, Canada' 2546–2551 (2013).

[32] Gedde U. W.: Polymer physics. Chapman and Hall, London (1995).

[33] Hermans P. H., Hermans J. J., Vermaas D., Weidinger A.: Deformation mechanism of cellulose gels. IV. General relationship between orientation of the crystalline and that of the amorphous portion. Journal of Polymer Science, **3**, 1–9 (1948).
DOI: 10.1002/pol.1948.120030101

[34] Sedighiamiri A., Senden D. J. A., Tranchida D., Govaert L. E., van Dommelen J. A. W.: A micromechanical study on the deformation kinetics of oriented semi-crystalline polymers. Computational Materials Science, **82**, 415–426 (2014)
DOI: 10.1016/j.commatsci.2013.09.068

[35] Salaberger D., Kannappan K. A., Kastner J., Reussner J., Auinger T.: Evaluation of computed tomography data from fibre reinforced polymers to determine fibre length distribution. International Polymer Processing, **26**, 283–291 (2011).
DOI: 10.3139/217.2441

[36] Jerabek M., Major Z., Lang R. W.: Strain determination of polymeric materials using digital image correlation. Polymer Testing, **29**, 407–416 (2010).
DOI: 10.1016/j.polymertesting.2010.01.005

[37] Hornsby P. R.: Rheology, compounding and processing of filled thermoplastics. in 'Mineral fillers in thermoplastics I' (eds.: Jancar J., Fekete E., Hornsby P. R., Jancar J., Pukánszky B., Rothon R. N.) Springer, Berlin, Vol 139, 155–217 (1999).
DOI: 10.1007/3-540-69220-7_4

[38] Advani S. G., Tucker C. L.: The use of tensors to describe and predict fiber orientation in short fiber composites. Journal of Rheology, **31**, 751–784 (1987).
DOI: 10.1122/1.549945

[39] Advani S. G., Tucker C. L.: A tensor description of fiber orientation in short fiber composites. in 'Proceedings of the ANTEC' 85 Annual Technical Conference, Washington, USA, 1113-1118 (1985).

[40] Delhaye V., Clausen A. H., Moussy F., Othman R., Hopperstad O. S.: Influence of stress state and strain rate on the behaviour of a rubber-particle reinforced polypropylene. International Journal of Impact Engineering, **38**, 208–218 (2011).
DOI: 10.1016/j.ijimpeng.2010.11.004

[41] Hempel P., Seelig T.: Talcum particle modified thermoplastics, Part II: Computational modeling. in '13. Problemseminar: Deformation und Bruchverhalten von Kunststoffen, Merseburg Germany' p8 (2011).

[42] Rijsdijk H., Contant M., Peijs A.: Continuous-glass-fibre-reinforced polypropylene composites: I. Influence of maleic-anhydride-modified polypropylene on mechanical properties. Composites Science and Technology, **48**, 161–172 (1993).
DOI: 10.1016/0266-3538(93)90132-Z

[43] Thomason J. L., Vlug M. A.: Influence of fibre length and concentration on the properties of glass fibre-reinforced polypropylene: 1. Tensile and flexural modulus. Composites Part A: Applied Science and Manufacturing, **27**, 477–484 (1996).
DOI: 10.1016/1359-835X(95)00065-A

[44] Jerabek M., Major Z., Renner K., Móczó J., Pukánszky B., Lang R. W.: Filler/matrix-debonding and micromechanisms of deformation in particulate filled polypropylene composites under tension. Polymer, **51**, 2040–2048 (2010).
DOI: 10.1016/j.polymer.2010.02.033

[45] Bailey E., Holloway J. R.: Experimental determination of elastic properties of talc to 800°C, 0.5 GPa; Calculations of the effect on hydrated peridotite, and implications for cold subduction zones. Earth and Planetary Science Letters, **183**, 487–498 (2000).
DOI: 10.1016/S0012-821X(00)00288-0